Article

Immunity

The tissue-resident regulatory T cell pool is shaped by transient multi-tissue migration and a conserved residency program

Graphical abstract

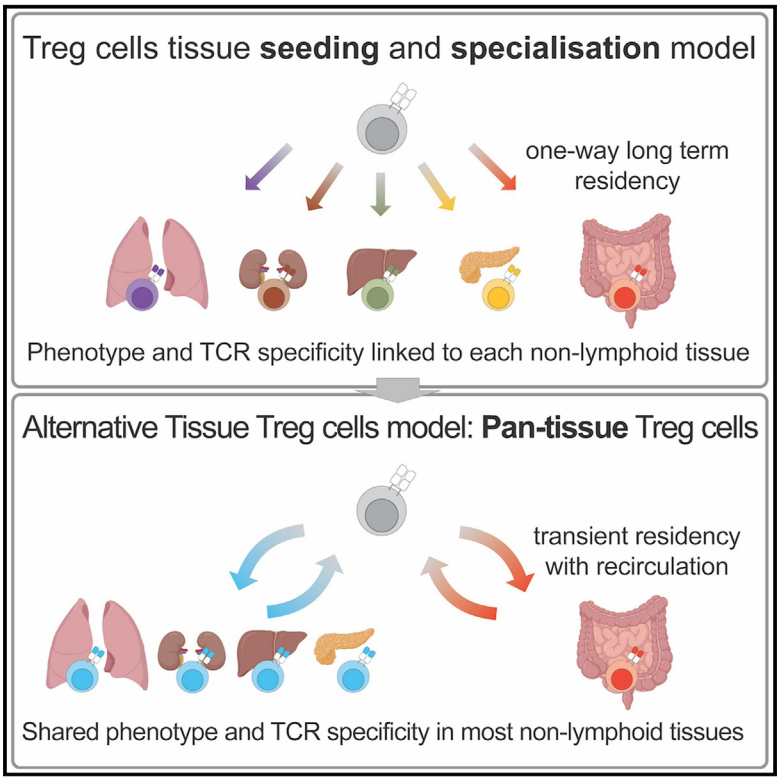

Highlights

- Regulatory T cells across different non-lymphoid tissues share a common phenotype
- Tissue-resident regulatory T cells dwell in the tissues for 3–10 weeks before exit
- Shared T cell receptor sequences confer multi-tissue migration
- Tissue-resident regulatory T cells are tissue agnostic in rehoming assays

Authors

Oliver T. Burton, Orian Bricard, Samar Tareen, ..., Brian D. Brown, James Dooley, Adrian Liston

Correspondence

al989@cam.ac.uk

In brief

Regulatory T (Treg) cells found in peripheral tissues were considered tissue restricted. Here, Burton et al. demonstrate that tissue Treg cells share a common phenotype and T cell receptor (TCR) repertoire, which confers multi-tissue migration. Thus, tissue Treg cells only maintain transient tissue residency and are tissue agnostic in rehoming assays.

Burton et al., 2024, Immunity *57*, 1–17
July 9, 2024 © 2024 The Author(s). Published by Elsevier Inc.
https://doi.org/10.1016/j.immuni.2024.05.023

CellPress

Please cite this article in press as: Burton et al., The tissue-resident regulatory T cell pool is shaped by transient multi-tissue migration and a conserved residency program, Immunity (2024), https://doi.org/10.1016/j.immuni.2024.05.023

Immunity

CellPress
OPEN ACCESS

Article

The tissue-resident regulatory T cell pool is shaped by transient multi-tissue migration and a conserved residency program

Oliver T. Burton,[1,2,3,4,9] Orian Bricard,[4,9] Samar Tareen,[4] Vaclav Gergelits,[1,4] Simon Andrews,[4] Laura Biggins,[4] Carlos P. Roca,[4] Carly Whyte,[4] Steffie Junius,[2,3] Aleksandra Brajic,[2,3] Emanuela Pasciuto,[2,3,5] Magda Ali,[1] Pierre Lemaitre,[2,3] Susan M. Schlenner,[3] Harumichi Ishigame,[6,7] Brian D. Brown,[8] James Dooley,[1,2,3,4,10] and Adrian Liston[1,2,3,4,10,11,*]

[1]Department of Pathology, University of Cambridge, Cambridge, UK
[2]VIB Center for Brain and Disease Research, Leuven, Belgium
[3]KU Leuven, University of Leuven, Department of Microbiology and Immunology, Leuven, Belgium
[4]Babraham Institute, Babraham Research Campus, Cambridge, UK
[5]University of Antwerp, Center of Molecular Neurology, Antwerp, Belgium
[6]Laboratory for Tissue Dynamics, RIKEN Center for Integrative Medical Sciences, Yokohama, Kanagawa 230-0045, Japan
[7]Near-InfraRed Photo-Immunotherapy Research Institute, Kansai Medical University, Hirakata, Osaka 573-1010, Japan
[8]Icahn Genomics Institute, Icahn School of Medicine at Mount Sinai, New York, NY, USA
[9]These authors contributed equally
[10]Senior author
[11]Lead contact
*Correspondence: al989@cam.ac.uk
https://doi.org/10.1016/j.immuni.2024.05.023

SUMMARY

The tissues are the site of many important immunological reactions, yet how the immune system is controlled at these sites remains opaque. Recent studies have identified Foxp3$^+$ regulatory T (Treg) cells in non-lymphoid tissues with unique characteristics compared with lymphoid Treg cells. However, tissue Treg cells have not been considered holistically across tissues. Here, we performed a systematic analysis of the Treg cell population residing in non-lymphoid organs throughout the body, revealing shared phenotypes, transient residency, and common molecular dependencies. Tissue Treg cells from different non-lymphoid organs shared T cell receptor (TCR) sequences, with functional capacity to drive multi-tissue Treg cell entry and were tissue-agnostic on tissue homing. Together, these results demonstrate that the tissue-resident Treg cell pool in most non-lymphoid organs, other than the gut, is largely constituted by broadly self-reactive Treg cells, characterized by transient multi-tissue migration. This work suggests common regulatory mechanisms may allow pan-tissue Treg cells to safeguard homeostasis across the body.

INTRODUCTION

The tissues are the key site for pathological reactions across a range of immunological challenges. Our understanding of the immune component of (non-lymphoid) tissues is, however, relatively limited and often extrapolated from the lymphoid tissues. An early paradigm for tissue immunology emerged from the biology of tissue macrophages, where generic precursor cells seed tissues at early developmental stages and undergo extensive specialization during indefinite residency.[1] Fetal $\gamma\delta$ T cells provide a lymphocyte counterpart to the tissue residency of myeloid cells[2]; however, $\alpha\beta$ T cells were largely exempt from the seeding and specialization model, being defined by their circular migration through the lymphatic system.

Tissue-resident memory (Trm) CD8$^+$ T cells and, more recently, CD4$^+$ T cells have broken the circular migration paradigm for $\alpha\beta$ T cells. Trm cells are antigen-experienced memory T cells with prolonged or even indefinite residency within the tissue of original antigen experience.[3] In infectious models, long-lasting pathogen-reactive clonal populations of T cells are found in the tissue following resolution and contribute to protection during re-infection.[4–11] In the human context, Trm cells accumulate at barrier sites,[12] and undergo site-specific clonal expansion.[13] In liver transplantation and recovery experiments, Trm cells from the original transplant can even be recovered in the transplanted organ 10 years later.[14] Murine Trm cells express distinct phenotypic markers, including CD69, CD103, C-X-C motif chemokine receptor 6 (CXCR6), CD11a, and programmed cell death protein 1 (PD-1),[15] driven by the transcription factors Hobit, Blimp1, and Runx3.[16–19]

Tissue regulatory T (Treg) cells, isolated from multiple non-lymphoid tissues, are an attractive analog to the conventional

This is an open access article under the CC BY license (http://creativecommons.org/licenses/by/4.0/).

Please cite this article in press as: Burton et al., The tissue-resident regulatory T cell pool is shaped by transient multi-tissue migration and a conserved residency program, Immunity (2024), https://doi.org/10.1016/j.immuni.2024.05.023

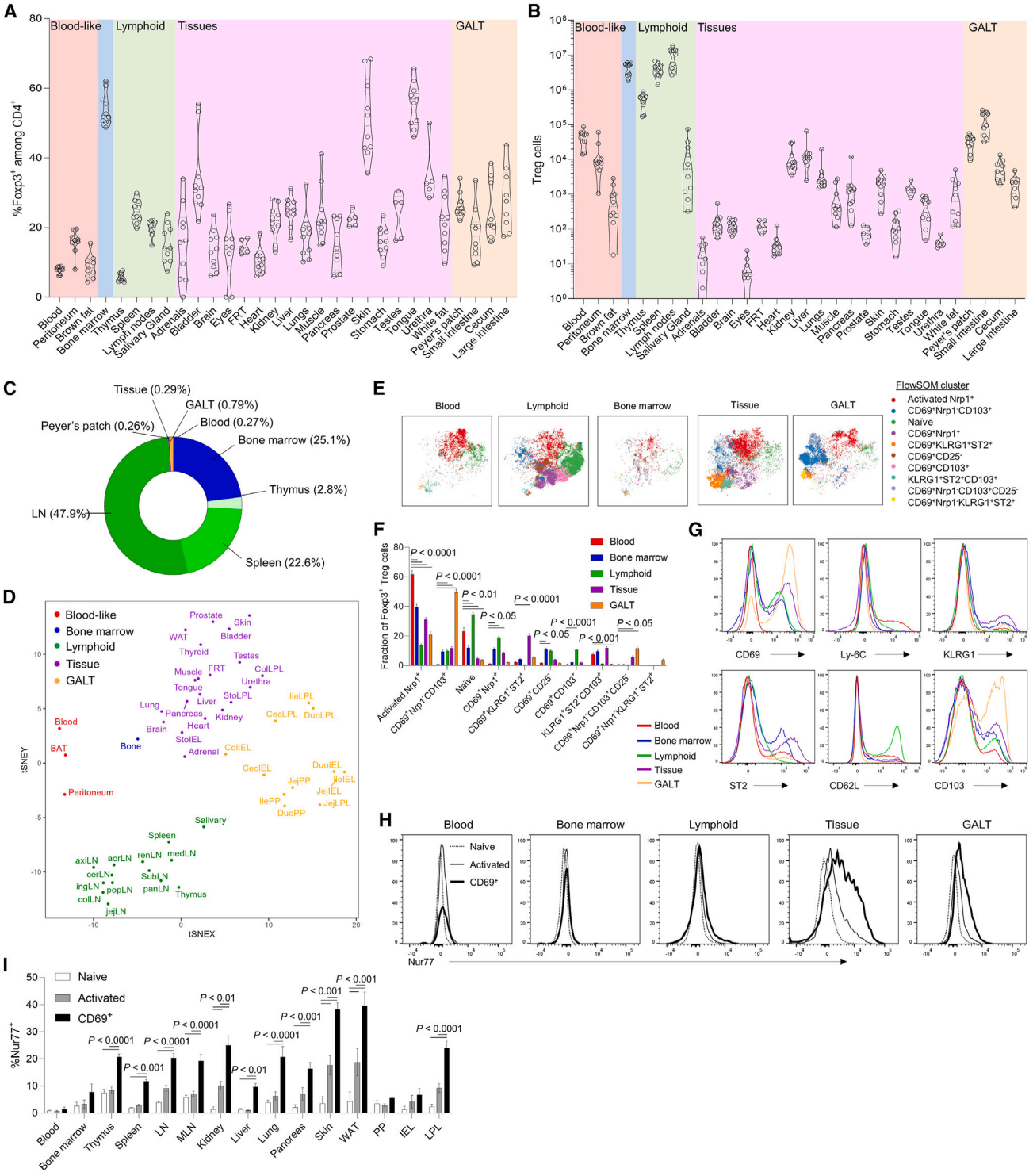

Figure 1. A common phenotypic program unites tissue-resident Treg cells across all major organs

Foxp3$^{Thy1.1}$ mice, aged 12–20 weeks, were injected with intravenous anti-CD45 antibody label. Tissues were dissected for flow cytometric analysis of Treg cells, gating out cells positive for intravenous anti-CD45 antibody.

(A and B) (A) Frequency of Treg cells among CD4$^+$TCRβ$^+$ T cells (n = 9–10), with (B) absolute numbers.

(C) Cumulative absolute number within major tissues sources.

(D) Treg cell phenotype from 48 organs was assessed by t-distributed stochastic neighbor embedding (tSNE) based on marker expression, with the median value (from n = 9–10 replicates) organically clustered into five tissue groups. Data in F and I are presented as mean ± SE with p values derived from two-way ANOVA with Dunnett's multiple comparisons.

(legend continued on next page)

Please cite this article in press as: Burton et al., The tissue-resident regulatory T cell pool is shaped by transient multi-tissue migration and a conserved residency program, Immunity (2024), https://doi.org/10.1016/j.immuni.2024.05.023

CellPress
OPEN ACCESS

Trm cell populations. Tissue Treg cell express at high rates the canonical Trm markers of CD69, CD103, CD11a, and PD-1, in addition to markers more commonly associated with circulating memory CD8$^+$ T cells, such as killer cell lectin-like receptor G1 (KLRG1).[20] These local Treg cells contribute to immunological tolerance in the tissues; more intriguingly, they have additional roles in physiological homeostasis. Adipose Treg cells aid insulin sensitivity[21] and lipolysis,[22] muscle Treg cells can aid injury repair,[23] brain Treg cells drive oligodendrocyte differentiation,[24] skin Treg cells prevent fibrosis,[25,26] uterine Treg cells support fetal growth,[27] and diverse physiological responses have been described across other tissues.[20] The parallels between Trm cells and tissue Treg cells have supported the conceptualization of tissue Treg cells under the seeding and specialization model of leukocyte tissue residency, although the generation of direct data for tissue Treg cells has lagged behind.

Here, we tested the seeding and specialization model of tissue Treg cells through a systematic analysis of the Treg cell population throughout the body. Using high-parameter flow cytometry, we found unified phenotypes for tissue Treg cells in the non-lymphoid non-gut tissues, coupled with common molecular dependencies and shared T cell receptor (TCR) clonality. Our data further showed that tissue residency was generally short, on the order of ~3 weeks, and extracted tissue Treg cells were tissue-agnostic on re-entry. Together, these results suggest that tissue Treg cells operate under a different residency paradigm from Trm cells or tissue-resident macrophages, being characterized by slow percolation through multiple tissues in a pan-tissue adapted state.

RESULTS

Tissue Treg cells share common phenotypes across the non-lymphoid tissues

To assess the uniqueness of Treg cells residing within organs, we profiled the infiltrating population in 48 murine tissues, covering a comprehensive set of lymphoid, non-lymphoid, and gut-associated tissues (Figure S1A). Looking at the 28 major tissue sources, Treg cells were largely represented as 10%–20% of CD4$^+$ T cells across each tissue, with frequencies elevated to ~50% in the bone marrow, skin, and tongue (Figure 1A). In absolute numbers, ~10^4–10^7 Treg cells were found in each lymphoid tissue type, ~10^3–10^5 Treg cells found in each gut-associated tissue type, and ~10–10^4 Treg cells found in each non-lymphoid tissue type (Figure 1B). Cumulatively, lymphoid tissues contained >98% of Treg cells identified across the body, with another 0.3% of Treg cells found in the blood, 0.8% of Treg cells in the gut-associated tissues, and 0.3% of Treg cells in the combined set of all non-lymphoid non-gut tissues (Figure 1C).

We next compared the phenotype of Treg cells across each of 48 source tissues using a high-dimensional flow cytometry panel allowing gating of Treg cells and assessment of markers associated with Treg cell activation and residency (Figures S1A and S1B). Organic clustering of Treg cell phenotypes across the source tissues identified five tissue type clusters, corresponding to blood-like Treg cells, bone marrow, lymphoid tissue Treg cells, non-lymphoid tissues, and gut-associated tissues (Figure 1D). These organic clusters largely correspond to anatomical tissue types, with a few notable exceptions, such as stomach Treg cells lying phenotypically closer to tissue Treg cells than to their intestinal counterparts. Grouping individual tissues into these larger tissue types provided resolution of Treg cell phenotypes into clusters (Figure 1E), with non-lymphoid tissues populated by activated and CD69$^+$ Treg cells, including enriched ST2$^+$ and KLRG1$^+$ populations (Figure 1F). None of these markers or populations were unique to a particular tissue type, with each tissue class including a diverse mixture of phenotypes, with only the relative intensity of markers (Figure 1G) and cluster frequency (Figure 1F) changing. Looking at antigen exposure through the Nur77 reporter of TCR engagement, antigen exposure was highest among CD69$^+$ Treg cells (Figures 1H and 1I). Together, these results demonstrate that Treg cells are found in nearly all tissues, with a high phenotypic similarity across non-lymphoid non-gut tissues.

A key requirement for comparative tissue phenotyping is the ability to discriminate between cells dwelling in the tissue and those captured due to vascular contamination. Here, we used perfusion or anti-CD45 antibody vascular labeling to identify and gate out the vascular-exposed Treg cell population (Figures S2A and S2B). Although the residual (post-perfusion) i.v. anti-CD45$^+$ cells are generally interpreted as blood contamination, and here, they were removed from the tissue Treg cell population, the residual vascular component of Treg cells in these tissue preparations was phenotypically intermediate between the i.v. CD45$^-$ tissue Treg cell compartment and the blood (Figures S2C–S2E). Further, an i.v. CD45^{int} Treg cell population was observed, with phenotypes intermediate between the residual vascular and tissue-based populations, consistent with a perivascular or trans-vascular Treg cell population with partial vascular shielding (Figures S2C–S2E). This result was unlikely to be driven by isolation effects, as the optimized tissue preparation approach used changed yield but not phenotype (Figures S2F–S2L). The residual vascular and peri/trans-vascular Treg cell populations are therefore more likely to represent transitional cells in the process of *in situ* differentiation than random vascular contamination.

Tissue Treg cells are shaped by age and microbiome

We next sought to determine the degree to which sex, age, and microbiome influence the tissue Treg cell niche and phenotype. For both tissue Treg cell frequency and phenotype, there were few differences between male and female mice, other than increased numbers of Treg cells in the salivary glands of female mice and a trend toward increased Treg cells in the white adipose tissue of male mice (Figures S3A–S3D). To assess the

(E and F) (E) tSNE representation with FlowSOM cluster overlay of high-parameter flow cytometry data on Treg cells grouped into the five tissue group categories, with (F) FlowSOM cluster frequency.

(G) Flow cytometry histograms showing key features from each Treg cell category.

(H and I) (H) Flow cytometry histograms of Nur77 expression within naive, activated, and CD69$^+$ Treg cells from the major tissue classes, with (I) quantification across multiple tissues. Data in F and I are presented as mean ± SE with p values derived from two-way ANOVA with Tukey's multiple comparisons.

See also Figures S1 and S2.

Please cite this article in press as: Burton et al., The tissue-resident regulatory T cell pool is shaped by transient multi-tissue migration and a conserved residency program, Immunity (2024), https://doi.org/10.1016/j.immuni.2024.05.023

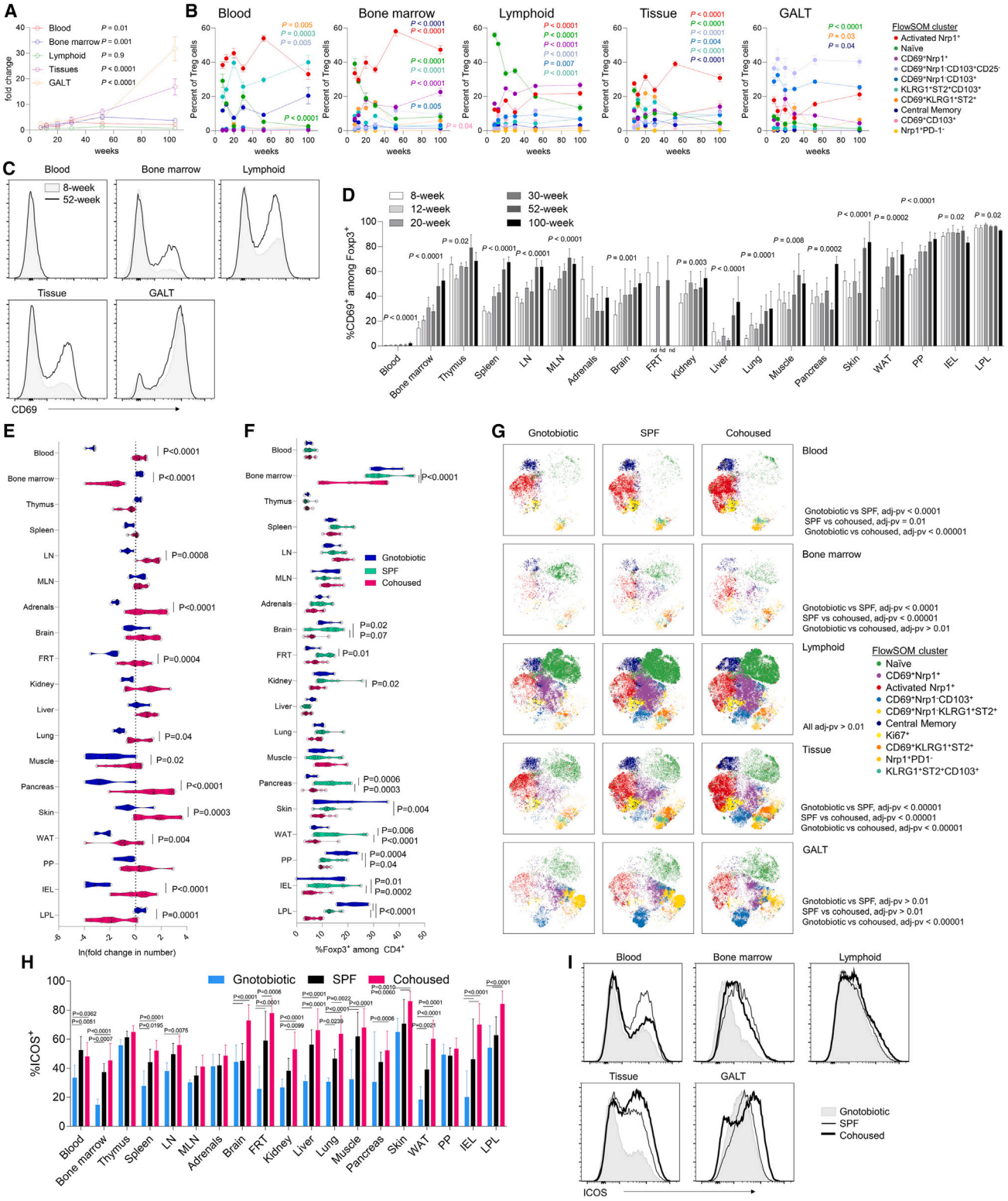

Figure 2. The tissue-resident Treg cell niche is shaped by aging and microbiome

Mice were perfused and assessed by flow cytometry for tissue Treg cell number and phenotype at 8, 12, 20, 30, 52, and 100 weeks of age (n = 5–12).

(A and B) (A) Fold-change in Treg cell number in the blood, bone marrow, lymphoid tissues, non-lymphoid tissues, and gut-associated tissues, and (B) quantitative change in phenotypic clusters, based on annotated tSNE clusters. p values refer to effect of age.

(C and D) (C) Histogram of CD69 expression at 8 and 100 weeks of age and (D) frequency of CD69$^+$ Treg cells over age and tissue. p values refer to effect of age.

(legend continued on next page)

effect of age, we typed the tissue Treg cell population from aging mice. Tissue Treg cells increased 5- to 20-fold across the non-lymphoid organs (Figure 2A), with the largest increases observed in white adipose tissue and liver (Figure S4A). The largest average increase was in gut-associated tissues, although this was driven almost exclusively by the lamina propria leukocyte (LPL) Treg cell population (Figure S4A). The frequency of Treg cells within the tissue CD4$^+$ T cell population was largely stable with age, with the exception of muscle and white adipose tissue, indicating that the fold-increase was driven by an (inflammatory) expansion in the total CD4$^+$ T cell niche (Figure S4B). At a phenotypic level, phenotypic adaptation intensified with age (Figure S4C), with relative enrichment of the CD69$^+$ resident populations over time (Figures 2B–2D). This result is consistent with both models of gradual accumulation of residential Treg cells and with age-dependent expansion of the cellular niche for residential Treg cells within the tissue.

Finally, we measured the impact of the microbiome on tissue Treg cells by comparing the standard SPF-housed mice to both gnotobiotic (germ-free) and microbial "re-wilded" mice. Although effect sizes were lower than observed in CD8$^+$ T cells,[28] a moderate increase in Treg cell number was associated with increased microbial complexity across the body, with the exception of the bone marrow and the LPL population of the gut, where the opposite occurred (Figure 2E). These effects were largely driven by changes in the total CD4$^+$ T cell infiltrate, as the frequency of Treg cells within the CD4$^+$ T cell compartment was stable with microbiome changes. The exception to this was the bone marrow and LPL compartments, where both the frequency of Treg cells within CD4$^+$ T cells and the absolute number of Treg cells fell markedly in re-wilded mice (Figures 2E and 2F), potentially reflecting displacement by effector CD8$^+$ T cells. Unlike that of CD8$^+$ T cells,[28] Treg cell phenotype was relatively stable with the changing microbial complexity (Figures 2G and S4D), other than ICOS elevation (Figures 2H and 2I). Together, these results suggest that the tissue Treg cell niche is numerically expanded but phenotypically preserved by both age and microbial challenge.

Overlapping molecular determinants of tissue Treg cell residency

To take a detailed, unbiased analysis of the tissue Treg cell transcriptome, we performed a high-depth bulk transcriptomics analysis of purified Treg cells from the blood, lymphoid tissues (spleen, lymph nodes, Peyer's patches), gut tissues (intraepithelial leukocyte [IEL] and LPL), and a representative selection of non-lymphoid non-gut tissues (liver, lung, pancreas, and kidney). Global analysis of the Treg cell populations found similar transcriptional profiles for the gut tissue and non-lymphoid tissue Treg cell populations (Figure 3A). Using pairwise comparisons, the Treg cell populations purified from non-lymphoid tissues (liver, lung, pancreas, and kidney) demonstrated highly similar transcriptional profiles, with ~95% transcriptional correlation (Figure 3B). IEL and LPL Treg cells showed similar transcriptional similarities to each other. The largest differences observed between the blood Treg cells and LPL Treg cells still demonstrated >85% transcriptional correlation (Figure 3B). The small transcriptional differences observed in pairwise comparisons of the selected tissue Treg cell populations were largely non-significant, with the largest set of transcriptional differences being genes with reduced expression in blood Treg cells (Figures 3C and 3D), including migration-associated genes and effector cytokines (Figure 3E). Pathway analysis of differential expression across tissue classes identified the strongest differences clustered within cytokine-cytokine receptor interactions, extracellular matrix-receptor interaction, and cell adhesion molecules (Figure 3F). Integrins and chemokine receptors were prominent among these changes, although the only class of tissue Treg cells with a unique signature were gut Treg cells, with elevated *Ccr9* and *Ccr5* and lower *Itgb1* and *Sell*. An interactive analysis resource based on these data, providing cross-tissue comparisons and pathway analysis, is available at https://www.bioinformatics.babraham.ac.uk/shiny/expressionViewer/.

We sought to functionally test selected tissue-residency candidates, including those canonically elevated in tissue Treg cells (CD69, ST2, KLRG1, CD103[20]), factors proposed as requirements for tissue Treg cell function (Blimp1[29] and basic leucine zipper transcription factor, ATF-like [BATF][30]), genes involved in tissue lymphocyte migration (CD11a and sphingosine-1-phosphate receptor 2 [S1PR2][31]), amphiregulin (Areg) as a candidate for tissue-specific function,[23] and Hif1α proposed to function in lymphocyte adaptation to tissue oxygen levels.[32] These candidates are expressed across a broad set of non-lymphoid non-gut tissues, at both the protein and RNA level (Figures 4A and 4B). We assessed mixed bone marrow chimeras with 50%:50% reconstitution of bone marrow from wild-type and mice deficient for *Cd69*, *Il1rl1* (ST2), *Itgal* (CD11a), KLRG1, *S1pr2*, *Batf*, or *Hif1a* (HIF1α), or with conditional deficiency in *Prdm1* (Blimp1) (Data S1). We also generated and assessed *Areg*-deficient mice, *Itgae*-deficient (CD103) mice, and *Foxp3*-^{CreERT2} *CD69*^{flox} mice (Data S1). We used a summary matrix to assess the change in tissue Treg cell frequency across each of 15 different tissues in each of these 10 genetic deficiency mouse strains, considering both Treg cell as a proportion of CD4$^+$ T cells (Figure 4C) and the absolute number of Treg cells within each tissue (Figure 4D). Despite their signature status, we found most of

(E and F) (E) Specific-pathogen-free (SPF)-housed mice, gnotobiotic (germ-free) mice, and wild-exposed co-housed mice (n = 9, 6, 12) assessed by flow cytometry for tissue Treg cell number and phenotype. Fold-change in tissue Treg cell number per tissue, and (F) frequency of Treg cells within CD4$^+$ T cell population per tissue.

(G) Phenotype of tissue Treg cells in blood, bone marrow, lymphoid tissues, non-lymphoid tissues, and gut-associated tissues displayed as tSNE of flow cytometry markers.

(H and I) (H) Inducible T cell costimulator (ICOS) expression over microbial exposure and tissues, within the Treg cell population, with (I) amalgamated histograms in tissue classes.

Data in A, B, D, and H are presented as mean with SE. For A, B, and D, p values derive from linear regression, testing for non-zero slope. For E, F, and H, a two-way ANOVA with Tukey's multiple comparisons was used.

See also Figures S3 and S4.

Please cite this article in press as: Burton et al., The tissue-resident regulatory T cell pool is shaped by transient multi-tissue migration and a conserved residency program, Immunity (2024), https://doi.org/10.1016/j.immuni.2024.05.023

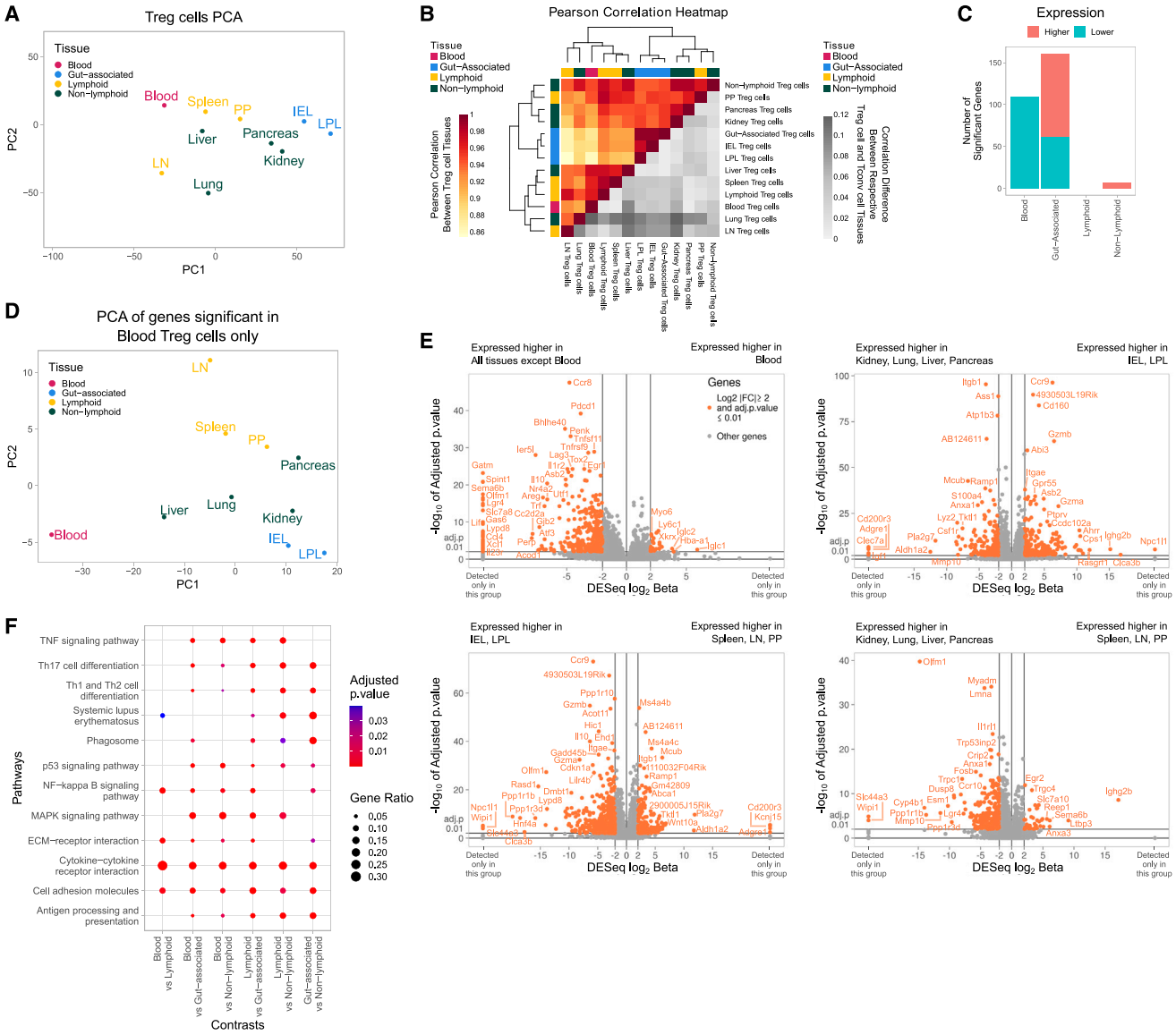

Figure 3. Transcriptional unity among tissue Treg cells

Treg cells were purified from the tissues of perfused *Foxp3*$^{Thy1.1}$ mice for RNA sequencing (RNA-seq) analysis.

(A) Principal-component analysis (PCA) of the Treg cell tissue mean expressions illustrating the broad clustering of the tissues in their respective tissue groups (n = 3, median value for each tissue shown. PCA with individual values is available through the online resource).

(B) Pearson correlation heatmap showing the similarity of the different Treg cell tissue mean expressions as well as the overall means of the four organically clustered tissue groups. Additionally, the magnitude of the respective Pearson correlations for Tconv cells between tissues and tissue groups are contrasted with the magnitude of Treg cell correlations for the same comparisons, to visualize the similarity of the transcriptional change.

(C) The number of genes persistently increased or decreased in expression in the respective tissue group when contrasted with each remaining tissue group pairwise.

(D) PCA of the Treg cell tissue mean expression using only the 109 genes persistently decreased in expression in blood Treg cells in (C).

(E) Volcano plots of the differential expression analyses. Blood Treg cells are contrasted with the means of all other Treg cell samples, followed by pairwise contrasts of the remaining three tissue groups.

(F) Dot plot showing the comparative overview of some of the various Kyoto Encyclopedia of Genes and Genomes (KEGG) pathways enriched in the gene set enrichment analysis.

these residency genes had little impact on Treg cell number. CD69-deficiency resulted in only a mild decrease in Treg cell numbers across the tissues. KLRG1-deficiency and BATF-deficiency drove an elevation and a reduction, respectively, in the number of Treg cells across most non-lymphoid tissues (both gut and non-gut), CD11a-deficiency reduced Treg cells entering all tissues surveyed, and Blimp1-deficiency enhanced tissue Treg cell numbers in the gut tissues (Data S1). Few unique gene-tissue associations were observed to control tissue Treg cell numbers, other than an increase in Treg cells in the skin of

Please cite this article in press as: Burton et al., The tissue-resident regulatory T cell pool is shaped by transient multi-tissue migration and a conserved residency program, Immunity (2024), https://doi.org/10.1016/j.immuni.2024.05.023

CellPress
OPEN ACCESS

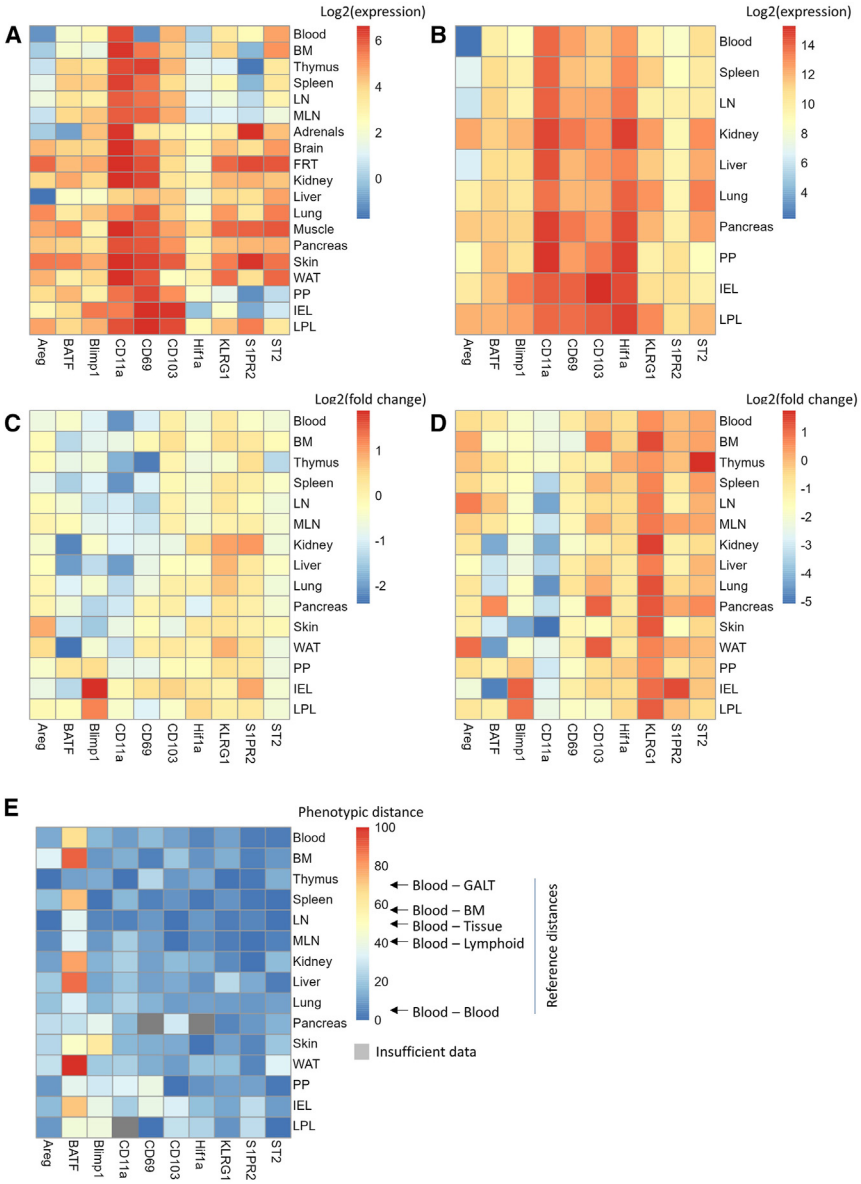

Figure 4. Conserved molecular determinants for Treg cell tissue residency

(A) Relative expression of Areg, BATF, Blimp1, CD11a, CD69, CD103, HIF1a, KLRG1, S1PR2, and ST2, as measured by flow cytometry and visualized as $\log_2$(expression), within tissue-resident Treg cells (n = 4).

(B) Relative mRNA expression of *Areg*, *Batf*, *Prdm1*, *Itgal*, *Cd69*, *Itgae*, *Hif1a*, *Klrg1*, *S1pr2*, and *Il1rl1*, as measured by RNA-seq and visualized as $\log_2$(expression), within tissue-resident Treg cells (n = 3).

(C) In separate experiments, the number and phenotype of tissue Treg cells were assessed in mixed bone marrow chimeras with 50%:50% deficient:wild-type bone marrow, containing bone marrow from BATF, Blimp1 (conditional), CD11a, CD69, Hif1a, KLRG1, S1PR2, or ST2 deficient bone marrow (n = 5, 6, 6, 4, 5, 4, 6, 4) or from comparison of wild-type and deficient mice for Areg and CD103 (n = 4, 4).

(D) Cells stained as positive for intravenous anti-CD45 antibody were excluded. Treg cell frequency among $CD4^+$ T cells and (D) absolute number in deficient relative to wild-type ($\log_2$(fold-change)).

(E) Phenotype change, between wild-type and deficient Treg cells, from each tissue. Euclidean distances are rescaled from 0 to 100, based on maximum changes, and reference values are based on the median distances between wild-type Treg cells of different tissue sources. Gray indicates insufficient events for phenotypic assessment.

See also Data S1.

Areg-deficient mice, which could be due to local inflammation from Treg cell-extrinsic functions, and an increase of S1PR2-deficient Treg cells in the kidney (Data S1). We further assessed the effect of genetic deficiency on Treg cell phenotype in each genetic deficiency. Measuring global phenotypic difference only minor shifts were observed in Treg cell phenotype across the matrix of tissue types and genetic deficiencies (Figure 4E), with most phenotypic difference shifts being on the order of natural variation across mice. The exceptions were genetic deficiency in BATF and Blimp1. Mixed chimerism of BATF resulted in a loss of the $CD69^+KLRG1^+ST2^+$ Treg cell population in every tissue. This had the largest numerical impact on Treg cell numbers in non-lymphoid organs, while the Treg cell population in lymphoid tissues was substituted by elevated frequencies of naive/resting Treg cells (Data S1). Mixed chimerism of CD4-Cre *Blimp1*^{flox} bone marrow demonstrated a strong loss of the $CD69^+Nrp1^-CD103^+$ Treg cell population within the gut and a partial loss of the $CD69^+ST2^+KLRG1^+$ Treg cell population across the non-lymphoid tissues (Data S1). Thus, while tissue-resident Treg cells express this signature gene set, expression of most members, other than BATF and Blimp1, is largely independent of the other members, and observed changes were pan-tissue rather than tissue-specific. Together, these results suggest that not only do tissue Treg cells show a unified phenotype, but they also appear to share the same key molecular determinants for residency.

Tissue Treg cells are short-term residents

The similarity in phenotypes and molecular dependency exhibited by tissue-resident Treg cells suggests that either the phenotypic plasticity of Treg cells is sharply curtailed, preventing niche-driven specialization, or that the dwell time for residency is of a limited duration, limiting divergence. To directly test the homeostatic population flows for tissue Treg cells, we performed a large multi-time point parabiotic experiment, consisting of CD45.1 mice parabiosed to CD45.2 mice, providing a common circulatory system, and assessed for displacement of tissue-resident cells. The use of multiple time points in this experimental design allowed for the estimate of dwell times rather than a simple assignation of residency at a single time

Please cite this article in press as: Burton et al., The tissue-resident regulatory T cell pool is shaped by transient multi-tissue migration and a conserved residency program, Immunity (2024), https://doi.org/10.1016/j.immuni.2024.05.023

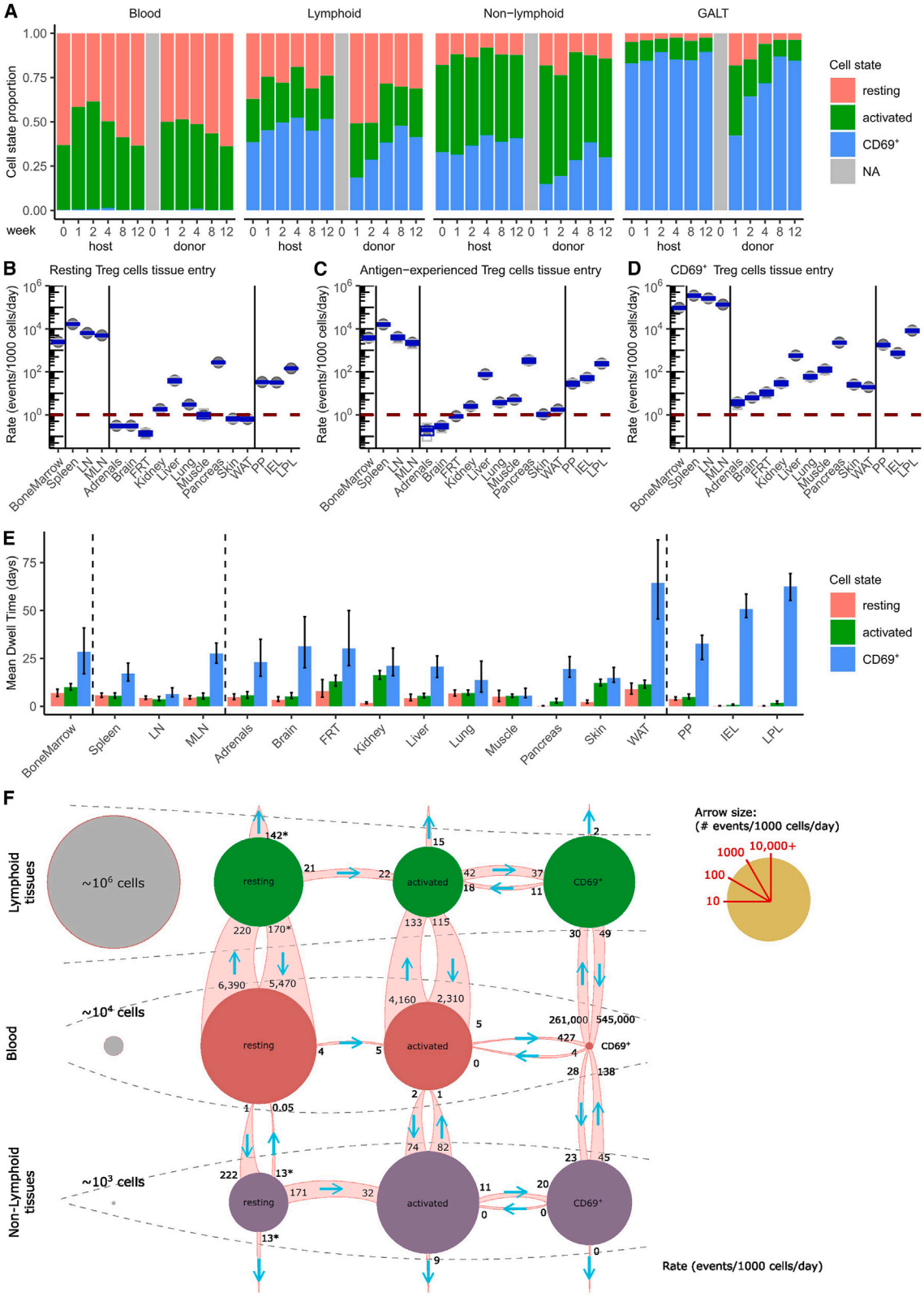

Figure 5. Limited dwell times of tissue Treg cells

Figure360▷ For a Figure360 author presentation of this figure, see https://doi.org/10.1016/j.immuni.2024.05.023.

CD45.1 mice were parabiosed to CD45.2 mice, perfused and sacrificed at weeks 1, 2, 4, 8, and 12 (n = 11, 12, 18, 16, 14).

(legend continued on next page)

Please cite this article in press as: Burton et al., The tissue-resident regulatory T cell pool is shaped by transient multi-tissue migration and a conserved residency program, Immunity (2024), https://doi.org/10.1016/j.immuni.2024.05.023

CellPress
OPEN ACCESS

point. Using the division of tissue Treg cells into the states of resting CD44$^-$CD62L^{hi} cells, activated CD44$^+$CD62L^{lo} cells, and CD69$^+$ cells, the CD69$^+$ population showed the slowest displacement kinetics, consistent with the "resident" status of these cells (Figure 5A). To calculate the residency dwell time of tissue Treg cells, we developed a probabilistic Markov chain model using Bayesian analysis. The best-fit Markov models exhibited large differences in entry rates, with non-lymphoid tissues having 1,000-fold lower entry than lymphoid tissues (Figures 5B–5D). There was, however, diversity within the tissues, with some tissues (gut, liver, pancreas) having 100-fold higher entry than others (adrenals, brain). Tissue entry rates modeled for CD69$^+$ Treg cells (Figure 5D) were ~10-fold higher than those modeled for resting or activated Treg cells (Figures 5B and 5C), across all tissue types. Modeled dwell times for resting Treg cells and activated Treg cells were short across all tested tissues, on the order of ~5 days, with most of the residency exhibited by the CD69$^+$ population (Figure 5E). Within lymphoid tissues, even the residency of the CD69$^+$ fraction was short: 3 days for lymph nodes, 17 days for spleen, and 4 weeks for mesenteric lymph nodes (Figure 5E). The average dwell time for CD69$^+$ Treg cells within non-lymphoid tissues was around 3 weeks, with white adipose tissue extending out to 8 weeks (Figure 5E). Gut-tissue CD69$^+$ Treg cell dwell time was at the upper end of this range, with 7–8 weeks for IELs and LPLs (Figure 5E). Building a cellular population model featuring the blood, median lymphoid tissue, and median non-lymphoid tissues (Figure 5F), lymphoid tissue kinetics were driven by the greatly elevated entry rates, with non-lymphoid tissues being seeded through direct entry of CD69$^+$ Treg cells from the blood and by indirect seeding through highly transient resting/activated Treg cells, of which a small fraction increased CD69 (Figure 5F). After the median dwell time of 3 weeks, the majority of these CD69$^+$ Treg cells were modeled to leave the tissue (Figure 5F). Consistent with this model of reversible residency, *KLRG1^{Cre} RosaA14* mice, with fate-mapped KLRG1 Treg cells, had substantial populations of ex-KLRG1-expressing Treg cells across the tissues, with activated but not naive/resting phenotypes (Data S1). Together, these data formally demonstrate a short dwell time for tissue-resident Treg cells and support a circular migration model where activated Treg cells enter, differentiate, transiently reside, and leave.

A common pool of tissue Treg cells seed multiple tissues

Our data demonstrate that tissue Treg cells, across a large range of tissues, initiate a common molecular program upon seeding tissues, with transient residency. Although incompatible with a long-term residency model, these data are compatible with two distinct models: clonally restricted circular trafficking or pan-tissue trafficking. Under the first model, Treg cells from each tissue would show circular migration between one non-lymphoid tissue and the lymphoid tissues, providing for clonal restriction while giving short dwell times. Under the second model, Treg cells would show the capacity to seed multiple non-lymphoid tissues, with circular flow resulting in the distribution of tissue Treg cell clones across multiple tissues. To distinguish between these two models, we assessed both the clonality of tissue Treg cells in a subset of non-lymphoid tissues and the capacity for tissue Treg cells to cross-seed alternative tissues.

We first investigated clonal sharing between non-lymphoid tissues, using the recombined TCR as a clonal barcode. We performed single-cell sequencing of purified tissue-resident Treg cells from four independent mice, focusing on the blood as a reference population and the kidney, pancreas, liver, and LPL as representative non-lymphoid tissue populations. TCRαβ protein-level sequences were used as markers of clonality. Despite being unmanipulated mice, with fully polyclonal repertoires, tissue-resident Treg cells showed a high degree of clonal sharing within mice (Figure 6A). TCR clones from Treg cells purified from the liver, pancreas, and kidney were highly represented within the blood and alternative non-gut tissues tested (Figure 6A). By contrast, the TCR clones identified in Treg cells purified from the LPL population were only rarely observed in the non-gut tissues, despite high levels of sharing within mice (Figures 6A–6C). To quantify the relative degree of sharing between tissues, we used an extracted half-sample as the comparator. Between liver, pancreas, and kidney comparisons, an average of 7.5% of TCR clones were shared, while LPL Treg cells only shared, on average, 1.3% of TCR clones with these non-gut tissues (Figure 6B). Normalized to the sharing rate observable within a single tissue, the relative sharing rate was ~66% between non-gut tissues and 12% between the LPL samples and the non-gut tissues (Figure 6D). These data suggest that while the gut Treg cell population may largely follow the clonally restricted circular trafficking model, the preponderance of common clones in the non-gut, non-lymphoid tissues is of a pan-tissue clonality. Reanalysis of a multi-tissue major histocompatibility complex (MHC) class I immunopeptidome dataset[33] suggested that only 1.4% of peptides are tissue-restricted (Figure S5). Although Treg cells recognize antigen presented on MHC class II, these data demonstrate the potential shared peptidome available for pan-tissue clonal Treg cells.

To formally test the functional outcome conferred upon tissue Treg cells by these clonotypic TCRs, we sought to biologically challenge the identified pan-tissue Treg cell TCRs via a retrogenic system. In order to multiplex the retrogenic assay and create a more representative perspective on tissue Treg cell TCRs, we adapted the Pro-Code epitope-based barcoding system,[34,35] which enables cell barcode detection at the protein level using a triplet combination of linear epitopes. Membrane-bound Pro-Codes were incompatible with *in vivo* lymphocyte-tracing, so we generated a Pro-Code variant, flow cytometry-optimized Pro-Codes (named here FlowCodes). Epitope fusion with histone 2B provided a long half-life and fixation-resistant

(A) Frequency of resting, activated, and resident Treg cells within the blood and tissues, for host cells and donor cells.
(B–D) (B) Markov chain results for entry rates for resting Treg cells, (C) activated Treg cells, and (D) CD69$^+$ Treg cells.
(E) Markov chain modeling was used on the parabiotic data to estimate Treg cell dwell times among the CD44$^-$CD62L^{hi}, CD44$^+$CD62L^{low}, and CD69$^+$ Treg cell subsets. Model estimates with 80% credibility interval.
(F) Based on the Markov chain models for Treg cells, the primary population flows between blood and tissues, indicating population size and the frequency of key events. *For tissue-dwelling resting Treg cells, the model does not distinguish between cell death and return to the blood.

Please cite this article in press as: Burton et al., The tissue-resident regulatory T cell pool is shaped by transient multi-tissue migration and a conserved residency program, Immunity (2024), https://doi.org/10.1016/j.immuni.2024.05.023

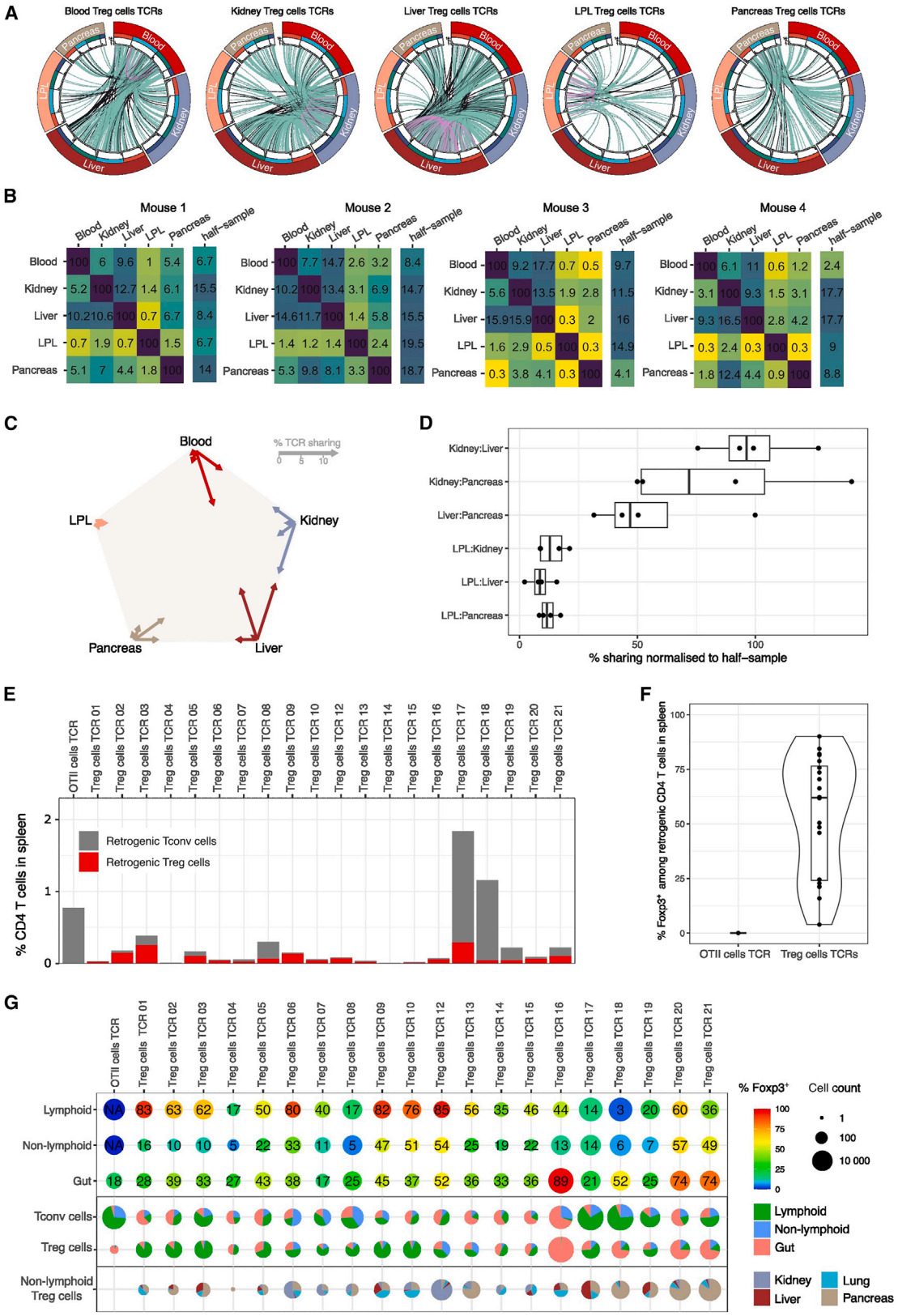

(legend on next page)

Please cite this article in press as: Burton et al., The tissue-resident regulatory T cell pool is shaped by transient multi-tissue migration and a conserved residency program, Immunity (2024), https://doi.org/10.1016/j.immuni.2024.05.023

CellPress
OPEN ACCESS

Pro-Code (Figures S6A and S6B). Into each of 21 FlowCode retrovirus backbones, we inserted a paired TCRα/TCRβ chain from 20 tissue Treg cell TCR clones and the OTII TCR. 10 clones were selected from highly distributed tissue Treg cells (Figure S6C) and 10 clones based on the highest detection in individual tissues (Figure S6D), creating a repertoire representative of the public clone repertoire (Figures S6E and S6F). The co-expression of a retrogenic TCR with a unique FlowCode allowed cells expressing a specific TCR to be tracked by flow cytometry in a polyclonal environment. 10 weeks after transplantation, differentiated CD4$^+$ T cells expressing the different TCRs were assessed for tissue representation and Treg cell fate. Although control retrogenic clones, bearing the OTII TCR only, remained conventional Foxp3$^-$ cells, an average of 60% of retrogenic cells bearing tissue Treg cell TCRs spontaneously entered the Treg cell lineage (Figures 6E and 6F), comparable to other *in vivo* TCR transgenic Treg cell induction rates.[36–41] Analysis of retrogenic clones at the tissue level revealed broad ability to enter lymphoid, non-lymphoid, and gut-associated tissues (Figures 6G and S6G). Of the ten retrogenics cloned from Treg cells found in widely dispersed tissues, nine were found as tissue Treg cells in multiple non-lymphoid tissues, with the exception (TCR04) found only in the pancreas (Figures 6G and S6G). Of the ten retrogenics cloned from Treg cells based on high-frequency detection within a single tissue, all were found as tissue Treg cells in multiple non-lymphoid tissues (Figures 6G and S6G). Five clones (TCR13/14/15/17/19) showed broadly balanced tissue representation, indicating that the initial detection as tissue-restricted may have been driven by stochastic sampling. By contrast, 5 clones showed a strong, but not exclusive, tissue bias, aligning with the source of initial identification: TCR12 in the kidney, TCR20/TCR21 in the pancreas, and TCR16 and TCR18 in the LPL of the gut (Figures 6G and S6G). No correlation was observed between single-tissue/multi-tissue status and CD69 expression (Figure S7), indicating residency program initiation can occur in multiple organs for a single clone. Together, these results demonstrate that a representative set of tissue Treg cell TCRs confer upon CD4$^+$ T cells a Treg cell fate, with the majority of TCRs driving a pan-tissue migration and residency profile and only a minority of TCRs driving a tissue-biased distribution.

As an independent test of the pan-tissue Treg cell model, we assessed the capacity of tissue Treg cells to migrate into different organs. First, we returned to the parabiosis system. The equilibration of tissue Treg cell frequency following parabiosis (Figure 5) is consistent with both single-tissue or multi-tissue recirculation patterns. We posited that Treg cells entering the system containing a novel tissue from a donor mouse lacking that tissue would be at a competitive disadvantage in repopulation under the single-tissue recirculation model, but would show a similar capacity to populate under a multi-tissue recirculation model. To create this unexperienced organ competitive test, we compared the repopulation of the female reproductive tract in female:female parabionts (donor-experienced) to male:female parabionts (donor-naive). Comparing the frequency of host cell replacement by donor cells, the female reproductive tract was equally populated by donor cells from male mice as by donor cells from female mice (Figure 7A). The male donor and female donor Treg cells were not only able to repopulate the female reproductive tract with equal efficiency, but they were also phenotypically indistinguishable (Figure 7B).

Second, to assess the speed at which the tissue Treg cell compartment could be reconstituted, we transferred whole splenocytes into Rag-deficient mice. By measuring the quantitative (Figure 7C) and qualitative (Figure 7D) reconstitution of the compartment within different tissues, we observed that the tissue Treg cell population could be rapidly reconstituted from lymphoid Treg cells. Within 2–4 weeks, the population of tissue Treg cells was at 10%–100% of the homeostatic level, across the non-lymphoid tissues (Figure 7C), and even at the 2-week time point, those Treg cells that had reentered the tissues had increased expression of CD69 to levels similar to that of

Figure 6. Extensive clonal sharing among tissue Treg cells imparts pan-tissue functionality

(A) *Foxp3$^{Thy1.1}$* mice at 16 weeks of age were injected with intravenous anti-CD45 antibody label prior to fluorescence-activated cell sorting (FACS) of Treg cells from blood, kidney, liver, pancreas, and LPL ($n = 4$) for analysis by single-cell TCR sequencing. Cells stained as positive for intravenous anti-CD45 antibody were excluded during sorting. Chord diagrams illustrate, for each tissue origin, the Treg cell TCR found to be shared between different tissues. For each tissue (main sector) of each mouse (sub-sector), the frequency-ranked TCR repertoire is shown as a bar plot. Lines joining 2 repertoires indicate a clonotype sharing between 2 tissues of the same mouse (green), the same tissue type between different mice (pink), or different tissue types in different mice (black).

(B) Heatmaps showing for each mouse the percentage of cells from x-tissue having a TCR also observed in y-tissue. Since sharing between small, diverse repertoires is not expected to result in high sharing percentage even if the same sample would be compared with itself, for each x-tissue, the sharing half-sample subpool compared with the other half of x-tissue sample in indicated on the right (average value of 100 sub-pools).

(C) Percentage of TCR sharing between tissue within each mouse, averaged for the 4 analyzed mice, illustrated the length of an arrow pointing toward the tissue.

(D) Percentage of TCR sharing between non-gut tissue pairs (kidney, pancreas, lung) and gut-non-gut tissue pairs (LPL with kidney, pancreas, or lung), relative to the split sample TCR sharing rates. Box-and-whisker plots with mean and quartiles.

(E) 20 tissue Treg cell TCRs were selected from single-cell sequencing data, comprising 10 TCRs selected on the basis of distribution width and 10 TCRs selected on the basis of tissue frequency. The selected TCR panel was cloned into FlowCode retroviruses, transduced into Rag-deficient bone marrow stem cells, and used to reconstitute irradiated mice. After 10 weeks, mice were injected with anti-CD45 antibody, gating out vascular cells, and tissue samples were prepared for analysis by flow cytometry.

(F) Quantification of Tconv cells and Treg cell T cells from each retrogenic TCR clone, as a percentage of total CD4$^+$ T cell frequency within the spleen, with (F) an average (and standard deviation) frequency of Treg cell fate within each clone.

(G) Individual results from T cells derived from each of the FlowCode retrogenic TCRs, across the assessed tissues. Top, absolute cell count of detected CD4$^+$ T cells for each clone (size) together with the frequency of Treg cells within the population (color; percentage listed on each sample). Frequencies are calculated from the aggregate of lymphoid (spleen, lymph node [LN]), non-lymphoid (kidney, lung, liver, pancreas), and gut (LPL) samples. Middle, for each retrogenic TCR clone, a pie chart visualizing the distribution of cells within the lymphoid, non-lymphoid, and gut compartments. Bottom, for non-lymphoid tissue Treg cells from each retrogenic TCR clone, a pie chart visualizing the distribution of cells within the non-lymphoid tissues.

See also Figures S5–S7 and Data S2.

Please cite this article in press as: Burton et al., The tissue-resident regulatory T cell pool is shaped by transient multi-tissue migration and a conserved residency program, Immunity (2024), https://doi.org/10.1016/j.immuni.2024.05.023

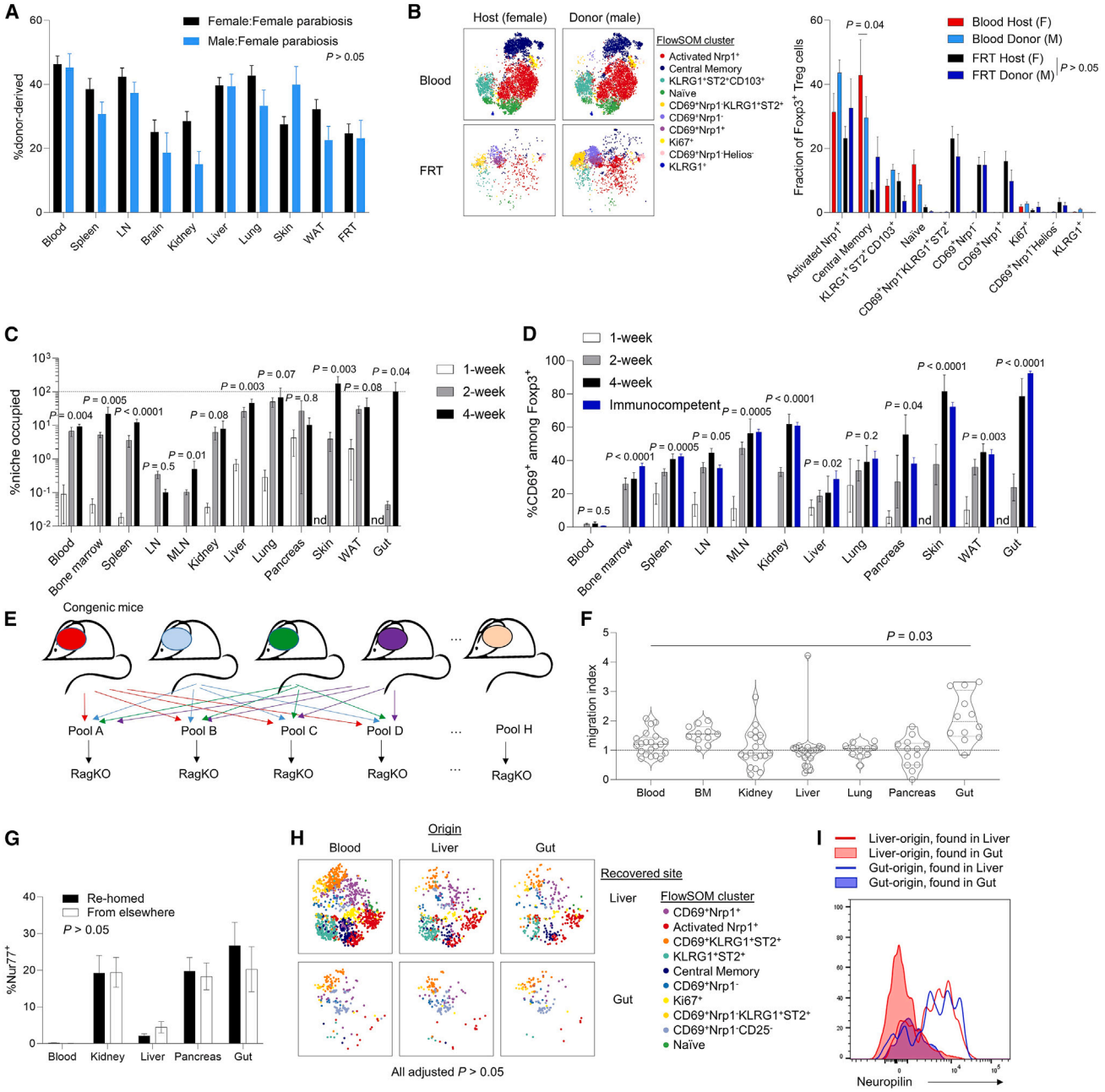

Figure 7. Tissue Treg cells retain multi-tissue homing capacity and phenotypic plasticity

(A) Proportion of incoming (donor-derived) Treg cells in perfused female mice when parabiotically paired to female vs. male mice (n = 18, 8). All male:female comparisons, $p > 0.05$ by Šídák's multiple comparison test.

(B) tSNE plots and quantification of phenotype on Treg cells from male:female parabiotic pairs. No statistically significant differences for tSNE crossentropy. Statistical testing on cluster distributions by two-way ANOVA with Tukey's multiple comparisons.

(C) Splenocytes were transferred into Rag-deficient mice, with the Treg cell compartment measured quantitatively after 1, 2, or 4 weeks of reconstitution, in reference to unmanipulated numbers (n = 6, 6, 3, 9). Mice were injected with intravenous anti-CD45 label, and positive cells excluded.

(D) Expression of CD69 on Treg cells within each organ post-reconstitution. p values in C and D derive from linear regression, testing for non-zero slope.

(E) Eight congenic-labeled pools of mixed tissue lymphocytes were generated, containing only one tissue from each mouse strain, to allow congenic tracing of tissue origin, and injected into Rag-deficient mice. Intravenous anti-CD45-labeled cells excluded.

(F) 4 weeks after the transfer of donor-tracked tissue pools, recipient mice were assessed for tissue Treg cell infiltration. Rehoming migration index was calculated for each donor tissue type (n = 7–11), normalized to no preference for rehoming. One-way ANOVA with Dunnett's post-test.

(G) Expression of Nur77 in Treg cells recovered post-transfer (n = 6–10). $p > 0.05$ by Šídák's multiple comparison test.

(H) tSNE plots showing phenotypic profiles of Treg cells recovered from the liver and gut, sub-divided based on origin.

(I) Neuropilin histogram of liver and gut origin Treg cells, recovered in the liver or gut.

All barcharts are shown as mean with SE.

Please cite this article in press as: Burton et al., The tissue-resident regulatory T cell pool is shaped by transient multi-tissue migration and a conserved residency program, Immunity (2024), https://doi.org/10.1016/j.immuni.2024.05.023

CellPress
OPEN ACCESS

homeostasis (Figure 7D). These data are consistent with a tissue Treg cell niche, with high capacity for rapid entry from the periphery.

Third, we performed a direct recirculation experiment. By extracting tissue-resident lymphocytes from 7 tissues from each of 8 antigenically marked strains, we could make mixed ex-tissue-resident lymphocyte pools, where the tissue-resident Treg cells extracted from each tissue had a unique antigenic marker combination (Figure 7E). These mixed pools were then injected into Rag-deficient hosts, and a migration index was calculated for re-entry of tissue-resident Treg cells into original tissue types. Although gut-purified Treg cells were biased toward re-entry into the gut, Treg cells originally isolated from the kidney, liver, lung, and pancreas showed no preference for re-entry (Figure 7F). Using Nur77 as a marker for TCR engagement, similar levels of antigen recognition were observed in the Treg cells regardless of whether they had rehomed from the original source tissue or had cross-populated (Figure 7G). Comparing gut-associated Treg cells to liver Treg cells, the cross-populating Treg cells exhibited a phenotype closer to the new host tissue than the originating host tissue (Figures 7H and 7I). Together, the parabiosis and tissue-transfer experiments strongly support a pan-tissue model for tissue Treg cell residency, whereby the same population of Treg cells is capable of repopulating multiple tissues, with only slight preferences for target tissues other than the gut.

DISCUSSION

The shared phenotype of tissue Treg cells and the evidence for a circular migration capacity leads to a parsimonious model of a pan-tissue Treg cell population. Under the pan-tissue model, activated Treg cells have the capacity to enter tissues at a low rate and be retained if antigen recognition occurs. This would lead to initiation of the generic tissue residency program for weeks to months before death or egress. Treg cells bearing a TCR capable of recognizing antigen within multiple tissues would percolate throughout multiple tissues over the lifetime of the cell. Rare clones with tissue-restricted antigen recognition would have a more specialized circular pattern, where dwell time is largely restricted to a single tissue, as observed with adipose tissue TCR clone (clone 53).[42] Both theoretical considerations (the small fraction of presented peptides that are tissue-restricted) and empirical data (agnostic rehoming capacity and shared TCR clones) necessitate such tissue-restricted clones being among the minority of tissue Treg cells. As Treg cell proliferation is driven by antigen recognition, multi-tissue Treg cells may bear a competitive advantage over mono-tissue Treg cells and, over time, grow to dominate the tissue repertoire. Although prior work used the seeding and specialization model, the data of those studies is consistent with the pan-tissue Treg cell model. For adipose Treg cells, which are at the more distinct end of our multi-tissue analysis, phenotypic[43] and TCR clonality[44] distinctiveness were originally identified in comparison to Treg cells from lymphoid organs. Likewise, the indefinite residency of adipose Treg cells was derived from parabiosis experiments at 4–6 weeks[44] (a parabiosis study at 12 weeks found no maintained residency,[45] consistent with our calculated dwell time). The pan-tissue model also allows us to reinterpret the complex data on tissue Treg cell "precursors."[46] Peroxisome proliferator–activated receptor γ (PPARγ), originally identified as an adipose-specific Treg cell signature gene[43] but here observed more broadly, is also expressed in a smaller number of Treg cells in lymphoid tissues. These cells are less diverse at the TCR level than other Treg cells and share clonality with Treg cells from the liver, skin, and adipose Treg cells.[46] Further, sorted PPARγ^+ cells could "seed" all three non-lymphoid tissues tested.[46] Similar findings are reported for KLRG1$^+$NFIL3$^+$ splenic Treg cells.[30] Under the seeding and specialization model, this data required the postulation of tissue Treg cell precursors prior to permanent seeding, which problematically requires TCR specificity assortment preceding tissue entry. Under the pan-tissue Treg cell model, the lymphoid PPARγ^+ Treg cells can be reinterpreted as recirculating tissue Treg cells. Although this idea had been considered and discarded in prior studies,[30] this dismissal was based on KLRG1 being considered an irreversible marker, while our fate-mapper data demonstrate KLRG1 expression is reversible in Treg cells. The pan-tissue Treg cell model is therefore more consistent with the existing literature.

These data point to both conserved and disparate features between tissue Treg cells and the conventional Trm cell populations. Beyond tissue residency, the striking feature conserved between tissue Treg cells and Trm cells is the phenotypic residency program, with markers such as CD69 and CD103 conserved across both populations. In the case of tissue Treg cells, signature genes were initially identified in single tissue and were labeled as unique in comparison to lymphoid Treg cells. Thus, markers such as KLRG1, ST2, and PPARγ were labeled as adipose Treg cell-specific[43,47] and Areg as muscle Treg cell-specific.[23] The same markers, when assessed in a pan-tissue manner, as here, are near-ubiquitous. The tissue residency program in Treg cells thus appears, like Trm cells, to be unified across tissues. We do not exclude "tilting" of the generic tissue-residency program by factors enriched in particular tissues, as observed in Trm cells,[48] although this potential is reduced by the limited dwell time of Treg cells in most tissue. Further enrichment of these same genes in particular tissues, or sex-based comparisons,[45] is more consistent with a relative enrichment of the generic tissue subset rather than the presence of a unique population. This also holds true for DNA methylation studies and chromatin accessibility studies, where differences between tissues are smaller than lymphoid-non-lymphoid comparisons.[30,49,50] The conservation of this signature, both across tissues and between tissue Treg cells and Trm cells, suggests the importance of the constituent genes for the adaptation of lymphocytes to tissues.

The key difference between tissue Treg cells and Trm cells is likely to be the nature of antigenic stimulation that turns on the residency module. As conventional T cells, primed by infections, the antigen exposure of Trm cells is temporally and spatially restricted. Of necessity this requires the residency signature to be "locked in" without continual antigenic stimuli, a program that may utilize Hobit, Runx, and Blimp.[16–18] By contrast, homeostatic tissue Treg cells recognize antigens without temporal restriction and with broader spatial distribution, enabling re-initiation on a continual basis. Indeed, in tissue Treg cells, the absence of such a transcriptional lock and the consequent sequential circulation-residency cycles would enable optimization of tissue distribution. The tissue phenotype may, in the

case of Treg cells, be controlled by the same regulators as the traditional activation pathway, with the phenotypic signature driven by chronic signaling rather than by expression of distinct transcription factors. Under this model, tissue Treg cells would not require a self-sustaining transcriptional lock; however, molecular mediators required for activation, such as BATF, would have even stronger phenotypic effects on tissue-residency phenotypes across a range of tissues, as observed here and elsewhere.[30,51]

A shared residency program initiated in pan-tissue Treg cells is not mutually exclusive with tissue-specific functional endpoints. From an evolutionary perspective, repurposing of homeostasis-restoring effector molecules on a tissue-by-tissue basis would enable a single regulatory module in tissue Treg cells to drive disparate physiological responses. Thus, effector molecules for tissue homeostasis, such as Notch ligand expression by skin Treg cells,[26] could allow a single mediator to feed into diverse responses across multiple tissues. A clear example of this pleiotropy is Areg. First proposed as a muscle Treg cell-specific effector of enhancing injury repair,[23] Areg is widely produced by Treg cells and capable of suppressing neurotoxic astrogliosis in the brain,[52] driving alveolar regeneration in the lung,[53,54] regulating angiogenesis in the limbs,[55] suppressing renal and hepatic inflammation,[56,57] and driving corneal healing in the eye.[58] In each case, source and effector molecule are conserved, while the response cell and initiated reparative program differ markedly.

Limitations of the study

The work here concentrated on the homeostatic state, and it is likely that aspects of tissue Treg cell biology are altered during tissue inflammation. Here, we found Treg cell number and phenotype were independent of the IL-33/ST2 pathway, while in the inflamed muscle,[59,60] heart,[61] and kidney,[62] IL-33 alarmin is released and ST2 is a potent regulator. This effect may also account for the less striking sexual dimorphism of adipose Treg cells observed in our study (a colony-dependent effect has previously been noted[63]), with the intense adipose tissue residency phenotype in other colonies linked to sex-associated inflammation.[45,64] Inflammation may also change the clonality rules described here, with both muscle[65] and heart[61] inflammation altering tissue Treg cell TCR repertoires. Finally, this study has been performed exclusively in mice, and further tissue-based analysis of human Treg cells is needed to determine whether features differ in humans.

STAR★METHODS

Detailed methods are provided in the online version of this paper and include the following:

- KEY RESOURCES TABLE
- RESOURCE AVAILABILITY
  - Lead contact
  - Materials availability
  - Data and code availability
- EXPERIMENTAL MODEL AND STUDY PARTICIPANT DETAILS
  - Mouse strains and strain generation
- METHOD DETAILS
  - Mouse procedures
  - Tissue preparation
  - Murine tissue flow cytometry
  - FlowCode cloning
  - RNAseq
- QUANTIFICATION AND STATISTICAL ANALYSIS
- ADDITIONAL RESOURCES

SUPPLEMENTAL INFORMATION

Supplemental information can be found online at https://doi.org/10.1016/j.immuni.2024.05.023.

ACKNOWLEDGMENTS

This work was supported by the ERC Consolidator Grant TissueTreg (to A.L.), the Wellcome Trust (to A.L.), and the BBSRC through BBS/E/B/000C0427, BBS/E/B/000C0428, and the Core Capability Grant. The authors acknowledge the KU Leuven FACS Core and Babraham Institute BSU, Flow Cytometry, Sequencing, and Bioinformatics Cores. We thank Jeason Haughton, Amy Dashwood, Lidia Yshii, Ana Laura Calvanese, Wenson Karunakaran, Stephanie Lienart, Kailash Singh, Alena Moudra, Ntombizodwa Makuyana, and Daria Vdovenko for technical assistance. We thank Julie Stockis and Tim Halim (CRUK Cambridge) for their advice. For mouse strains, we acknowledge Lars Vereecke (VIB), Andrew McKenzie (LMB), Alexander Rudensky (Sloan Kettering), Michelle Linterman (Babraham Institute), Rahul Roychoudhuri (University of Cambridge), Pilar Lauzurica (Instituto de Salud Carlos III), Laurent Brossay (Brown University), Takaharu Okada (RIKEN), and Alex Gould (Francis Crick Institute). OTII-2A.pMIG II was a gift from Dario Vignali (University of Pittsburgh).

AUTHOR CONTRIBUTIONS

Conceptualization, J.D. and A.L.; data curation, O.T.B.; formal analysis, O.T.B., O.B., S.T., and V.G.; funding acquisition, A.L.; investigation, O.T.B., O.B., C.W., S.J., A.B., E.P., M.A., and P.L.; methodology, O.T.B., O.B., S.T., V.G., C.P.R., B.D.B., and J.D.; project administration, O.T.B., J.D., and A.L.; resources, H.I., S.M.S., and B.D.B.; software, O.T.B., O.B., S.T., V.G., S.A., L.B., and C.P.R.; supervision, O.T.B., S.A., J.D., and A.L.; validation, O.T.B. and O.B.; visualization, O.T.B., O.B., S.T., V.G., and L.B.; writing—original draft, O.T.B., O.B., and A.L.; writing—review and editing, all.

DECLARATION OF INTERESTS

A.L. and J.D. are founders of Aila Biotech Ltd. A.L. has served on advisory boards for Imcyse, Sangamo, Dualyx, and Enhanc3D. C.P.R. is currently employed at CSL Behring. S.T. is currently employed at Roche. S.J. and A.B. are currently employed at Janssen Pharmaceuticals.

Received: October 5, 2023
Revised: February 27, 2024
Accepted: May 24, 2024
Published: June 18, 2024

REFERENCES

1. Ginhoux, F., and Guilliams, M. (2016). Tissue-resident macrophage ontogeny and homeostasis. Immunity *44*, 439–449. https://doi.org/10.1016/j.immuni.2016.02.024.
2. Ribot, J.C., Lopes, N., and Silva-Santos, B. (2021). gammadelta T cells in tissue physiology and surveillance. Nat. Rev. Immunol. *21*, 221–232. https://doi.org/10.1038/s41577-020-00452-4.
3. Buggert, M., Price, D.A., Mackay, L.K., and Betts, M.R. (2023). Human circulating and tissue-resident memory CD8(+) T cells. Nat. Immunol. *24*, 1076–1086. https://doi.org/10.1038/s41590-023-01538-6.
4. Fernandez-Ruiz, D., Ng, W.Y., Holz, L.E., Ma, J.Z., Zaid, A., Wong, Y.C., Lau, L.S., Mollard, V., Cozijnsen, A., Collins, N., et al. (2016). Liver-resident memory CD8(+) T cells form a Front-Line defense against malaria liver-stage. Immunity *45*, 889–902. https://doi.org/10.1016/j.immuni.2016.08.011.

5. Jiang, X., Clark, R.A., Liu, L., Wagers, A.J., Fuhlbrigge, R.C., and Kupper, T.S. (2012). Skin infection generates non-migratory memory CD8+ T(RM) cells providing global skin immunity. Nature *483*, 227–231. https://doi.org/10.1038/nature10851.
6. Mackay, L.K., Stock, A.T., Ma, J.Z., Jones, C.M., Kent, S.J., Mueller, S.N., Heath, W.R., Carbone, F.R., and Gebhardt, T. (2012). Long-lived epithelial immunity by tissue-resident memory T (TRM) cells in the absence of persisting local antigen presentation. Proc. Natl. Acad. Sci. USA *109*, 7037–7042. https://doi.org/10.1073/pnas.1202288109.
7. Reilly, E.C., Lambert Emo, K., Buckley, P.M., Reilly, N.S., Smith, I., Chaves, F.A., Yang, H., Oakes, P.W., and Topham, D.J. (2020). T(RM) integrins CD103 and CD49a differentially support adherence and motility after resolution of influenza virus infection. Proc. Natl. Acad. Sci. USA *117*, 12306–12314. https://doi.org/10.1073/pnas.1915681117.
8. Sheridan, B.S., Pham, Q.M., Lee, Y.T., Cauley, L.S., Puddington, L., and Lefrançois, L. (2014). Oral infection drives a distinct population of intestinal resident memory CD8(+) T cells with enhanced protective function. Immunity *40*, 747–757. https://doi.org/10.1016/j.immuni.2014.03.007.
9. Shin, H., and Iwasaki, A. (2012). A vaccine strategy that protects against genital herpes by establishing local memory T cells. Nature *491*, 463–467. https://doi.org/10.1038/nature11522.
10. Wakim, L.M., Woodward-Davis, A., and Bevan, M.J. (2010). Memory T cells persisting within the brain after local infection show functional adaptations to their tissue of residence. Proc. Natl. Acad. Sci. USA *107*, 17872–17879. https://doi.org/10.1073/pnas.1010201107.
11. Wu, T., Hu, Y., Lee, Y.T., Bouchard, K.R., Benechet, A., Khanna, K., and Cauley, L.S. (2014). Lung-resident memory CD8 T cells (TRM) are indispensable for optimal cross-protection against pulmonary virus infection. J. Leukoc. Biol. *95*, 215–224. https://doi.org/10.1189/jlb.0313180.
12. Connors, T.J., Matsumoto, R., Verma, S., Szabo, P.A., Guyer, R., Gray, J., Wang, Z., Thapa, P., Dogra, P., Poon, M.M.L., et al. (2023). Site-specific development and progressive maturation of human tissue-resident memory T cells over infancy and childhood. Immunity *56*, 1894–1909.e5. https://doi.org/10.1016/j.immuni.2023.06.008.
13. Poon, M.M.L., Caron, D.P., Wang, Z., Wells, S.B., Chen, D., Meng, W., Szabo, P.A., Lam, N., Kubota, M., Matsumoto, R., et al. (2023). Tissue adaptation and clonal segregation of human memory T cells in barrier sites. Nat. Immunol. *24*, 309–319. https://doi.org/10.1038/s41590-022-01395-9.
14. Pallett, L.J., Burton, A.R., Amin, O.E., Rodriguez-Tajes, S., Patel, A.A., Zakeri, N., Jeffery-Smith, A., Swadling, L., Schmidt, N.M., Baiges, A., et al. (2020). Longevity and replenishment of human liver-resident memory T cells and mononuclear phagocytes. J. Exp. Med. *217*, e20200050. https://doi.org/10.1084/jem.20200050.
15. Evrard, M., Becht, E., Fonseca, R., Obers, A., Park, S.L., Ghabdan-Zanluqui, N., Schroeder, J., Christo, S.N., Schienstock, D., Lai, J., et al. (2023). Single-cell protein expression profiling resolves circulating and resident memory T cell diversity across tissues and infection contexts. Immunity *56*, 1664–1680.e9. https://doi.org/10.1016/j.immuni.2023.06.005.
16. Mackay, L.K., Minnich, M., Kragten, N.A.M., Liao, Y., Nota, B., Seillet, C., Zaid, A., Man, K., Preston, S., Freestone, D., et al. (2016). Hobit and Blimp1 instruct a universal transcriptional program of tissue residency in lymphocytes. Science *352*, 459–463. https://doi.org/10.1126/science.aad2035.
17. Milner, J.J., Toma, C., Yu, B., Zhang, K., Omilusik, K., Phan, A.T., Wang, D., Getzler, A.J., Nguyen, T., Crotty, S., et al. (2017). Runx3 programs CD8(+) T cell residency in non-lymphoid tissues and tumours. Nature *552*, 253–257. https://doi.org/10.1038/nature24993.
18. Fonseca, R., Burn, T.N., Gandolfo, L.C., Devi, S., Park, S.L., Obers, A., Evrard, M., Christo, S.N., Buquicchio, F.A., Lareau, C.A., et al. (2022). Runx3 drives a CD8(+) T cell tissue residency program that is absent in CD4(+) T cells. Nat. Immunol. *23*, 1236–1245. https://doi.org/10.1038/s41590-022-01273-4.
19. Zundler, S., Becker, E., Spocinska, M., Slawik, M., Parga-Vidal, L., Stark, R., Wiendl, M., Atreya, R., Rath, T., Leppkes, M., et al. (2019). Hobit- and Blimp-1-driven CD4(+) tissue-resident memory T cells control chronic intestinal inflammation. Nat. Immunol. *20*, 288–300. https://doi.org/10.1038/s41590-018-0298-5.
20. Muñoz-Rojas, A.R., and Mathis, D. (2021). Tissue regulatory T cells: regulatory chameleons. Nat. Rev. Immunol. *21*, 597–611. https://doi.org/10.1038/s41577-021-00519-w.
21. Feuerer, M., Herrero, L., Cipolletta, D., Naaz, A., Wong, J., Nayer, A., Lee, J., Goldfine, A.B., Benoist, C., Shoelson, S., and Mathis, D. (2009). Lean, but not obese, fat is enriched for a unique population of regulatory T cells that affect metabolic parameters. Nat. Med. *15*, 930–939. https://doi.org/10.1038/nm.2002.
22. Xiao, T., Langston, P.K., Muñoz-Rojas, A.R., Jayewickreme, T., Lazar, M.A., Benoist, C., and Mathis, D. (2022). T(regs) in visceral adipose tissue up-regulate circadian-clock expression to promote fitness and enforce a diurnal rhythm of lipolysis. Sci. Immunol. *7*, eabl7641. https://doi.org/10.1126/sciimmunol.abl7641.
23. Burzyn, D., Kuswanto, W., Kolodin, D., Shadrach, J.L., Cerletti, M., Jang, Y., Sefik, E., Tan, T.G., Wagers, A.J., Benoist, C., and Mathis, D. (2013). A special population of regulatory T cells potentiates muscle repair. Cell *155*, 1282–1295. https://doi.org/10.1016/j.cell.2013.10.054.
24. Dombrowski, Y., O'Hagan, T., Dittmer, M., Penalva, R., Mayoral, S.R., Bankhead, P., Fleville, S., Eleftheriadis, G., Zhao, C., Naughton, M., et al. (2017). Regulatory T cells promote myelin regeneration in the central nervous system. Nat. Neurosci. *20*, 674–680. https://doi.org/10.1038/nn.4528.
25. Kalekar, L.A., Cohen, J.N., Prevel, N., Sandoval, P.M., Mathur, A.N., Moreau, J.M., Lowe, M.M., Nosbaum, A., Wolters, P.J., Haemel, A., et al. (2019). Regulatory T cells in skin are uniquely poised to suppress profibrotic immune responses. Sci. Immunol. *4*, eaaw2910. https://doi.org/10.1126/sciimmunol.aaw2910.
26. Ali, N., Zirak, B., Rodriguez, R.S., Pauli, M.L., Truong, H.A., Lai, K., Ahn, R., Corbin, K., Lowe, M.M., Scharschmidt, T.C., et al. (2017). Regulatory T cells in skin facilitate epithelial stem cell differentiation. Cell *169*, 1119–1129.e11. https://doi.org/10.1016/j.cell.2017.05.002.
27. Florez, L.M., Fourcade, G., Darrassse-Jèze, G., Barennes, P., Gan-Fernandez, K., Régnier, P., Nehar-Belaid, D., Courau, T., Ruocco, M.G., Zacchigna, S., et al. (2023). Tissue-resident uterine regulatory T cells support fetal growth. Preprint at bioRxiv. https://doi.org/10.1101/2023.09.07.554921.
28. Beura, L.K., Hamilton, S.E., Bi, K., Schenkel, J.M., Odumade, O.A., Casey, K.A., Thompson, E.A., Fraser, K.A., Rosato, P.C., Filali-Mouhim, A., et al. (2016). Normalizing the environment recapitulates adult human immune traits in laboratory mice. Nature *532*, 512–516. https://doi.org/10.1038/nature17655.
29. Beppu, L.Y., Mooli, R.G.R., Qu, X., Marrero, G.J., Finley, C.A., Fooks, A.N., Mullen, Z.P., Frias, A.B., Jr., Sipula, I., Xie, B., et al. (2021). Tregs facilitate obesity and insulin resistance via a Blimp-1/IL-10 axis. JCI Insight *6*, e140644. https://doi.org/10.1172/jci.insight.140644.
30. Delacher, M., Imbusch, C.D., Hotz-Wagenblatt, A., Mallm, J.P., Bauer, K., Simon, M., Riegel, D., Rendeiro, A.F., Bittner, S., Sanderink, L., et al. (2020). Precursors for nonlymphoid-tissue Treg cells reside in secondary lymphoid organs and are programmed by the transcription factor BATF. Immunity *52*, 295–312.e11. https://doi.org/10.1016/j.immuni.2019.12.002.
31. Fowell, D.J., and Kim, M. (2021). The spatio-temporal control of effector T cell migration. Nat. Rev. Immunol. *21*, 582–596.
32. Varanasi, S.K., Kumar, S.V., and Rouse, B.T. (2020). Determinants of tissue-specific metabolic adaptation of T cells. Cell Metab. *32*, 908–919. https://doi.org/10.1016/j.cmet.2020.10.013.
33. Schuster, H., Shao, W., Weiss, T., Pedrioli, P.G.A., Roth, P., Weller, M., Campbell, D.S., Deutsch, E.W., Moritz, R.L., Planz, O., et al. (2018). A tissue-based draft map of the murine MHC class I immunopeptidome. Sci. Data *5*, 180157. https://doi.org/10.1038/sdata.2018.157.
34. Wroblewska, A., Dhainaut, M., Ben-Zvi, B., Rose, S.A., Park, E.S., Amir, E.D., Bektesevic, A., Baccarini, A., Merad, M., Rahman, A.H., and Brown, B.D. (2018). Protein barcodes enable high-dimensional

single-cell CRISPR screens. Cell *175*, 1141–1155.e16. https://doi.org/10.1016/j.cell.2018.09.022.

35. Dhainaut, M., Rose, S.A., Akturk, G., Wroblewska, A., Nielsen, S.R., Park, E.S., Buckup, M., Roudko, V., Pia, L., Sweeney, R., et al. (2022). Spatial CRISPR genomics identifies regulators of the tumor microenvironment. Cell *185*, 1223–1239.e20. https://doi.org/10.1016/j.cell.2022.02.015.
36. Jordan, M.S., Boesteanu, A., Reed, A.J., Petrone, A.L., Holenbeck, A.E., Lerman, M.A., Naji, A., and Caton, A.J. (2001). Thymic selection of CD4+CD25+ regulatory T cells induced by an agonist self-peptide. Nat. Immunol. *2*, 301–306. https://doi.org/10.1038/86302.
37. Klein, L., Khazaie, K., and von Boehmer, H. (2003). In vivo dynamics of antigen-specific regulatory T cells not predicted from behavior in vitro. Proc. Natl. Acad. Sci. USA *100*, 8886–8891. https://doi.org/10.1073/pnas.1533365100.
38. Liston, A., Lesage, S., Wilson, J., Peltonen, L., and Goodnow, C.C. (2003). Aire regulates negative selection of organ-specific T cells. Nat. Immunol. *4*, 350–354. https://doi.org/10.1038/ni906.
39. Walker, L.S.K., Chodos, A., Eggena, M., Dooms, H., and Abbas, A.K. (2003). Antigen-dependent proliferation of CD4+ CD25+ regulatory T cells in vivo. J. Exp. Med. *198*, 249–258. https://doi.org/10.1084/jem.20030315.
40. Hsieh, C.S., Liang, Y., Tyznik, A.J., Self, S.G., Liggitt, D., and Rudensky, A.Y. (2004). Recognition of the peripheral self by naturally arising CD25+ CD4+ T cell receptors. Immunity *21*, 267–277. https://doi.org/10.1016/j.immuni.2004.07.009.
41. Bautista, J.L., Lio, C.W.J., Lathrop, S.K., Forbush, K., Liang, Y., Luo, J., Rudensky, A.Y., and Hsieh, C.S. (2009). Intraclonal competition limits the fate determination of regulatory T cells in the thymus. Nat. Immunol. *10*, 610–617. https://doi.org/10.1038/ni.1739.
42. Li, C., DiSpirito, J.R., Zemmour, D., Spallanzani, R.G., Kuswanto, W., Benoist, C., and Mathis, D. (2018). TCR transgenic mice reveal stepwise, multi-site acquisition of the distinctive fat-Treg phenotype. Cell *174*, 285–299.e12. https://doi.org/10.1016/j.cell.2018.05.004.
43. Cipolletta, D., Feuerer, M., Li, A., Kamei, N., Lee, J., Shoelson, S.E., Benoist, C., and Mathis, D. (2012). PPAR-gamma is a major driver of the accumulation and phenotype of adipose tissue Treg cells. Nature *486*, 549–553. https://doi.org/10.1038/nature11132.
44. Kolodin, D., van Panhuys, N., Li, C., Magnuson, A.M., Cipolletta, D., Miller, C.M., Wagers, A., Germain, R.N., Benoist, C., and Mathis, D. (2015). Antigen- and cytokine-driven accumulation of regulatory T cells in visceral adipose tissue of lean mice. Cell Metab. *21*, 543–557. https://doi.org/10.1016/j.cmet.2015.03.005.
45. Vasanthakumar, A., Chisanga, D., Blume, J., Gloury, R., Britt, K., Henstridge, D.C., Zhan, Y., Torres, S.V., Liene, S., Collins, N., et al. (2020). Sex-specific adipose tissue imprinting of regulatory T cells. Nature *579*, 581–585. https://doi.org/10.1038/s41586-020-2040-3.
46. Li, C., Muñoz-Rojas, A.R., Wang, G., Mann, A.O., Benoist, C., and Mathis, D. (2021). PPARgamma marks splenic precursors of multiple nonlymphoid-tissue Treg compartments. Proc. Natl. Acad. Sci. USA *118*, e2025197118. https://doi.org/10.1073/pnas.2025197118.
47. Cipolletta, D., Cohen, P., Spiegelman, B.M., Benoist, C., and Mathis, D. (2015). Appearance and disappearance of the mRNA signature characteristic of Treg cells in visceral adipose tissue: age, diet, and PPARgamma effects. Proc. Natl. Acad. Sci. USA *112*, 482–487. https://doi.org/10.1073/pnas.1423486112.
48. Christo, S.N., Evrard, M., Park, S.L., Gandolfo, L.C., Burn, T.N., Fonseca, R., Newman, D.M., Alexandre, Y.O., Collins, N., Zamudio, N.M., et al. (2021). Discrete tissue microenvironments instruct diversity in resident memory T cell function and plasticity. Nat. Immunol. *22*, 1140–1151. https://doi.org/10.1038/s41590-021-01004-1.
49. Delacher, M., Imbusch, C.D., Weichenhan, D., Breiling, A., Hotz-Wagenblatt, A., Träger, U., Hofer, A.C., Kägebein, D., Wang, Q., Frauhammer, F., et al. (2017). Genome-wide DNA-methylation landscape defines specialization of regulatory T cells in tissues. Nat. Immunol. *18*, 1160–1172. https://doi.org/10.1038/ni.3799.
50. Spath, S., Roan, F., Presnell, S.R., Höllbacher, B., and Ziegler, S.F. (2022). Profiling of Tregs across tissues reveals plasticity in ST2 expression and hierarchies in tissue-specific phenotypes. iScience *25*, 104998. https://doi.org/10.1016/j.isci.2022.104998.
51. Hayatsu, N., Miyao, T., Tachibana, M., Murakami, R., Kimura, A., Kato, T., Kawakami, E., Endo, T.A., Setoguchi, R., Watarai, H., et al. (2017). Analyses of a mutant Foxp3 allele reveal BATF as a critical transcription factor in the differentiation and accumulation of tissue regulatory T cells. Immunity *47*, 268–283.e9. https://doi.org/10.1016/j.immuni.2017.07.008.
52. Ito, M., Komai, K., Mise-Omata, S., Iizuka-Koga, M., Noguchi, Y., Kondo, T., Sakai, R., Matsuo, K., Nakayama, T., Yoshie, O., et al. (2019). Brain regulatory T cells suppress astrogliosis and potentiate neurological recovery. Nature *565*, 246–250. https://doi.org/10.1038/s41586-018-0824-5.
53. Kaiser, K.A., Loffredo, L.F., Santos-Alexis, K.L., Ringham, O.R., and Arpaia, N. (2023). Regulation of the alveolar regenerative niche by amphiregulin-producing regulatory T cells. J. Exp. Med. *220*, e20221462. https://doi.org/10.1084/jem.20221462.
54. Arpaia, N., Green, J.A., Moltedo, B., Arvey, A., Hemmers, S., Yuan, S., Treuting, P.M., and Rudensky, A.Y. (2015). A distinct function of regulatory T cells in tissue protection. Cell *162*, 1078–1089. https://doi.org/10.1016/j.cell.2015.08.021.
55. Liu, J., Pan, L., Hong, W., Chen, S., Bai, P., Luo, W., Sun, X., He, F., Jia, X., Cai, J., et al. (2022). GPR174 knockdown enhances blood flow recovery in hindlimb ischemia mice model by upregulating AREG expression. Nat. Commun. *13*, 7519. https://doi.org/10.1038/s41467-022-35159-8.
56. Melderis, S., Warkotsch, M.T., Dang, J., Hagenstein, J., Ehnold, L.I., Herrnstadt, G.R., Niehus, C.B., Feindt, F.C., Kylies, D., Puelles, V.G., et al. (2022). The amphiregulin/EGFR axis protects from lupus nephritis via downregulation of pathogenic CD4(+) T helper cell responses. J. Autoimmun. *129*, 102829. https://doi.org/10.1016/j.jaut.2022.102829.
57. Dai, K., Huang, L., Chen, J., Yang, L., and Gong, Z. (2015). Amphiregulin promotes the immunosuppressive activity of intrahepatic CD4(+) regulatory T cells to impair CD8(+) T-cell immunity against hepatitis B virus infection. Immunology *144*, 506–517. https://doi.org/10.1111/imm.12400.
58. Yan, D., Yu, F., Chen, L., Yao, Q., Yan, C., Zhang, S., Wu, N., Gong, D., Sun, H., Fu, Y., et al. (2020). Subconjunctival injection of regulatory T cells potentiates corneal healing via orchestrating inflammation and tissue repair after acute alkali Burn. Invest. Ophthalmol. Vis. Sci. *61*, 22. https://doi.org/10.1167/iovs.61.14.22.
59. Kuswanto, W., Burzyn, D., Panduro, M., Wang, K.K., Jang, Y.C., Wagers, A.J., Benoist, C., and Mathis, D. (2016). Poor repair of skeletal muscle in aging mice reflects a defect in local, interleukin-33-dependent accumulation of regulatory T cells. Immunity *44*, 355–367. https://doi.org/10.1016/j.immuni.2016.01.009.
60. Wang, K., Yaghi, O.K., Spallanzani, R.G., Chen, X., Zemmour, D., Lai, N., Chiu, I.M., Benoist, C., and Mathis, D. (2020). Neuronal, stromal, and T-regulatory cell crosstalk in murine skeletal muscle. Proc. Natl. Acad. Sci. USA *117*, 5402–5408. https://doi.org/10.1073/pnas.1922559117.
61. Xia, N., Lu, Y., Gu, M., Li, N., Liu, M., Jiao, J., Zhu, Z., Li, J., Li, D., Tang, T., et al. (2020). A unique population of regulatory T cells in heart potentiates cardiac protection from myocardial infarction. Circulation *142*, 1956–1973. https://doi.org/10.1161/CIRCULATIONAHA.120.046789.
62. Sakai, R., Ito, M., Komai, K., Iizuka-Koga, M., Matsuo, K., Nakayama, T., Yoshie, O., Amano, K., Nishimasu, H., Nureki, O., et al. (2021). Kidney GATA3(+) regulatory T cells play roles in the convalescence stage after antibody-mediated renal injury. Cell. Mol. Immunol. *18*, 1249–1261. https://doi.org/10.1038/s41423-020-00547-x.
63. Panduro, M., Benoist, C., and Mathis, D. (2016). Tissue Tregs. Annu. Rev. Immunol. *34*, 609–633. https://doi.org/10.1146/annurev-immunol-032712-095948.
64. Kohlgruber, A.C., Gal-Oz, S.T., LaMarche, N.M., Shimazaki, M., Duquette, D., Koay, H.F., Nguyen, H.N., Mina, A.I., Paras, T., Tavakkoli, A., et al. (2018). gammadelta T cells producing interleukin-17A regulate adipose regulatory T cell homeostasis and thermogenesis. Nat. Immunol. *19*, 464–474. https://doi.org/10.1038/s41590-018-0094-2.

Please cite this article in press as: Burton et al., The tissue-resident regulatory T cell pool is shaped by transient multi-tissue migration and a conserved residency program, Immunity (2024), https://doi.org/10.1016/j.immuni.2024.05.023

65. Cho, J., Kuswanto, W., Benoist, C., and Mathis, D. (2019). T cell receptor specificity drives accumulation of a reparative population of regulatory T cells within acutely injured skeletal muscle. Proc. Natl. Acad. Sci. USA *116*, 26727–26733. https://doi.org/10.1073/pnas.1914848116.

66. Dunn, O.J. (1964). Multiple Comparisons Using Rank Sums. Technometrics *6*, 241–252.

67. Liston, A., Nutsch, K.M., Farr, A.G., Lund, J.M., Rasmussen, J.P., Koni, P.A., and Rudensky, A.Y. (2008). Differentiation of regulatory Foxp3+ T cells in the thymic cortex. Proc. Natl. Acad. Sci. USA *105*, 11903–11908. https://doi.org/10.1073/pnas.0801506105.

68. Herndler-Brandstetter, D., Ishigame, H., Shinnakasu, R., Plajer, V., Stecher, C., Zhao, J., Lietzenmayer, M., Kroehling, L., Takumi, A., Kometani, K., et al. (2018). KLRG1(+) effector CD8(+) T cells lose KLRG1, differentiate into all memory T cell lineages, and convey enhanced protective immunity. Immunity *48*, 716–729.e8. https://doi.org/10.1016/j.immuni.2018.03.015.

69. Notario, L., Alari-Pahissa, E., de Molina, A., and Lauzurica, P. (2016). CD69 deficiency enhances the Host Response to Vaccinia Virus Infection through Altered NK Cell Homeostasis. J. Virol. *90*, 6464–6474. https://doi.org/10.1128/JVI.00550-16.

70. Mombaerts, P., Iacomini, J., Johnson, R.S., Herrup, K., Tonegawa, S., and Papaioannou, V.E. (1992). RAG-1-deficient mice have no mature B and T lymphocytes. Cell *68*, 869–877. https://doi.org/10.1016/0092-8674(92)90030-g.

71. Ding, Z.M., Babensee, J.E., Simon, S.I., Lu, H., Perrard, J.L., Bullard, D.C., Dai, X.Y., Bromley, S.K., Dustin, M.L., Entman, M.L., et al. (1999). Relative contribution of LFA-1 and Mac-1 to neutrophil adhesion and migration. J. Immunol. *163*, 5029–5038.

72. Ryan, H.E., Poloni, M., McNulty, W., Elson, D., Gassmann, M., Arbeit, J.M., and Johnson, R.S. (2000). Hypoxia-inducible factor-1alpha is a positive factor in solid tumor growth. Cancer Res. *60*, 4010–4015.

73. Schaefer, B.C., Schaefer, M.L., Kappler, J.W., Marrack, P., and Kedl, R.M. (2001). Observation of antigen-dependent CD8+ T-cell/ dendritic cell interactions in vivo. Cell. Immunol. *214*, 110–122. https://doi.org/10.1006/cimm.2001.1895.

74. Tata, A., Dodard, G., Fugère, C., Leget, C., Ors, M., Rossi, B., Vivier, E., and Brossay, L. (2021). Combination blockade of KLRG1 and PD-1 promotes immune control of local and disseminated cancers. Oncoimmunology *10*, 1933808. https://doi.org/10.1080/2162402X.2021.1933808.

75. Shapiro-Shelef, M., Lin, K.I., McHeyzer-Williams, L.J., Liao, J., McHeyzer-Williams, M.G., and Calame, K. (2003). Blimp-1 is required for the formation of immunoglobulin secreting plasma cells and pre-plasma memory B cells. Immunity *19*, 607–620. https://doi.org/10.1016/s1074-7613(03)00267-x.

76. Townsend, M.J., Fallon, P.G., Matthews, D.J., Jolin, H.E., and McKenzie, A.N. (2000). T1/ST2-deficient mice demonstrate the importance of T1/ST2 in developing primary T helper cell type 2 responses. J. Exp. Med. *191*, 1069–1076. https://doi.org/10.1084/jem.191.6.1069.

77. Rubtsov, Y.P., Niec, R.E., Josefowicz, S., Li, L., Darce, J., Mathis, D., Benoist, C., and Rudensky, A.Y. (2010). Stability of the regulatory T cell lineage in vivo. Science *329*, 1667–1671. https://doi.org/10.1126/science.1191996.

78. Junius, S., Mavrogiannis, A.V., Lemaitre, P., Gerbaux, M., Staels, F., Malviya, V., Burton, O., Gergelits, V., Singh, K., Tito Tadeo, R.Y., et al. (2021). Unstable regulatory T cells, enriched for naive and Nrp1(neg) cells, are purged after fate challenge. Sci. Immunol. *6*, eabe4723. https://doi.org/10.1126/sciimmunol.abe4723.

79. Kamran, P., Sereti, K.I., Zhao, P., Ali, S.R., Weissman, I.L., and Ardehali, R. (2013). Parabiosis in mice: a detailed protocol. J. Vis. Exp. https://doi.org/10.3791/50556.

80. Whyte, C.E., Tumes, D.J., Liston, A., and Burton, O.T. (2022). Do more with less: improving high parameter cytometry through overnight staining. Curr. Protoc. *2*, e589. https://doi.org/10.1002/cpz1.589.

81. Holst, J., Szymczak-Workman, A.L., Vignali, K.M., Burton, A.R., Workman, C.J., and Vignali, D.A.A. (2006). Generation of T-cell receptor retrogenic mice. Nat. Protoc. *1*, 406–417. https://doi.org/10.1038/nprot.2006.61.

82. Andrews, S. (2010). FastQC: A quality control tool for high throughput sequence data. GitHub. https://github.com/s-andrews/FastQC.

83. Krueger, F. (2012). Trim galore! Consistent quality and adapter trimming for RRBS or standard FastQ files. GitHub. https://github.com/FelixKrueger/TrimGalore.

84. Dobin, A., Davis, C.A., Schlesinger, F., Drenkow, J., Zaleski, C., Jha, S., Batut, P., Chaisson, M., and Gingeras, T.R. (2013). STAR: ultrafast universal RNA-seq aligner. Bioinformatics *29*, 15–21. https://doi.org/10.1093/bioinformatics/bts635.

85. Frankish, A., Diekhans, M., Ferreira, A.M., Johnson, R., Jungreis, I., Loveland, J., Mudge, J.M., Sisu, C., Wright, J., Armstrong, J., et al. (2019). GENCODE reference annotation for the human and mouse genomes. Nucleic Acids Res. *47*, D766–D773. https://doi.org/10.1093/nar/gky955.

86. Liao, Y., Smyth, G.K., and Shi, W. (2014). featureCounts: an efficient general purpose program for assigning sequence reads to genomic features. Bioinformatics *30*, 923–930. https://doi.org/10.1093/bioinformatics/btt656.

87. Ewels, P., Magnusson, M., Lundin, S., and Käller, M. (2016). MultiQC: summarize analysis results for multiple tools and samples in a single report. Bioinformatics *32*, 3047–3048. https://doi.org/10.1093/bioinformatics/btw354.

88. Love, M.I., Huber, W., and Anders, S. (2014). Moderated estimation of fold change and dispersion for RNA-seq data with DESeq2. Genome Biol. *15*, 550. https://doi.org/10.1186/s13059-014-0550-8.

89. van der Maaten, L., and Hinton, G. (2008). Visualizing high-dimensional data using t-SNE. J. Mach. Learn. Res. *9*, 2579–2605.

90. Krijthe, J.H. (2015). Rtsne: T-distributed stochastic neighbor embedding using Barnes-Hut implementation. GitHub. https://github.com/jkrijthe/Rtsne.

91. McInnes, L., Healy, J., Saul, N., and Großberger, L. (2018). UMAP: uniform manifold approximation and projection. J. Open Source Software *3*, 861.

92. Konopka, T. (2020). Umap: Uniform Manifold Approximation and Projection. CRAN. https://CRAN.R-project.org/package=umap.

93. Luo, W., Friedman, M.S., Shedden, K., Hankenson, K.D., and Woolf, P.J. (2009). GAGE: generally applicable gene set enrichment for pathway analysis. BMC Bioinformatics *10*, 161. https://doi.org/10.1186/1471-2105-10-161.

94. Luo, W., and Brouwer, C. (2013). Pathview: an R/Bioconductor package for pathway-based data integration and visualization. Bioinformatics *29*, 1830–1831. https://doi.org/10.1093/bioinformatics/btt285.

95. Yu, G., Wang, L.G., Han, Y., and He, Q.Y. (2012). clusterProfiler: an R package for comparing biological themes among gene clusters. Omics *16*, 284–287. https://doi.org/10.1089/omi.2011.0118.

96. Chang, W., Cheng, J., Allaire, J.J., Xie, Y., and McPherson, J. (2020). Shiny: web Application Framework for R. CRAN. https://CRAN.R-project.org/package=shiny.

97. Roca, C.P., Burton, O.T., Gergelits, V., Prezzemolo, T., Whyte, C.E., Halpert, R., Kreft, Ł., Collier, J., Botzki, A., Spidlen, J., et al. (2021). AutoSpill is a principled framework that simplifies the analysis of multichromatic flow cytometry data. Nat. Commun. *12*, 2890. https://doi.org/10.1038/s41467-021-23126-8.

98. Roca, C.P., Burton, O.T., Neumann, J., Tareen, S., Whyte, C.E., Gergelits, V., Veiga, R.V., Humblet-Baron, S., and Liston, A. (2023). A cross entropy test allows quantitative statistical comparison of t-SNE and UMAP representations. Cell Rep. Methods *3*, 100390. https://doi.org/10.1016/j.crmeth.2022.100390.

99. Gergelits, V., Burton, O., Dooley, J., and Liston, A. (2024). Markov chain models for tissue regulatory T cell cellular kinetics and dwell times V1. Mendeley Data. https://doi.org/10.17632/czhfj4g6vb.1.

Please cite this article in press as: Burton et al., The tissue-resident regulatory T cell pool is shaped by transient multi-tissue migration and a conserved residency program, Immunity (2024), https://doi.org/10.1016/j.immuni.2024.05.023

STAR★METHODS

KEY RESOURCES TABLE

REAGENT or RESOURCE	SOURCE	IDENTIFIER
Antibodies		
Alexa Fluor 405 anti-CD11c	Biotechne	Cat# FAB69501V-100UG
Alexa Fluor 488 anti-CD45.1	BioLegend	Cat# 110718; RRID:AB_492862
Alexa Fluor 594 anti-T-bet	BioLegend	Cat# 644833; RRID:AB_2728473
Alexa Fluor 647 anti-CD193	BioLegend	Cat# 144508; RRID:AB_2561536
Alexa Fluor 660 anti-Foxp3	ThermoFisher	Cat# 606-5773-80; RRID:AB_2896287
Alexa Fluor 700 anti-Ki67	ThermoFisher	Cat# 56-5698-82; RRID:AB_2637480
Alexa Fluor 700 anti-TIGIT	Biotechne	Cat# FAB72671N-100UG
APC anti-CD90.1	ThermoFisher	Cat# 17-0900-82; RRID:AB_469420
APC anti-Foxp3	Miltenyi	Cat# 130-111-601; RRID:AB_2651768
APC anti-Foxp3	ThermoFisher	Cat# 17-5773-82; RRID:AB_469457
APC/Fire 750 anti-Integrin β7	BioLegend	Cat# 321224; RRID:AB_2715981
BB515 anti-CD199	BD Biosciences	Cat# 565577; RRID:AB_2869688)
BB660-P2 anti-CD95	BD Biosciences	custom
BB700 anti-LAG3	BD Biosciences	Cat# 742206; RRID:AB_2740664
BB755-P anti-CD8a	BD Biosciences	custom
BB790-P anti-Ly-6C	BD Biosciences	custom
Biotin anti-CD45	ThermoFisher	Cat# 13-0451-85; RRID:AB_466447
BUV395 anti-CD103	BD Biosciences	Cat# 740238; RRID:AB_2739985
BUV395 anti-CD45	BD Biosciences	Cat# 564279; RRID:AB_2651134
BUV496 anti-CD4	BD Biosciences	Cat# 612952; RRID:AB_2813886
BUV563 anti-CD45	BD Biosciences	Cat# 612924; RRID:AB_2870209
BUV563 anti-NK1.1	BD Biosciences	Cat# 741233; RRID:AB_2870785
BUV615 anti-CD152	BD Biosciences	custom
BUV615 anti-Siglec F	BD Biosciences	custom
BUV661 anti-CD103	BD Biosciences	Cat# 750718; RRID:AB_2874838
BUV661 anti-CD19	BD Biosciences	Cat# 612971; RRID:AB_2870243
BUV737 anti-CD62L	BD Biosciences	Cat# 612833; RRID:AB_2870155
BUV805 anti-CD8a	BD Biosciences	Cat# 612898; RRID:AB_2870186
BUV805 anti-GITR	BD Biosciences	Cat# 742061; RRID:AB_2871349
BV421 anti-CD103	BioLegend	Cat# 121422; RRID:AB_2562901
BV421 anti-CD11c	BioLegend	Cat# 117330; RRID:AB_11219593
BV421 anti-CD152	BioLegend	Cat# 106312; RRID:AB_2563063
BV421 anti-CD45.1	BioLegend	Cat# 110732; RRID:AB_2562563
BV421 anti-ICOS	BioLegend	Cat# 313524; RRID:AB_2562545
BV480 anti-CD192	BD Biosciences	Cat# 747971; RRID:AB_2872432
BV480 anti-CD25	BD Biosciences	Cat# 566120; RRID:AB_2739522
BV510 anti-CD44	BioLegend	Cat# 103044; RRID:AB_2650923
BV570 anti-CD44	BioLegend	Cat# 103037; RRID:AB_10900641
BV570 anti-CD90.2	BioLegend	Cat# 105329; RRID:AB_10917055
BV605 anti-ICOS	BioLegend	Cat# 313538; RRID:AB_2687079
BV650 anti-CD3	BioLegend	Cat# 100229; RRID:AB_11204249
BV650 anti-RORγT	BD Biosciences	Cat# 564722; RRID:AB_2738915
BV650 anti-XCR1	BioLegend	Cat# 148220; RRID:AB_2566410
BV711 anti-PD-1	BioLegend	Cat# 135231; RRID:AB_2566158

(*Continued on next page*)

Please cite this article in press as: Burton et al., The tissue-resident regulatory T cell pool is shaped by transient multi-tissue migration and a conserved residency program, Immunity (2024), https://doi.org/10.1016/j.immuni.2024.05.023

CellPress
OPEN ACCESS

Continued

REAGENT or RESOURCE	SOURCE	IDENTIFIER
BV750 anti-CD183	BD Biosciences	Cat# 747298; RRID:AB_2872012
BV750 anti-CD19	BD Biosciences	Cat# 747332; RRID:AB_2872036
BV785 anti-KLRG1	BioLegend	Cat# 138429; RRID:AB_2629749
eFluor 450 anti-Helios	ThermoFisher	Cat# 48-9883-41; RRID:AB_2574137
eFluor 450 anti-TIM-3	ThermoFisher	Cat# 48-5871-82; RRID:AB_2574081
eFluor 660 anti-IRF4	ThermoFisher	Cat# 50-9858-82; RRID:AB_2574393
FITC anti-TCRγδ	ThermoFisher	Cat# 11-5711-82; RRID:AB_465238
Pacific Blue anti-Helios	BioLegend	Cat# 137220; RRID:AB_10690535
Pacific Orange anti-F4/80	ThermoFisher	Cat# MF48030; RRID:AB_2539704
PE anti-CD120b	BioLegend	Cat# 113406; RRID:AB_2206941
PE anti-Nur77	ThermoFisher	Cat# 12-5965-82; RRID:AB_1257209
PE anti-T-bet	Miltenyi	Cat# 130-098-596; RRID:AB_2653647
PE-Cy5 anti-CD69	BioLegend	Cat# 104510; RRID:AB_313113
PE-Cy5.5 anti-CD25	ThermoFisher	Cat# 35-0251-82; RRID:AB_11218898
PE-Cy7 anti-ST2	ThermoFisher	Cat# 25-9335-80; RRID:AB_2637463
PE-Dazzle 594 anti-CD196	BioLegend	Cat# 129822; RRID:AB_2687019
PE-eFluor610 anti-GATA-3	ThermoFisher	Cat# 61-9966-41; RRID:AB_2574685
PerCP anti-I-A/I-E	Biolegend	Cat# 107624; RRID:AB_2191073
PerCP-eFluor710 anti-CD304	ThermoFisher	Cat# 46-3041-82; RRID:AB_2573741
PE-Vio615 anti-Helios	Miltenyi	Cat# 130-112-636; RRID:AB_2651984
Purified anti-CD11b	ThermoFisher	Cat# 14-0112-82; RRID:AB_467108
Purified anti-CD24	BioLegend	Cat# 14-0242-82; RRID:AB_467170
Purified anti-Ly-6G	BioLegend	Cat# 127602; RRID:AB_1089180
Purified anti-NK1.1	BioLegend	Cat# 108702; RRID:AB_313389
SBV515 anti-CD25	BioRad	Cat# MCA1260SBV515
SBV610 anti-NK1.1	BioRad	Cat# MCA1266SBV610
Spark Blue 550 anti-CD3	BioLegend	Cat# 100260; RRID:AB_2832258
Spark Blue 550 anti-CD45.2	BioLegend	Cat# 109862; RRID:AB_2860626
StarBright UV400 anti-F4/80	BioRad	custom
StarBright UV445 anti-CD45R	BioRad	custom
StarBright Violet440 anti-CD3	BioRad	Cat# MCA500SBV440
StarBright Violet515 anti-CD25	BioRad	Cat# MCA1260SBV515
StarBright Violet610 anti-CD161	BioRad	Cat# MCA1266SBV610
Super Bright 780 anti-KLRG1	ThermoFisher	Cat# 78-5893-80; RRID:AB_2735064
Alexa Fluor 350 anti-S tag	ThermoFisher	Cat# MA1-981; RRID:AB_347008
BV421 anti-HA tag	BioLegend	Cat# 682405; RRID:AB_2716037
CF405M anti-Ollas tag	ThermoFisher	Cat# MA5-16125; RRID:AB_11152481
Alexa Fluor 532 anti-AU1 tag	BioLegend	Cat# 901902; RRID:AB_2565014
PE-Cy7 anti-V5 tag	ThermoFisher	Cat# 25-6796-42; RRID:AB_2784669
Alexa Fluor 647 anti-NWS tag	BioLegend	Cat# 688202; RRID:AB_2629594
DyLight 800 anti-Flag tag	ThermoFisher	Cat# MA1-91878-D680; RRID:AB_2537624
TotalSeq™-C0301 anti-mouse Hashtag 1 Antibody	BioLegend	Cat# 155861; RRID:AB_2800693
TotalSeq™-C0302 anti-mouse Hashtag 2 Antibody	BioLegend	Cat# 155863; RRID:AB_2800694
TotalSeq™-C0303 anti-mouse Hashtag 3 Antibody	BioLegend	Cat# 155865; RRID:AB_2800695
TotalSeq™-C0304 anti-mouse Hashtag 4 Antibody	BioLegend	Cat# 155867; RRID:AB_2800696
TotalSeq™-C0305 anti-mouse Hashtag 5 Antibody	BioLegend	Cat# 155869; RRID:AB_2800697
TotalSeq™-C0197 anti-mouse CD69 Antibody	BioLegend	Cat# 104551; RRID:AB_2832333
Chemicals, peptides, and recombinant proteins		
ViaKrome 808	Beckman Coulter	Cat# C36628

(*Continued on next page*)

Continued

REAGENT or RESOURCE	SOURCE	IDENTIFIER
Alexa Fluor 350 conjugation kit	ThermoFisher	Cat# A20180
Fixable Viability Dye eFluor780	ThermoFisher	Cat# 65-0865-18
PE-Cy5.5 conjugation kit	Abcam	Cat# ab102899
StarBright Violet670 Streptavidin	BioRad	Cat# STAR210SBV670
Alexa Fluor 790 conjugation kit	ThermoFisher	Cat# A20189
Qdot545 Streptavidin	ThermoFisher	Cat# Q10091MP
Alexa Fluor 532 conjugation kit	ThermoFisher	Cat# A20182
APC-Cy5.5 conjugation kit	Abcam	Cat# ab102855
Mix-n-Stain™ CF®405M Antibody Labeling Kit	Biotium	Cat# BT92232
Alexa Fluor 647 NHS Ester	ThermoFisher	Cat# A20006
Cas9 protein	IDT	Cat# 1081058
EasySep Mouse Hematopoietic Progenitor Cell Isolation kit	Stem Cell Technologies	Cat# 19856
TPO	R&D Systems	Cat# 488-TO-025/CF
IL-3	BioLegend	Cat# 575506
IL-6	BioLegend	Cat# 575706
SCF	BioLegend	Cat# 579708
FLT3L	BioLegend	Cat# 550706
Baytril	Sigma-Aldrich	Cat# 17849
StemSpan SFEM II medium	Stem Cell Technologies	Cat# 9605
EDTA	ThermoFisher	Cat# 15575020
Percoll	Sigma-Aldrich	Cat# GE17-0891-01
IMDM	ThermoFisher	Cat# 12440053
HEPES	ThermoFisher	Cat# 15630056
Sodium pyruvate	ThermoFisher	Cat# 11360070
Gentamicin	Abcam	Cat# ab146573
Calcium chloride	Sigma-Aldrich	Cat# C1016-100G
Magnesium chloride	Sigma-Aldrich	Cat# 208337-100G
Collagenase D	Sigma-Aldrich	Cat# COLLD-RO
Collagenase IV	ThermoFisher	Cat# 17104019
DNase I	Sigma-Aldrich	Cat# DN25
Nitex	Sefar	https://www.sefar.com/
2.4G2 hybridoma	produced in house	https://pubmed.ncbi.nlm.nih.gov/2434334/
Foxp3/Transcription Factor Staining Buffer Set	ThermoFisher	Cat# 00-5523-00
Neutral buffered formalin	VWR	Cat# 9713.5000
Precision Count beads	BioLegend	Cat# 424902
50kDa centrifugal filters	Sigma Aldrich	Cat# UFC505096
NEBulder Hifi DNA assembly	NEB	Cat# E2621L
NcoI	NEB	Cat# R0193S
NotI	NEB	Cat# R0189S
Rneasy Mini Kit	Qiagen	Cat# 74106
Critical commercial assays		
Chromium Next GEM Single Cell 5' Reagent Kits v2	10X Genomics	Cat# PN-1000265
Library Construction Kit	10X Genomics	Cat# PN-1000190
5' Feature Barcode Kit	10X Genomics	Cat# PN-1000256
Chromium Single Cell Mouse TCR Amplification Kit	10X Genomics	Cat# PN-1000254
Chromium Next GEM Chip K Single Cell Kit	10X Genomics	Cat# PN-1000287
Dual Index Kit TT Set A	10X Genomics	Cat# PN-1000215

(*Continued on next page*)

Please cite this article in press as: Burton et al., The tissue-resident regulatory T cell pool is shaped by transient multi-tissue migration and a conserved residency program, Immunity (2024), https://doi.org/10.1016/j.immuni.2024.05.023

CellPress
OPEN ACCESS

Continued

REAGENT or RESOURCE	SOURCE	IDENTIFIER
Deposited data		
Tissue screen	This paper, Figures 1A–1G	Flow Repository: FR-FCM-Z6ME
Nur77	This paper, Figures 1H and 1I	Flow Repository: FR-FCM-Z6L8
Ageing	This paper, Figures 2A–2D	Flow Repository: FR-FCM-Z6L9
Microbiome	This paper, Figures 2E–2I	Flow Repository: FR-FCM-Z6LT
CD69 KO chimera	This paper, Figure 4	Flow Repository: FR-FCM-Z6MF
ST2 KO chimera	This paper, Figure 4	Flow Repository: FR-FCM-Z6MK
CD11a KO chimera	This paper, Figure 4	Flow Repository: FR-FCM-Z6ML
KLRG1 KO chimera	This paper, Figure 4	Flow Repository: FR-FCM-Z6MJ
CD4Cre Blimp1$^{fl/fl}$ chimera	This paper, Figure 4	Flow Repository: FR-FCM-Z6MW
S1PR2 chimera	This paper, Figure 4	Flow Repository: FR-FCM-Z6MH
BATF KO chimera	This paper, Figure 4	Flow Repository: FR-FCM-Z6MM
CD4Cre Hif1a$^{fl/fl}$ chimera	This paper, Figure 4	Flow Repository: FR-FCM-Z6MN
Areg KO	This paper, Figure 4	Flow Repository: FR-FCM-Z6MS
CD103 KO	This paper, Figure 4	Flow Repository: FR-FCM-Z6MR
Parabiosis	This paper, Figure 5	Flow Repository: FR-FCM-Z5UV
Female:male parabiosis	This paper, Figures 7A–7C	Flow Repository: FR-FCM-Z6MQ
Foxp3^{ERT2Cre} CD69$^{fl/fl}$	This paper, Data S1	Flow Repository: FR-FCM-Z6MG
i.v. CD45 labeling	This paper, Figure S2	Flow Repository: FR-FCM-Z6MX
Klrg1Cre RosaAi14 fate mapper	This paper, Data S1	Flow Repository: FR-FCM-Z6MP
Tissue Treg bulk RNA-Seq	This paper, Figure 3	GEO: GSE265835
Tissue Treg TCR scRNA-Seq	This paper, Figure 6	GEO: GSE266111
Experimental models: Organisms/strains		
Mouse: Foxp3Thy1.1 reporter: C57BL/6.129(Cg)-Foxp3$^{tm5(Thy1.1)Ayr}$/J.SJL-Ptprc^{a}.Pepc^{b}/BoyJ; C57BL/6.129(Cg)-Foxp3$^{tm5(Thy1.1)Ayr}$/J	Alexander Rudensky (Sloan Kettering)	https://www.pnas.org/doi/10.1073/pnas.0801506105
Mouse: OT-II TCR transgenic: C57BL/6.SJL-Ptprc^{a}/BoyJ; C57BL/6.Rag2^{tm1Fwa}.SJL-Ptprc^{a}/BoyJ	Michelle Linterman and Rahul Roychoudhuri (Babraham Institute)	Stock No: 004194
Mouse: C57BL/6 germfree	Germfree Ghent Germfree and Gnotobiotic mouse facility	Stock No: 000664
Mouse: C57BL/6J	Jackson	Stock No: 000664
Mouse: Rag knockout: B6(Cg)-Rag2$^{tm1.1Cgn}$/J	Jackson	Stock No: 008449
Mouse: CD45.1 mice: B6.SJL-Ptprc^{a} Pepc^{b}/BoyJ	Jackson	Stock No: 002014
Mouse: Klrg1Cre RosaAi14: C57BL/6Jax-Klrg1$^{tm1(IRES-eGFP-iCre)Fla}$	Takaharu Okada (RIKEN)	https://www.sciencedirect.com/science/article/pii/S1074761318300918
Mouse: CD69$^{-/-}$	Pilar Lauzurica (Carlos III, Madrid)	https://www.ncbi.nlm.nih.gov/pmc/articles/PMC4936124/
Mouse: CD11a$^{-/-}$: Itgal^{tm1Bll}	Andrew McKenzie (LMB)	https://pubmed.ncbi.nlm.nih.gov/10528208/
Mouse: Mouse: CD4Cre Hif1a$^{fl/fl}$: B6.129-Tg(Cd4-cre)^{1Cwi}.Hif1^{atm3Rsjo}/J.Foxp3$^{tm5(Thy1.1)Ayr}$/J	Alex Gould (Francis Crick Institute)	https://pubmed.ncbi.nlm.nih.gov/10945599/
Mouse: Ubiquitin-GFP: (UbiquitinC)Tg(UBC-GFP)^{30Scha}/J Ptprca	Michelle Linterman (Babraham Institute)	https://pubmed.ncbi.nlm.nih.gov/12088410/
Mouse: Klrg1$^{-/-}$: C57BL/6-Klrg1^{em1Lbro}/J	Laurent Brossay (Brown University)	https://pubmed.ncbi.nlm.nih.gov/34188973/
Mouse: S1pr2$^{-/-}$: S1pr2$^{tm2a(EUCOMM)Hmgu}$	Michelle Linterman (Babraham Institute)	https://www.informatics.jax.org/allele/MGI:5306490
Mouse: CD4Cre Blimp1fl/fl: B6.129-Prdm1^{tm1Clme}/J- Tg(Cd4-cre)1Cwi	Michelle Linterman (Babraham Institute)	https://pubmed.ncbi.nlm.nih.gov/14563324/

(*Continued on next page*)

Continued

REAGENT or RESOURCE	SOURCE	IDENTIFIER
Mouse: ST2$^{-/-}$: Il1rl1^{tm1Anjm}	Andrew McKenzie (LMB)	https://pubmed.ncbi.nlm.nih.gov/10727469/
Mouse: BATF$^{-/-}$: B6.129S-Batf$^{tm1.1Kmm}$/J	Jackson	Stock No: 013758
Mouse: CD69$^{fl/fl}$: C57BL/6.CD69$^{tm1(flox)ALi}$/J	Cyagen	This paper
Mouse: CD103-/-: C57BL/6.Itgae^{tm1SSc}	VIB-KU Leuven	This paper
Mouse: Areg$^{-/-}$: C57BL/6.Areg^{tm1SSc}	VIB-KU Leuven	This paper
Mouse: Foxp3ERT2Cre: Foxp3$^{tm9(EGFP/cre/ERT2)Ayr}$	Alexander Rudensky (Sloan Kettering)	https://www.ncbi.nlm.nih.gov/pmc/articles/PMC4262151/
Mouse: RosaRFP mice: C57BL/6.129-Gt(ROSA)26Sor$^{tm2(RFP)}$	Joerg Fehling (Ulm)	https://pubmed.ncbi.nlm.nih.gov/17171761/
Mouse: CD4Cre (B6.Cg-Tg(Cd4-cre)$^{1Cwi/BfluJ}$)	Jackson	Stock No: 022071
Oligonucleotides		
GTTGAGGCTGCGGAACTTCC	IDT	N/A
ATAATATAGCCGGATATTTGTGG	IDT	N/A
GTTGAGGCTGCGGAACTTCC	IDT	N/A
Recombinant DNA		
TCR OTII-2A.pMIG II	Addgene	Cat# 52112
For FlowCode plasmids, see Data S2.	This paper	Data S2
Software and algorithms		
FastQC	Babraham Bioinformatics	https://www.bioinformatics.babraham.ac.uk/projects/fastqc/
Trim Galore!	GitHub	https://www.bioinformatics.babraham.ac.uk/projects/trim_galore/
STAR aligner	GitHub	https://www.ncbi.nlm.nih.gov/pmc/articles/PMC3530905/
MultiQC	GitHub	https://multiqc.info/
GAGE	Bioconductor	https://bmcbioinformatics.biomedcentral.com/articles/10.1186/1471-2105-10-161
Pathview	Bioconductor	https://academic.oup.com/bioinformatics/article/29/14/1830/232698
clusterProfiler	Bioconductor	https://www.sciencedirect.com/science/article/pii/S2666675821000667
CellRanger 5.0.0	10X Genomics	https://support.10xgenomics.com/single-cell-gene-expression/software/overview/welcome
circlize	CRAN	https://academic.oup.com/bioinformatics/article/30/19/2811/2422259
dplyr	CRAN	https://dplyr.tidyverse.org/
ggplot2	CRAN	https://ggplot2.tidyverse.org/
ggsci	CRAN	https://nanx.me/ggsci/
Matrix	CRAN	https://cran.r-project.org/web/packages/Matrix/index.html
pheatmap	CRAN	https://cran.r-project.org/web/packages/pheatmap/index.html
scales	CRAN	https://scales.r-lib.org/
scater	Bioconductor	https://academic.oup.com/bioinformatics/article/33/8/1179/2907823?login=true
Seurat	CRAN	https://satijalab.org/seurat/
SingleCellExperiment	Bioconductor	https://www.nature.com/articles/s41592-019-0654-x
tidyr	CRAN	https://tidyr.tidyverse.org/
viridis	CRAN	https://cran.r-project.org/web/packages/viridis/vignettes/intro-to-viridis.html

(*Continued on next page*)

Continued

REAGENT or RESOURCE	SOURCE	IDENTIFIER
FlowJo versions 10.8.1 - 10.10	BD	https://www.flowjo.com/
GraphPad Prism versions 9-10	GraphPad	https://www.graphpad.com/
R versions 4.1 - 4.3	CRAN	https://cran.rstudio.com/
Rstudio	Posit.co	https://posit.co/download/rstudio-desktop/
digest	CRAN	https://cran.r-project.org/web/packages/digest/index.html
dunn.test	CRAN	Dunn[66]
flowCore	CRAN	https://www.bioconductor.org/packages/release/bioc/html/flowCore.html
ggridges	CRAN	https://cran.r-project.org/web/packages/ggridges/index.html
RANN	CRAN	https://github.com/jefferislab/RANN
RColorBrewer	CRAN	https://cran.r-project.org/web/packages/RColorBrewer/index.html
reshape2	CRAN	https://cran.r-project.org/package=reshape2
EmbedSOM	CRAN	https://github.com/exaexa/EmbedSOM
Rtsne	CRAN	https://cran.r-project.org/package=Rtsne
umap	CRAN	https://cran.r-project.org/package=umap
uwot	CRAN	https://cran.r-project.org/package=Rtsne
ConsensusClusterPlus	Bioconductor	https://academic.oup.com/bioinformatics/article/26/12/1572/281699
FlowSOM	Bioconductor	https://onlinelibrary.wiley.com/doi/full/10.1002/cyto.a.22625
Cross Entropy test	GitHub	https://www.sciencedirect.com/science/article/pii/S2667237522002958; https://github.com/AdrianListon/Cross-Entropy-test
FlowCytoScript	GitHub	https://github.com/DrCytometer/Advanced-flowcytoscript; https://github.com/DrCytometer/Simplified-flowcytoscript
rstan version 2.26	CRAN	https://cran.r-project.org/package=rstan
FlowcodeDecoder	This paper, GitHub	https://github.com/obricard/FlowcodeDecoder
AutoSpill	GitHub	https://www.nature.com/articles/s41467-021-23126-8
Other		
ExpressionViewer	This paper	https://www.bioinformatics.babraham.ac.uk/shiny/expressionViewer/
Markov chain models	This paper, Figure 5	Mendeley Data: https://data.mendeley.com/datasets/czhfj4g6vb/1

RESOURCE AVAILABILITY

Lead contact

Further information and requests for resources and reagents should be directed to and will be fulfilled by the lead contact, Adrian Liston (al989@cam.ac.uk).

Materials availability

Plasmids generated in this study are available upon request. Requests for mouse lines generated in this study should be directed to the lead contact.

Data and code availability

Flow cytometry data have been deposited in Flow Repository and are publicly available as of the date of publication. Reference numbers are listed in the key resources table. Single-cell RNA-seq data have been deposited at GEO and are publicly available as of the date of publication. Accession numbers are listed in the key resources table.

All original code has been deposited in GitHub and is publicly available as of the date of publication. DOIs are listed in the key resources table.

Any additional information required to reanalyze the data reported in this paper is available from the lead contact upon request.

EXPERIMENTAL MODEL AND STUDY PARTICIPANT DETAILS

Mouse strains and strain generation

All mice were housed in SPF conditions unless otherwise stated. All mice used were on the C57BL/6 background. Mice were used at between 7 and 20 weeks of age unless otherwise indicated. Both male and female mice were used for experiments. Equal numbers of male and female mice were used for the tissue screening experiment. For higher success rates, exclusively female mice were used for parabiosis (unless otherwise indicated), and for consistency with these experiments, several other studies were also comprised of female mice. Mouse experimental protocols were approved either by the University of Leuven ethics committee and carried out in accordance with the recommendations of the European Union (EU) concerning the welfare of laboratory animals (Directive 2010/63/EU), or they were approved by the UK Home Office and the Babraham Institute AWERB.

Foxp3$^{Thy1.1}$ and CD45.1 *Foxp3*$^{Thy1.1}$ mice,[67] *Klrg1*^{Cre} *RosaAi14* mice,[68] *CD69*$^{-/-}$ mice,[69] *Rag1*$^{-/-}$ mice,[70] *CD11a*$^{-/-}$ (*Itgal*^{tm1Bll}) mice,[71] CD4Cre *Hif1a*$^{fl/fl}$ mice,[72] Ubiquitin-GFP mice,[73] *Klrg1*$^{-/-}$ mice,[74] *S1pr2*$^{-/-}$ mice (*S1pr2*$^{tm2a(EUCOMM)Hmgu}$), CD4Cre *Blimp1*$^{fl/fl}$[75] and *ST2*$^{-/-}$ (*Il1rl1*^{tm1Anjm}) mice[76] are as previously described. *BATF*$^{-/-}$ bone-marrow (013758) was obtained from JAX for bone-marrow reconstitution.

CD69$^{fl/fl}$ mice were generated using C57BL/6N ES cells, through Cyagen. Briefly, exons 2–4 were targeted for flox site insertion, using homologous arms generated using BAC clones RP23-11N22 and RP23-399O9 as templates. The targeting vector included a self-deleting Neo cassette site, leaving the *CD69*$^{fl/fl}$ mice. Cre activity on this allele results in the deletion of 2382bp spanning exons 2–4, resulting in a frameshift after exon 1 (residue 21) and a stop codon after residue 24. Mice were then crossed to the *Foxp3*^{CreERT2} strain.[77]

CD103$^{-/-}$ mice were generated using direct microinjection of Cas9 protein (IDT, 1μg/μl) and *CD103* gRNA (5μl of 1μM, 5' GTTGAGGCTGCGGAACTTCC-3' targeting exon 5) into C57BL/6 zygotes, followed by transfer into CD1 surrogates. Offspring were screened, and mice bearing a 10bp deletion (aagttccgca) resulting in a frameshift at residue 118 were bred to homozygosity and confirmed for lack of expression by flow cytometry.

Areg$^{-/-}$ mice were generated using direct microinjection of Cas9 protein (IDT, 1μg/μl) and *Areg* gRNA (5μl of 20μM mixed gRNA 5'-TCTGGGGACCACAGTGCCGGTGG-3' and 5'-ATAATATAGCCGGATATTTGTGG-3' targeting exon 2, plus 5μl of 20μM trRNA) into C57BL/6 zygotes, followed by transfer into CD1 surrogates. Offspring were screened by sequencing, and mice bearing a 118bp deletion in exon 2 resulting in a frameshift and early truncation were bred to homozygosity and confirmed for lack of expression by flow cytometry.

METHOD DETAILS

Mouse procedures

Gnotobiotic C57BL/6J mice were housed at the VIB gnotobiotic facility, Ghent. For microbiome enrichment, pet store female mice were wild-exposed prior to cohousing with SPF C57BL/6J mice (KUL L2 animal facility, Leuven). After 12 weeks of cohousing, a subset of mice was tested for 47 pathogens by serology and screened for microbiome diversity by fecal microbiome sequencing, as previously reported.[78]

For parabiosis, Foxp3$^{Thy1.1}$ and CD45.1 Foxp3$^{Thy1.1}$ mice were intercrossed for at least 5 generations prior to starting parabiosis experiments. The congenic mice were then cohoused for one week prior to surgery. Parabiosis surgery was performed as previously described.[79] Mice in which the blood lymphocyte population was not between 40-60% of donor origin after 1 week were excluded from the study. For male:female parabiosis, the two mice were matched in weight rather than age.

Foxp3^{ERT2Cre} *CD69*$^{fl/fl}$ mice were treated with tamoxifen (0.2mg/g) by oral gavage weekly for three weeks.

Competitive mixed bone marrow chimeras were created using equal mixtures of bone marrow. A total of $2x10^6$ cells were injected i.v. into 11 Gy-irradiated CD45.1/CD45.2 heterozygous mice or 5.5Gy-irradiated Rag-deficient mice. Mice were given water containing Baytril (50mg/ml) after irradiation. Chimeras were analyzed 8-12 weeks post-reconstitution.

For retrogenic TCR mice, hematopoietic stem cells (HSC) were isolated as lineage-depleted bone marrow cells using the EasySep Mouse Hematopoietic Progenitor Cell Isolation kit (Stem Cell Technologies), and transduced with retrovirus in the presence of Lentiblast (Oz Biosciences). HSC were cultured in TPO (R&D Systems), IL-3, IL-6, SCF and FLT3L (BioLegend) for 24hr in StemSpan SFEM II medium (Stem Cell Technologies). The transduced cells ($5x10^5$ per mouse) were transplanted into lethally irradiated C57BL/6 mice along with unmanipulated *Rag1*$^{-/-}$ bone marrow ($1x10^6$ cells). Mice were assessed 10 weeks post-transplant.

To test tissue re-homing, leukocytes were isolated from the tissues of congenic strains (CD45.1, CD45.2, CD45.1/CD45.2, Foxp3$^{Thy1.1}$, CD45.1 Foxp3$^{Thy1.1}$, UbGFP, CD45.1 UbGFP, RosaRFP) and combined such that each pool contained uniquely

identifiable Treg cells from each tissue source. The pools were injected i.p. into individual Rag-deficient mice. Cells were recovered and analyzed four weeks post-transfer.

Tissue preparation

Prior to isolating tissue leukocytes, mice were either injected intravenously with anti-CD45 antibody to label vascular leukocytes or they were lethally anesthetized with ketamine/xylazine and perfused with PBS containing 2.5% FCS. Tissues were harvested into HBSS with 2.5% FCS and 2mM EDTA, and stored on ice until further processing. The thymus, lymph nodes, Peyer's patches, spleen, adrenal glands were dispersed with frosted glass microscope slides, filtered through 100μm mesh. Where necessary, erythrocytes were lysed prior to counting using a Countess Automated Cell Counter (ThermoFisher). The liver was prepared similarly, except the resulting cell suspension was washed extensively and centrifuged (600g, 10min) through a 40% Percoll (Sigma Aldrich) solution prior to erythrocyte lysis. Bone marrow was extracted from a single femur by crushing with a mortar and pestle. Blood was treated to lyse red cells prior to staining.

The salivary glands, lungs, pancreas, kidney, adipose tissue, reproductive tissues, eyes, back skin, tongue, hind limb muscle, heart, bladder and brain were digested as follows to extract tissue leukocytes: Tissues were chopped finely with razor blades and washed by centrifugation to remove debris. They were then resuspended in digest buffer (IMDM supplemented with 20% FCS, 10mM HEPES, 1mM sodium pyruvate, 10μg/ml gentamicin, 1mM $CaCl_2$ and 1mM $MgCl_2$) with enzymes (400μg/ml collagenase D, 100μg/ml hyaluronidase and 40μg/ml DNase I, Sigma Aldrich). In some experiments 2mg/ml collagenase IV was used in place of collagenase D. Tissues were shaken in an agitating mixer at 37°C for 15min, dispersed with a pipette, and shaken for another 15min. The solution was then filtered through 100μm mesh and any remaining chunks were forced through the mesh. The cells were washed and passed through 40% Percoll to enrich for the leukocyte fraction. The various parts of the gastrointestinal tract were separated into intraepithelial and lamina proprial compartments using a pre-digest step of agitation at 37°C in HBSS with 10mM HEPES, 10mM EDTA and 2.5% FCS. The released cells were collected and passed through 40% Percoll to isolate the intraepithelial leukocytes (IELs). The remaining tissue was diced finely, digested enzymatically and passed through Percoll to isolate the lamina propria leukocytes (LPLs).

Murine tissue flow cytometry

For murine samples, Fc receptor interactions were blocked using 2.4G2 hybridoma supernatant. Viability staining was performed in HBSS, using either ViaKrome 808 (Beckman Coulter) or Fixable Viability Dye eFluor780 (ThermoFisher). *In vivo* intravenous labeling of leukocytes with anti-CD45-biotin was developed using fluorescent streptavidin. Any epitopes requiring pre-fixation staining were stained for 1 hour at 4°C in the dark in FACS buffer (PBS with 2.5% FCS and 2mM EDTA). Cells were washed with FACS buffer and then fixed. For fluorescent protein retention, cells were fixed at room temperature for 45 minutes in the dark with neutral buffered formalin (VWR). For all other purposes, cells were fixed and permeabilized for 30 minutes using the Foxp3/Transcription Factor Staining Buffer Set (eBioscience). Following two washes with the eBioscience permeabilization buffer, cells were stained overnight (~16hrs) with all remaining antibodies in permeabilization buffer supplemented with 20% 2.4G2 supernatant, as described.[80] Cells were washed and acquired with 10,000 Precision Count beads (BioLegend) added per sample. The antibody cocktails used for the main flow cytometry panels can be found in Data S3. For ageing and cohousing data, the Symphony parabiosis panel was used, with the exception of including Alexa Fluor 488 anti-TCRβ (clone H57-597, BioLegend, 109215; RRID:AB_493344, 1:2500) in place of CD45.1.

Where indicated, antibodies were conjugated to fluorophores according to the manufacturer's instructions. Where possible, free fluorophore was removed using centrifugal filters with a 50kDa cut-off. The following antibody conjugation kits were used in this research: PE/Cy5.5® Conjugation Kit - Lightning-Link®, APC/Cy5.5® Conjugation Kit - Lightning-Link® (AbCam), Alexa Fluor™ 350 Antibody Labeling Kit, Alexa Fluor™ 532 Antibody Labeling Kit, and Alexa Fluor™ 790 Antibody Labeling Kit (ThermoFisher).

Cohousing, gnotobiotic, parabiosis, ageing and $CD103^{-/-}$ chimera data were acquired on a BD FACSymphony A5 flow cytometer (BD Biosciences). The remaining murine data were acquired on an Aurora Spectral Analyzer (Cytek).

FlowCode cloning

TCR coding sequences from murine TCR OTII-2A.pMIG II[81] (Addgene plasmid # 52112; http://n2t.net/addgene:52112; RRID:Addgene_52112) were removed using EcoRI and XhoI and replaced by TCR of interest coding sequences using NEBuilder Hifi DNA assembly and IDT eblocks gene fragments encoding Travj, Trac_P2A, Trbvdj, Trbc1 or Trbc2. EGFP was removed using NcoI and NotI and replaced by H2bc3_AU1_Flag_HA coding sequence using NEBuilder Hifi DNA assembly and an IDT eblocks gene fragment. AU1_Flag_HA was removed using BamHI and NotI and replaced by other Procode tags using NEBuilder Hifi DNA assembly and PCR amplicons generated from NLS-mCherry Pro-Code vector library.[34,35] Plasmid sequences can be found in Data S2.

RNAseq

For bulk RNA sequencing, 2000 $CD4^+$ $Foxp3Thy1.1^+$ Treg cells and $Foxp3Thy1.1^-$ Tconv cells were sorted on a BD FACSAria from each source from perfused mice. RNA was isolated using RNeasy Mini kit (Qiagen). RNA concentration and purity were determined using the Nanodrop ND-1000 (Nanodrop Technologies) and RNA integrity with a Bioanalyser 2100 (Agilent). 3′mRNA-seq library preparation and transcriptome analysis was performed by Lexogen (Austria) using the QuantSeq 3′mRNA-Seq Library Prep Kit for Illumina and QuantSeq data analysis workflow. scRNA-Seq was performed using 10x Genomics 5' VDJ Single Cell Immune

Profiling. Treg cells were flow sorted on a BD Influx, Aria, Jazz or Fusion on the basis of CD4$^+$Foxp3Thy1.1$^+$ i.v.CD45$^-$ CD19$^-$CD11b$^-$CD8$^-$F4/80$^-$. Cells were labeled with Hashtag TotalSeq regents and loaded onto the 10x Chromium Controller. Sequencing was performed on an Illumina HiSeq. Data was processed in R using scripts as detailed below.

Following sequencing of purified tissue Treg cell and Tconv cells populations, the RNAseq data was processed using FastQC[82] for assessing read quality pre-and post-trimming, Trim Galore![83] for trimming adapter sequences, and STAR aligner[84] for aligning to GENCODE[85] mouse primary assembly vM23, with the raw counts being generated by featureCounts.[86] A combined report was generated using MultiQC.[87] Raw counts were isualizat using DESeq2,[88] and global analysis using PCA, t-SNE[89,90] (perplexity parameter at '3') and UMAP[91,92] was performed on the genes post minimum transcript per cell filtering of 0.01 transcripts per cell. Heatmaps were produced using Pearson correlation. Differential expression analysis was performed using the default DESeq2 analysis pipeline, but without using zero-centered Normal priors, $\log_2$ fold change shrinkage, outlier replacement using Cook's distance or independent filtering. The selection criteria was absolute DESeq $\log_2$ beta $\geq$ 2 and adjusted p.value < 0.01. Gene set enrichment analysis was performed using GAGE[93] with the pathway isualization done by Pathview.[94] The script for the RNAseq analysis is available at https://github.com/AdrianListon/TissueTregs. The enriched profiles were compared using the clusterProfiler package.[95] A publicly accessible webtool was developed in R Shiny[96] which provides an interactive bulk RNA-seq data analysis module allowing users to perform custom contrasts to explore the data further for additional results and/or verification. In addition to this module, other modules are also available, such as the TCR module which explores the T cell repertoire in the data. The script for generating the webtool is available at https://github.com/AdrianListon/ExpressionViewer. The webtool is available at https://www.bioinformatics.babraham.ac.uk/shiny/expressionViewer/.

For comparative analysis of most highly expressed genes, the 50 highest expressed genes per tissue are displayed. For comparative analysis of most highly differentially-expressed genes, the gene list was first generated based on statistical difference of samples from blood Treg cells, then up to 50 differentially-expressed genes per tissue were displayed (fewer if less than 50 genes with differential expression within that tissue reached statistical significance). For this analysis 33 genes were removed from the dataset, based on contamination from pancreatic acinar cells in the pancreatic samples (*2210010C04Rik, Amy2a1, Amy2a2, Amy2a3, Amy2a4, Amy2a5, Amy2b, Cel, Cela1, Cela2a, Cela3b, Clps, Cpa1, Cpa2, Cpb1, Ctrb1, Ctrl, Gp2, Klk1, Pdia2, Pla2g1b, Pnlip, Pnliprp1, Pnliprp2, Prss2, Reg1, Rnase1, Spink1, Sycn, Tff2, Try4, Try5, Zg16*). The list of acinar contaminants was independently generated by Julie Stockis and Tim Halim (CRUK Cambridge) on an independent dataset of KLRG1$^+$ and KLRG1$^-$ Treg cells. The list was generated by cross-referencing the genes driving the first principle component of the PCA of KLRG1$^+$ and KLRG1$^-$ pancreatic Treg cells to their pancreatic lymph node counterparts with a gene list of very highly expressed genes from a 10x scRNAseq dataset of acinar cells (manuscript in preparation). The list of probable contaminants was validated here through scRNA data, where the gene signatures present in the pancreatic bulk RNAseq samples (both Treg cell and Tconv cell) were absent in scRNA of Treg cell sorted from the pancreas.

For TCR sequence analysis, scRNA data was used to allow for paired TCR$\alpha\beta$ chain identification. Row sequencing data was processed with CellRanger 5.0.0 without barcode mismatches allowed and with multi-features analysis (gene expression, vdj-t, totalseq hashtags). Features were linked based on cell barcodes and tissue origin was retrieved based on hashtags signals when highest hashtag count was at least 30 times higher than the others using a custom R script. Gene expression and TCR repertoire analysis were generated in R using circlize, dplyr, ggplot2, ggsci, Matrix, pheatmap,scales, scater, Seurat, SingleCellExperiment, tidyr, viridis packages. For repertoire analysis, a TCR clonotype is associated to a unique set of Trav, tra_cdr3, trbv, trb_cdr3. The custom script is available at: https://github.com/AdrianListon/TissueTregTCR.

QUANTIFICATION AND STATISTICAL ANALYSIS

FlowJo version 10.8.1 (BD), GraphPad Prism 9, R version 4.1.2, RStudio, and CellRanger (10X Genomics) were used for analysis. Within the R environment, the following packages were employed: digest, dunn.test, flowCore, ggplot2, ggridges, RANN, RcolorBrewer, reshape2, EmbedSOM, Rtsne, umap, ConsensusClusterPlus, FlowSOM, Seurat and dplyr. Flow cytometry spillover compensation was calculated using AutoSpill.[97] Major tissue groups (blood-like, bone-marrow, lymphoid, tissue, gut) were organically derived through assessment of marker positivity on tissue Treg cells from 48 organs, using FlowSOM consensus clustering on a tSNE dimensionality reduction. To assess phenotypic divergence in tissue Treg cells following genetic disruption of key genes, we measured the Euclidean distance between wildtype and deficient samples from a given tissue on a PCA based on FlowSOM cluster distributions. For a given wildtype to deficient comparison, FlowSOM clustering was performed on flow cytometry measurements of Treg cell markers. A PCA was performed to remove any co-linearity. Within each tissue pairwise distances between wildtype and deficient samples were calculated, and the median distance was used. To create an interpretable scale, we also measured the median distance between wildtype samples of blood and wildtypesamples from each other category (BM, Lymphoid, Tissue, GALT). On the heatmap, each column (genetic perturbation) is re-scaled from 0 - 100. Samples with a high or variable pairwise distance within a tissue from a single genotype were flagged for manual inspection. Statistical tests used are indicated in the figure legends, typically a two-way ANOVA with Tukey's or Šídák's multiple comparisons. Statistical comparisons of tSNE plots were performed with the Cross Entropy test, using Kolmogorov-Smirnov tests with Holm correction.[98]

The scripts used for flow cytometry data analysis and tSNE Cross Entropy comparisons are available on GitHub: https://github.com/AdrianListon/Cross-Entropy-test. An updated, faster version is available at https://github.com/DrCytometer/Advanced-flowcytoscript, and a simplified version can be found at https://github.com/DrCytometer/Simplified-flowcytoscript. Individual

parameter files for these analyses are uploaded with the individual data sets on FlowRepository. Immunopeptidome reanalysis was based on the published $H2D^d$ immunopeptidome of 19 normal tissues from C57BL/6 mice.[33]

Parabiosis data (proportions of cell states (resting, activated, $CD69^+$ Treg cells) in each of 17 tissues and blood measured at weeks 0, 1, 2, 4, 8, 12 in each parabiont) was modelled by continuous time Markov Chains using a Bayesian approach. The aim was to describe the observed data (flow cytometry data of T cell types and state proportions evolving in time), while directly estimating the biological flow/transition rates including their distributions, i.e., the biological process governing the observed data. Independently for each tissue, the Markov Chain models the whole body Treg cell dynamics using 9 model states (3 body compartments (blood, selected tissue, all other tissues pooled) x 3 cell states (resting, activated, CD69+)) and possible flows between them. The assumed prior distributions of flow rates were selected as uniform on the support 2-3 orders of magnitude larger than the final posterior estimates in order to provide the least information and robustness. The models were fitted using Markov Chain Monte Carlo (MCMC) algorithm, specifically Hamiltonian Monte Carlo (HMC) in the Stan programming language, while using the rstan 2.26 package, interface for R language. Each Markov Chain model was estimated by four Monte Carlo chains with 5,000 samples. The fits of the aggregate models were assessed against the empirical data collected, and used to calculate probabilistic dwell times.[99] The flow rate estimates were provided as mode posterior together with 80% highest density (credible) interval (HDI). The full pipeline is available at https://github.com/gergelits/markov_chain_tissue_treg.

Retrogenic TCR analysis via FlowCodes was assessed using FlowJo v10.8.1 to extract $CD4^+$ T cell-related events and then analyzed with the custom FlowCode Decoder shiny app to obtain count and expression levels per TCR clone. The FlowCode Decoder script is available on GitHub: https://github.com/obricard/FlowcodeDecoder. Graphs were generated in R 4.1.2 using ggplot2.

ADDITIONAL RESOURCES

In order to aid the reader in exploring and visualizing the complex datasets in this publication, we have created ExpressionViewer, a Shiny web interface accessible at https://www.bioinformatics.babraham.ac.uk/shiny/expressionViewer/. The Markov chain models of the tissue Treg cell circulation from parabiosis experiments are available at Mendeley Data: https://data.mendeley.com/datasets/czhfj4g6vb/1.

Immunity, Volume *57*

Supplemental information

The tissue-resident regulatory T cell pool is shaped by transient multi-tissue migration and a conserved residency program

Oliver T. Burton, Orian Bricard, Samar Tareen, Vaclav Gergelits, Simon Andrews, Laura Biggins, Carlos P. Roca, Carly Whyte, Steffie Junius, Aleksandra Brajic, Emanuela Pasciuto, Magda Ali, Pierre Lemaitre, Susan M. Schlenner, Harumichi Ishigame, Brian D. Brown, James Dooley, and Adrian Liston

Supplementary Material

Supplementary Figure 1. Phenotypic unity for tissue-resident Treg cells across multiple organs. Wildtype mice, aged 12-20 weeks, were injected with intravenous anti-CD45 antibody label and assessed for flow cytometry. Treg cells were purified from 48 organs: blood, thymus, spleen, bone marrow, cervical LN, submandibular LN, axillary LN, inguinal LN, popliteal LN, pancreatic LN, mediastinal LN, renal LN, aortic LN, jejunal LN, colonic LN, skin, lung, pancreas, salivary gland, liver, kidney, tongue, heart, muscle, white fat, brown fat, brain, female reproductive tract, urethra, testes, prostate, bladder, peritoneum, duodenal Peyer's Patches, jejunal Peyer's Patches, ileal Peyer's Patches, stomach IEL, duodenal IEL, Jejunal IEL, ileal IEL, cecal IEL, colonic IEL, stomach LPL, duodenal LPL, jejunal LPL, ileal LPL, cecal LPL, and colonic LPL. Cells stained as positive for intravenous anti-CD45 antibody were gated out prior to downstream analysis. **A)** UMAP plots of high parameter flow analysis of gated tissue Treg cells, built upon expression of GITR, TIM3, CCR3, TIGIT, Ly-6C, CCR9, CCR6, CXCR3, CCR2, KLRG1, ST2, CD62L, Neuropilin, CD69, CD44, CD25, CD95, TNFRII, ICOS, PD-1. **B)** Heatmap of phenotypic marker expression in Treg cells from each tissue, clustered by similarity, for each marker. Relates to **Figure 1**.

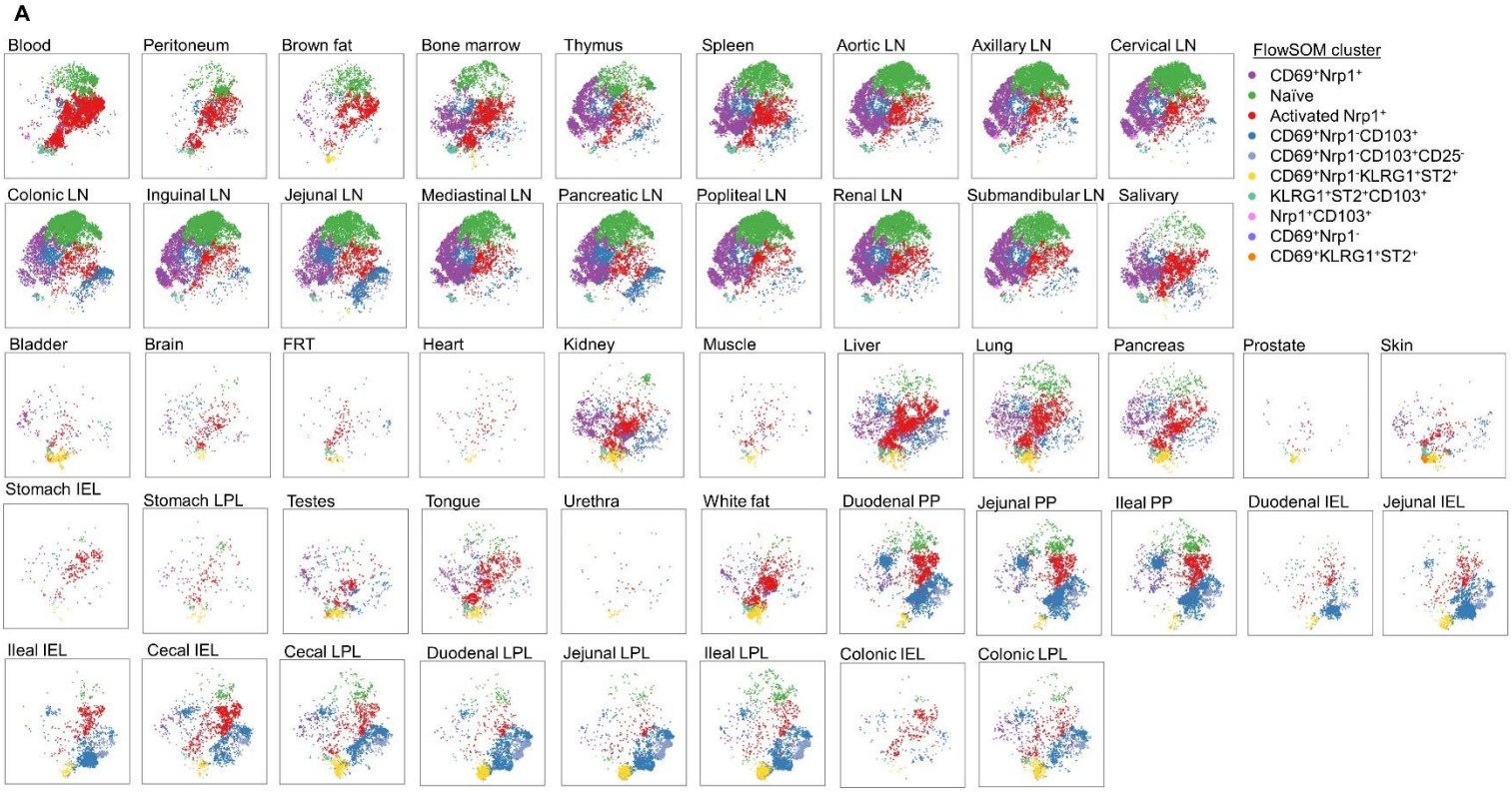
A
Blood
Peritoneum
Brown fat
Bone marrow
Thymus
Spleen
Aortic LN
Axillary LN
Cervical LN
Colonic LN
Inguinal LN
Jejunal LN
Mediastinal LN
Pancreatic LN
Popliteal LN
Renal LN
Submandibular LN
Salivary
Bladder
Brain
FRT
Heart
Kidney
Muscle
Liver
Lung
Pancreas
Prostate
Skin
Stomach IEL
Stomach LPL
Testes
Tongue
Urethra
White fat
Duodenal PP
Jejunal PP
Ileal PP
Duodenal IEL
Jejunal IEL
Ileal IEL
Cecal IEL
Cecal LPL
Duodenal LPL
Jejunal LPL
Ileal LPL
Colonic IEL
Colonic LPL
FlowSOM cluster
CD69+Nrp1+
Naïve
Activated Nrp1+
CD69+Nrp1-CD103+
CD69+Nrp1-CD103+CD25-
CD69+Nrp1-KLRG1+ST2+
KLRG1+ST2+CD103+
Nrp1+CD103+
CD69+Nrp1-
CD69+KLRG1+ST2+

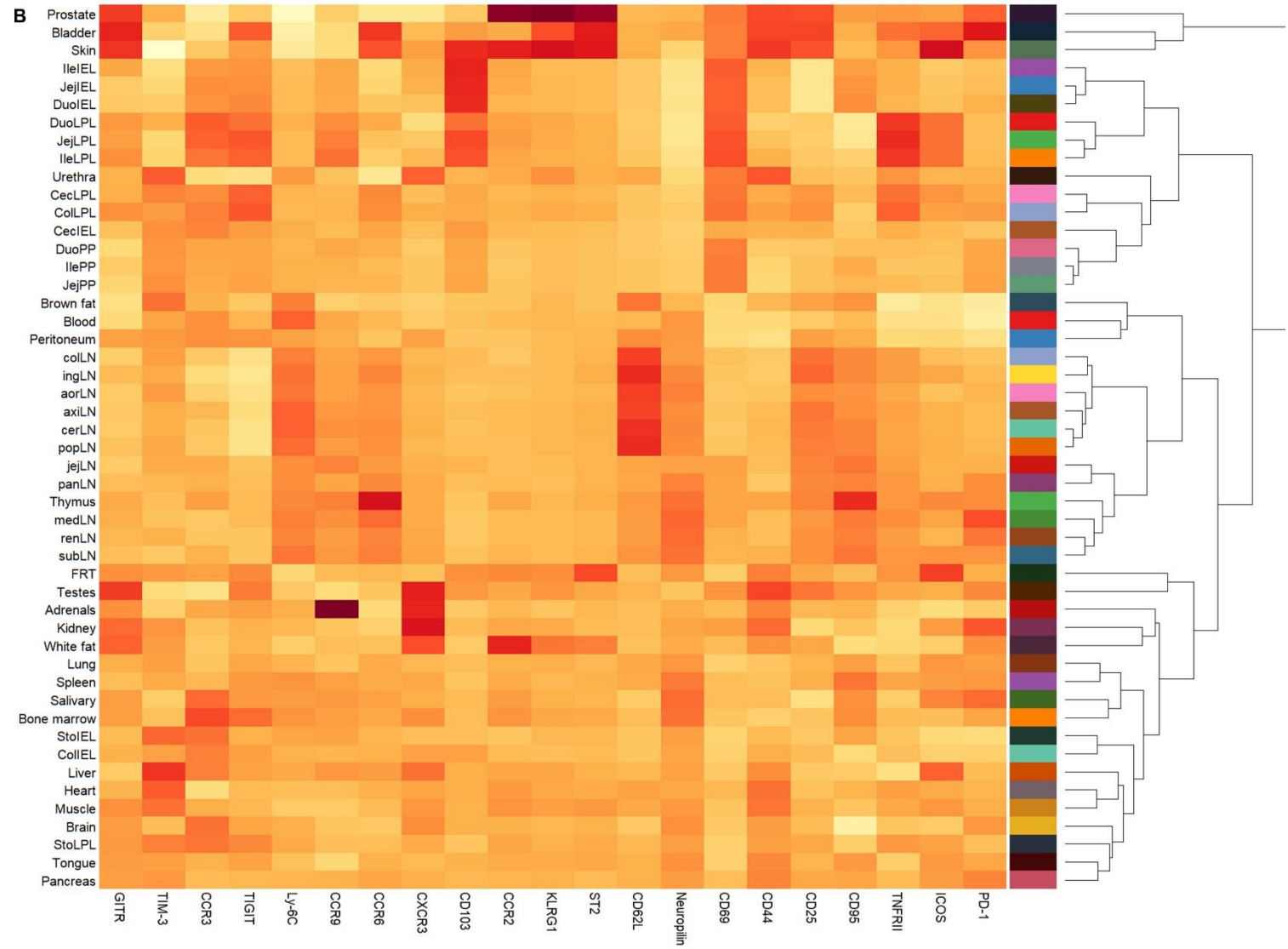
B
Prostate
Bladder
Skin
IleIEL
JejIEL
DuoIEL
DuoLPL
JejLPL
IleLPL
Urethra
CecLPL
ColLPL
CecIEL
DuoPP
IlePP
JejPP
Brown fat
Blood
Peritoneum
colLN
ingLN
aorLN
axiLN
cerLN
popLN
jejLN
panLN
Thymus
medLN
renLN
subLN
FRT
Testes
Adrenals
Kidney
White fat
Lung
Spleen
Salivary
Bone marrow
StoIEL
ColIEL
Liver
Heart
Muscle
Brain
StoLPL
Tongue
Pancreas
GITR
TIM-3
CCR3
TIGIT
Ly-6C
CCR9
CCR6
CXCR3
CD103
CCR2
KLRG1
ST2
CD62L
Neuropilin
CD69
CD44
CD25
CD95
TNFRII
ICOS
PD-1

Supplementary Figure 2. Phenotypic identification of tissue-residency. A) Wildtype mice, aged 16 weeks, were injected with intravenous anti-CD45-PE antibody label and perfused prior to tissue Treg cell isolation for flow cytometry analysis. Representative gating of Treg cell and i.v. CD25 antibody labelling. **B)** Fraction of Treg cells labeled by i.v. injection of anti-CD45-PE (n=4). **C)** Tissue Treg cell phenotypes were compared by tSNE and FlowSOM cluster overlay for blood vs kidney Treg cells, with kidney Treg cells separated into the vascular (CD45-PE^{+}) population, a potentially perivascular CD45-PE^{mid} population and the tissue-embedded CD45-PE^{-} populations. **D)** Heat map and **E)** UMAP for tissue Treg cell phenotypes were compared by tSNE and FlowSOM cluster overlay for blood vs combined lymphoid, non-lymphoid and gut-associated Treg cells, with these Treg cells separated into the vascular (CD45-PE^{+}) population, a potentially perivascular CD45-PE^{low} population and the tissue-embedded CD45-PE^{-} populations. **F)** Blood, LN, skin and spleen were isolated for tissue Treg cell phenotyping by flow cytometry. Spleen samples were either given the standard (lymphoid tissue) mechanical disruption or (the non-lymphoid protocol of) enzymatic tissue digestion. Total leukocyte and **G)** Treg cell numbers for spleen samples prepared by mechanical or enzymatic digestion of the spleen. **H)** Frequency of Treg cells among the isolated CD4^{+} T cell population, for spleen samples prepared by mechanical or enzymatic digestion of the spleen. Statistical analysis by Šídák's multiple comparison test on 2-way ANOVA. **I)** Phenotypic comparison of mechanical and enzymatic splenic Treg cells, using blood, lymphoid (cervical LN) and non-lymphoid (skin) out-groups. Displayed by PCA or **J)** UMAP, with **K)** quantified FlowSOM clusters. Statistical analysis by Tukey's multiple comparison test on 2-way ANOVA, showing only p values for significant differences between spleen mechanical and spleen enzymatic populations. **L)** Heat map of the Treg cell expression of the markers used for PCA and UMAP analysis, GITR, TIM3, CCR3, TIGIT, Ly-6C, CCR9, CCR6, CXCR3, CCR2, KLRG1, ST2, CD62L, Neuropilin, CD69, CD44, CD25, CD95, TNFRII, ICOS, PD-1. Relates to **Figure 1**.

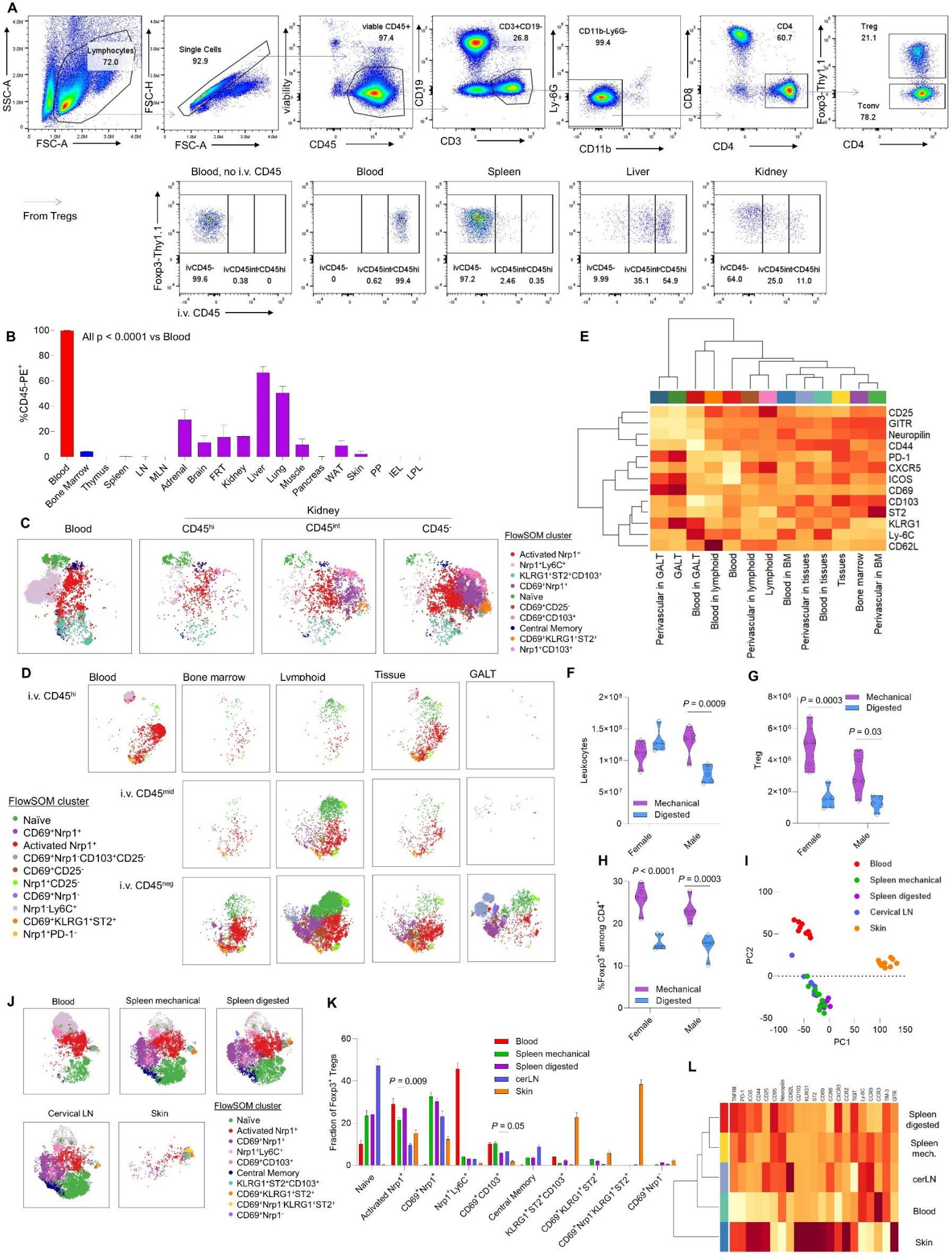
A
Lymphocytes 72.0
Single Cells 92.9
viable CD45+ 97.4
CD3+CD19- 26.8
CD11b-Ly6G- 99.4
CD4 60.7
Treg 21.1
Tconv 78.2
SSC-A
FSC-A
FSC-H
viability
CD45
CD19
CD3
Ly-6G
CD11b
CD8
CD4
Foxp3-Thy1.1
From Tregs
Blood, no i.v. CD45
Blood
Spleen
Liver
Kidney
ivCD45- 99.6
ivCD45int/CD45hi 0.38 0
ivCD45- 0
ivCD45int/CD45hi 0.62 99.4
ivCD45- 97.2
ivCD45int/CD45hi 2.46 0.35
ivCD45- 9.99
ivCD45int/CD45hi 35.1 54.9
ivCD45- 64.0
ivCD45int/CD45hi 25.0 11.0
i.v. CD45
B
All p < 0.0001 vs Blood
%CD45-PE+
Blood
Bone Marrow
Thymus
Spleen
LN
MLN
Adrenal
Brain
FRT
Kidney
Liver
Lung
Muscle
Pancreas
WAT
Skin
PP
IEL
LPL
C
Blood
Kidney
CD45hi
CD45int
CD45-
FlowSOM cluster
Activated Nrp1+
Nrp1+Ly6C+
KLRG1+ST2+CD103+
CD69+Nrp1+
Naïve
CD69+CD25-
CD69+CD103+
Central Memory
CD69+KLRG1+ST2+
Nrp1+CD103+
D
Blood
Bone marrow
Lymphoid
Tissue
GALT
i.v. CD45hi
i.v. CD45mid
i.v. CD45neg
FlowSOM cluster
Naïve
CD69+Nrp1+
Activated Nrp1+
CD69+Nrp1-CD103+CD25-
CD69+CD25-
Nrp1+CD25-
CD69+Nrp1-
Nrp1-Ly6C+
CD69+KLRG1+ST2+
Nrp1+PD-1-
E
CD25
GITR
Neuropilin
CD44
PD-1
CXCR5
ICOS
CD69
CD103
ST2
KLRG1
Ly-6C
CD62L
Perivascular in GALT
GALT
Blood in GALT
Blood in lymphoid
Blood
Perivascular in lymphoid
Lymphoid
Blood in BM
Perivascular in tissues
Blood in tissues
Tissues
Bone marrow
Perivascular in BM
F
Leukocytes
P = 0.0009
Mechanical
Digested
Female
Male
G
Treg
P = 0.0003
P = 0.03
Mechanical
Digested
Female
Male
H
%Foxp3+ among CD4+
P < 0.0001
P = 0.0003
Mechanical
Digested
Female
Male
I
Blood
Spleen mechanical
Spleen digested
Cervical LN
Skin
PC1
PC2
J
Blood
Spleen mechanical
Spleen digested
Cervical LN
Skin
FlowSOM cluster
Naïve
Activated Nrp1+
CD69+Nrp1+
Nrp1+Ly6C+
CD69+CD103+
Central Memory
KLRG1+ST2+CD103+
CD69+KLRG1+ST2+
CD69+Nrp1-KLRG1+ST2+
CD69+Nrp1-
K
Fraction of Foxp3+ Tregs
Blood
Spleen mechanical
Spleen digested
cerLN
Skin
P = 0.009
P = 0.05
Naive
Activated Nrp1+
CD69+Nrp1+
Nrp1+Ly6C+
CD69+CD103+
Central Memory
KLRG1+ST2+CD103+
CD69+KLRG1+ST2+
CD69+Nrp1+KLRG1+ST2+
CD69+Nrp1-
L
TNFRII
PD-1
ICOS
CD44
CD25
CD95
Neuropilin
CD62L
CD103
KLRG1
ST2
CD69
CCR6
CXCR3
CCR2
TIGIT
Ly6C
CCR9
CCR3
IL-13
GITR
Spleen digested
Spleen mech.
cerLN
Blood
Skin

Supplementary Figure 3. Minor effects of sex on tissue Treg cell number and phenotype across multiple tissues. Wildtype mice, aged 12-20 weeks, were injected with intravenous anti-CD45 antibody label. Major tissues were dissected and lymphocytes purified for flow cytometric analysis of Treg cell populations. **A)** Frequency of Treg cells among $CD4^+$ $TCR\beta^+$ T cells, per organ, for female and male mice (n=5/group, representative of two independent experiments). No statistically significant differences by Šídák's multiple comparisons test on 2-way ANOVA. **B)** Absolute number of Treg cells recorded per tissue, box-and-whisker plots showing 2.5-97.5% interval. Statistical analysis by by Šídák's multiple comparisons test on 2-way ANOVA. **C)** tSNE plots showing Treg cell phenotype in male or female Treg cells, gated as viable $CD45^+CD3^+CD4^+Foxp3^+$ intravenously labeled $CD45^-$ and built on CCR2, CCR3, CCR6, CCR9, CD25, CD44, CD62L, CD69, CD95, CD103, CXCR3, GITR, ICOS, KLRG1, Ly-6c, Neuropilin, PD-1, ST2, TIGIT, Tim-3 and TNFRII for major tissue groups. **D)** tSNE plots showing comparisons of the most numerically sexually dimorphic non-lymphoid tissues: reproductive tissue, white adipose tissue, salivary gland, with kidney as a reference tissue. P-values by KS test on crossentropy (tSNE-diff) for each pair. Relates to **Figure 2**.

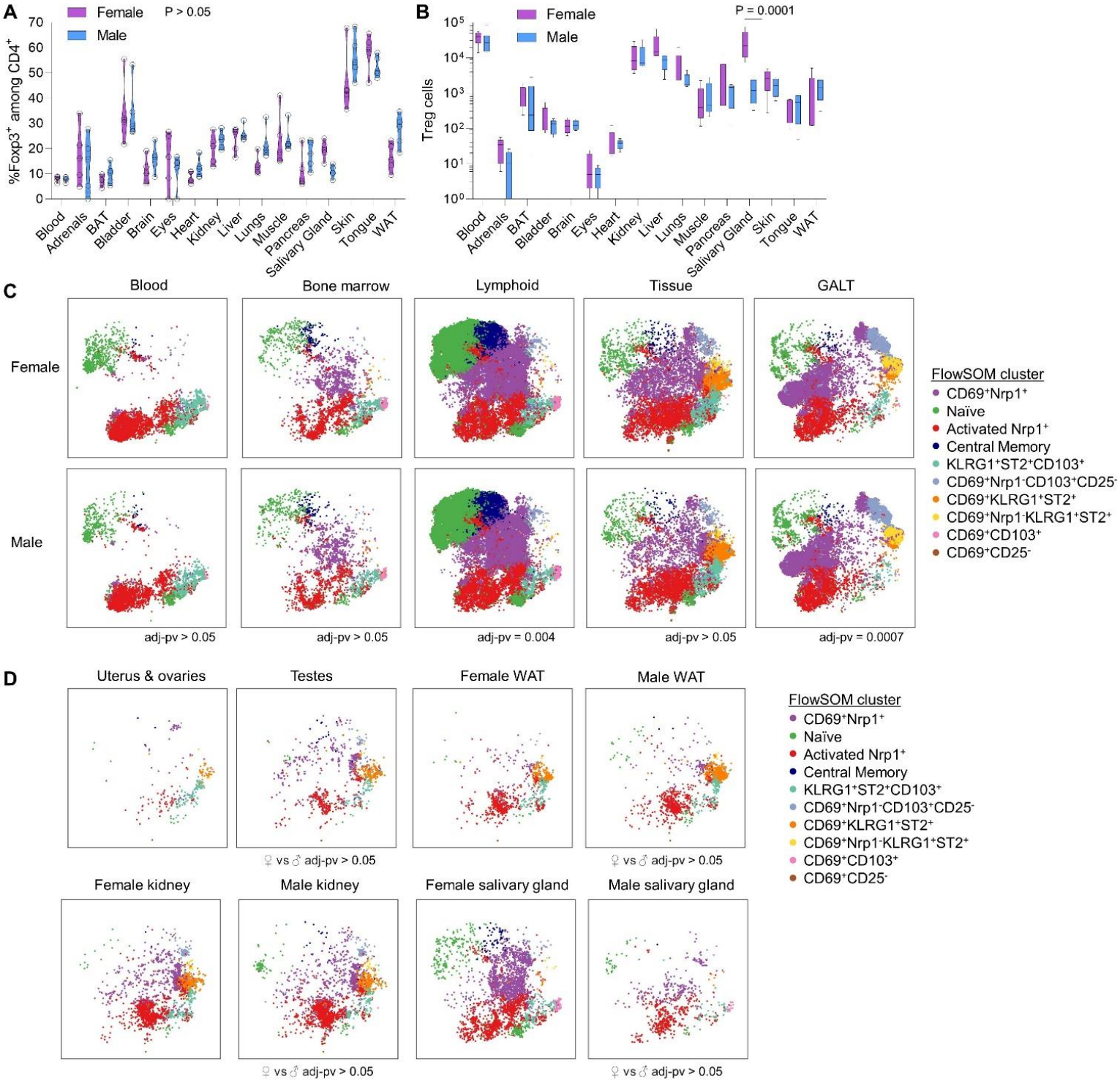
A
Female
Male
P > 0.05
%Foxp3+ among CD4+
70
60
50
40
30
20
10
0
Blood
Adrenals
BAT
Bladder
Brain
Eyes
Heart
Kidney
Liver
Lungs
Muscle
Pancreas
Salivary Gland
Skin
Tongue
WAT
B
Female
Male
P = 0.0001
Treg cells
10^5
10^4
10^3
10^2
10^1
10^0
Blood
Adrenals
BAT
Bladder
Brain
Eyes
Heart
Kidney
Liver
Lungs
Muscle
Pancreas
Salivary Gland
Skin
Tongue
WAT
C
Blood
Bone marrow
Lymphoid
Tissue
GALT
Female
Male
adj-pv > 0.05
adj-pv > 0.05
adj-pv = 0.004
adj-pv > 0.05
adj-pv = 0.0007
FlowSOM cluster
CD69+Nrp1+
Naïve
Activated Nrp1+
Central Memory
KLRG1+ST2+CD103+
CD69+Nrp1-CD103+CD25-
CD69+KLRG1+ST2+
CD69+Nrp1-KLRG1+ST2+
CD69+CD103+
CD69+CD25-
D
Uterus & ovaries
Testes
Female WAT
Male WAT
♀ vs ♂ adj-pv > 0.05
♀ vs ♂ adj-pv > 0.05
Female kidney
Male kidney
Female salivary gland
Male salivary gland
♀ vs ♂ adj-pv > 0.05
♀ vs ♂ adj-pv > 0.05
FlowSOM cluster
CD69+Nrp1+
Naïve
Activated Nrp1+
Central Memory
KLRG1+ST2+CD103+
CD69+Nrp1-CD103+CD25-
CD69+KLRG1+ST2+
CD69+Nrp1-KLRG1+ST2+
CD69+CD103+
CD69+CD25-

Supplementary Figure 4. Impact of age and microbiome on tissue-resident Treg cells. Mice were perfused and assessed by flow cytometry for tissue Treg cell number and phenotype at 8, 12, 20, 30, 52 and 100 weeks of age (n=5-8). **A)** Fold change in Treg cell number in the blood, bone-marrow, lymphoid tissues (thymus, spleen, LN, mLN), non-lymphoid tissues (skin, muscle, female reproductive tract, lungs, pancreas, brain, white adipose tissue, liver, kidney, adrenals) and gut-associated tissues (Peyer's patches and small intestine IEL and LPL). Tissues displayed on multiple graphs according to the scale of the fold-change. **B)** Frequency of Treg cells within $CD4^+$ T cell population per tissue and age group, n.d. = not done. P values refer to effect of age, through linear regression testing. **C)** tSNE of Treg cell phenotype among blood, bone-marrow, lymphoid tissues, non-lymphoid tissues and gut-associated tissues at each age, gated on viable $CD45^+CD3^+CD4^+Foxp3^+$ and built on CD103, CD62L, CTLA-4, CD25, CD44, ICOS, PD-1, KLRG1, Neuropilin, T-bet, Helios, CD69, ST2 and Ki67. **D)** SPF-housed mice, gnotobiotic (germ-free) mice and wild-exposed co-housed mice (n=9, 6, 12) perfused and assessed by flow cytometry for tissue Treg cell phenotype at 8-12 weeks of age, displayed as PCA plots of expression for the same markers as in C. Graphs separated into blood, bone-marrow, lymphoid tissues (thymus, spleen, LN, mLN), non-lymphoid tissues (skin, muscle, female reproductive tract, lungs, pancreas, brain, white adipose tissue, liver, kidney, adrenals) and gut-associated tissues (Peyer's patches and small intestine IEL and LPL). Relates to **Figure 2**.

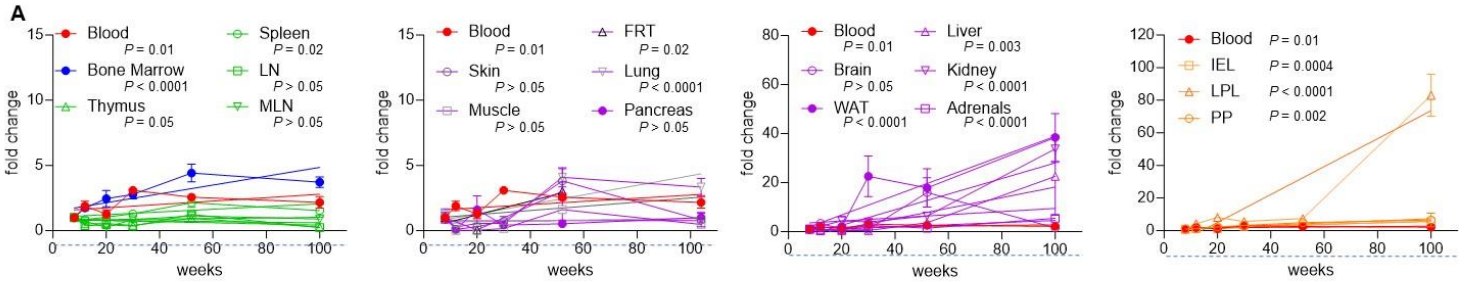
A
Blood P = 0.01
Bone Marrow P < 0.0001
Thymus P = 0.05
Spleen P = 0.02
LN P > 0.05
MLN P > 0.05
Blood P = 0.01
Skin P > 0.05
Muscle P > 0.05
FRT P = 0.02
Lung P < 0.0001
Pancreas P > 0.05
Blood P = 0.01
Brain P > 0.05
WAT P < 0.0001
Liver P = 0.003
Kidney P < 0.0001
Adrenals P < 0.0001
Blood P = 0.01
IEL P = 0.0004
LPL P < 0.0001
PP P = 0.002
fold change
weeks

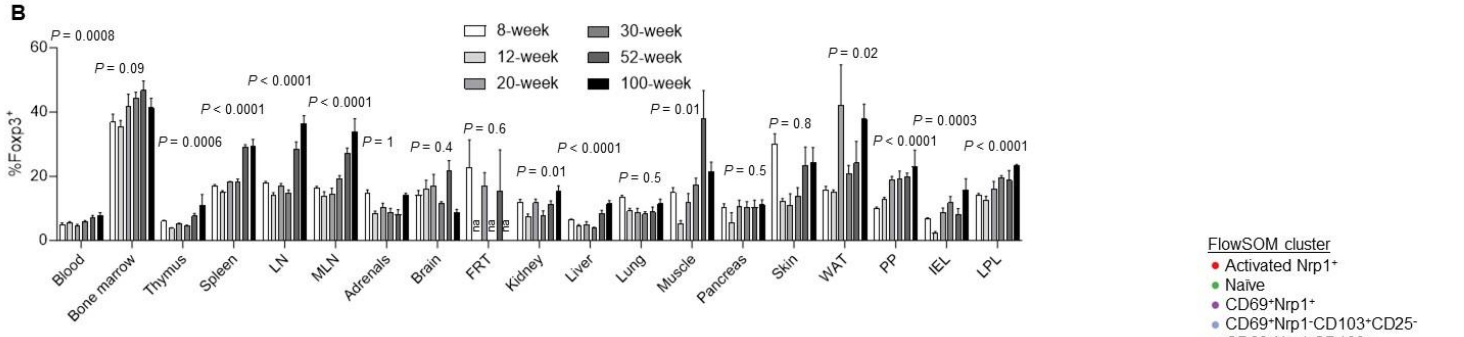
B
8-week
12-week
20-week
30-week
52-week
100-week
%Foxp3+
P = 0.0008
P = 0.09
P = 0.0006
P < 0.0001
P < 0.0001
P < 0.0001
P = 1
P = 0.4
P = 0.6
P = 0.01
P < 0.0001
P = 0.5
P = 0.01
P = 0.5
P = 0.8
P = 0.02
P < 0.0001
P = 0.0003
P < 0.0001
Blood
Bone marrow
Thymus
Spleen
LN
MLN
Adrenals
Brain
FRT
Kidney
Liver
Lung
Muscle
Pancreas
Skin
WAT
PP
IEL
LPL

C
Weeks of age
8
12
20
30
52
100
Blood
Bone marrow
Lymphoid
Tissue
GALT
FlowSOM cluster
Activated Nrp1+
Naïve
CD69+Nrp1+
CD69+Nrp1-CD103+CD25-
CD69+Nrp1-CD103+
KLRG1+ST2+CD103+
CD69+KLRG1+ST2+
Central Memory
CD69+CD103+
Nrp1+PD-1-

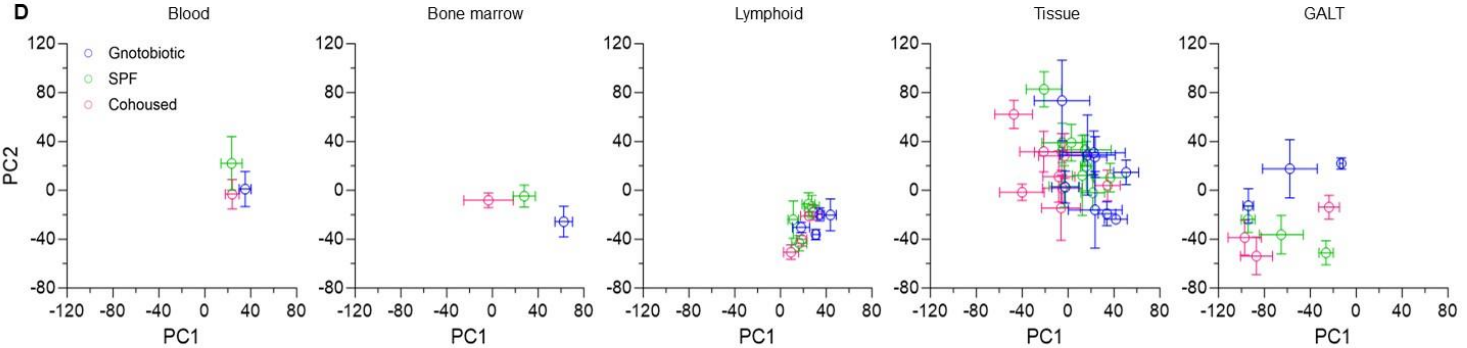
D
Blood
Bone marrow
Lymphoid
Tissue
GALT
Gnotobiotic
SPF
Cohoused
PC2
PC1

Supplementary Figure 5. Immunopeptidome overlap between tissues. Reanalysis of a published H2D^{d} immunopeptidome of 19 normal tissues from C57BL/6 mice mass spectrometry dataset [35]. **A)** The fraction of spectral count that correspond to peptides detected only in a single tissue (Unique), in 2-9 tissues (Some), in 10-18 tissue (Most) or in all tissues (All). **B)** Distribution of the spectral count frequency of each peptide depending on their sharing group. Relates to **Figure 6**.

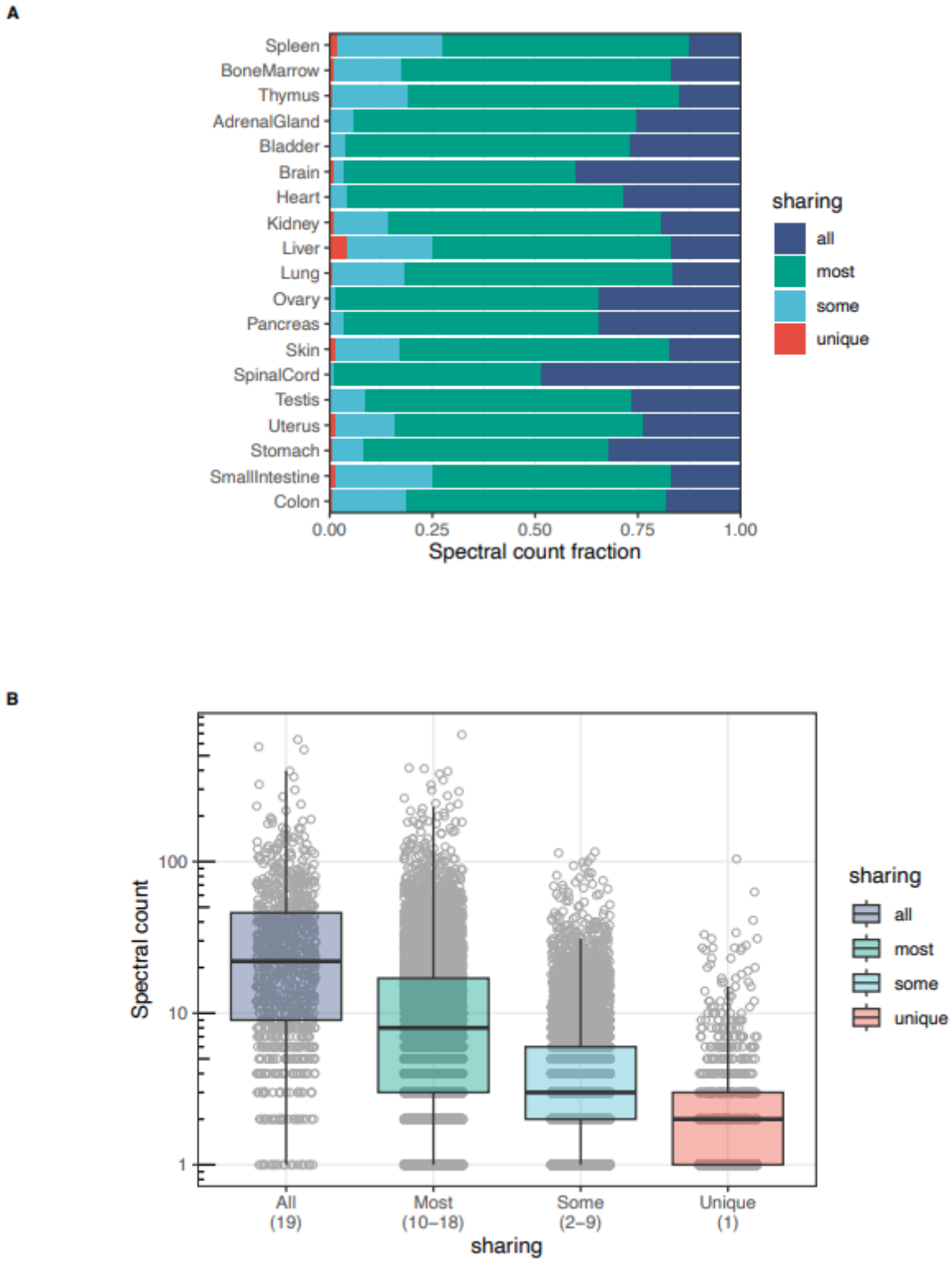

Supplementary Figure 6. Selection of multiplexed tissue Treg cell TCR retrogenics to reflect the common properties of tissue Treg cell TCRs. A) The selected TCR panel, representative of the TCRs cloned from the tissue Treg cell population as a whole, were cloned into FlowCode retroviruses, combining the TCRα and TCRβ sequences with a unique triplicate ProCode epitope combination. **B)** Rag-deficient bone-marrow stem cells were individually transduced with the 20 retroviruses and pooled for reconstitution of irradiated mice. After 10 weeks, mice were injected with anti-CD45 antibody and tissue samples were prepared for analysis by flow cytometry. Cells stained as positive for intravenous anti-CD45 antibody were gated out prior to downstream analysis. FlowCodeDecoder was used to assign each T cell to the appropriate TCR clone, based on expression of the 7 epitopes. **C)** *Foxp3*$^{Thy1.1}$ male mice at 16 weeks of age were injected with intravenous anti-CD45 antibody label prior to FACS sorting of Treg cells from blood, kidney, liver, pancreas and LPL (n=4) for analysis by scTCRseq. Cells stained as positive for intravenous anti-CD45 antibody were gated out prior to downstream analysis. Top 20 TCRs from the scSeq database, ranked based on the total number of samples the clonotype was detected in. Heatmaps represent the frequency of detection of each clone, across the 5 tested tissues and 4 replicate mice. TCR clones 01-10, selected for retrogenic analysis, are marked. **C)** Top 10 TCRs from the scSeq database, ranked based on the frequency with which the clonotypes were detected in mouse 1 kidney, liver, pancreas and LPL samples. Heatmaps represent the frequency of detection of each clone, across the 5 tested tissues and 4 replicate mice. **D)** TCR clones 11-21, constituting the top three clones from each tissue, were selected for retrogenic analysis. **E)** Plot showing tissue Treg cell TCRs, based on the total number of cells in which the clone was detected and the number of samples it was detected in (including both replicate mice and different tissue samples, not including the blood). Selected clones are indicated and named. **F)** Bar graph based on public tissue Treg cell clones (identified in at least two mice, with at least one count per mouse), indicating the fraction that were observed in only a single tissue across multiple mice ("tissue-restricted"), a single tissue plus blood ("tissue/blood-restricted") or across multiple tissues ("multi-tissue). Parallel analysis made on the 20 selected TCRs. **G)** Rag-deficient bone-marrow stem cells were individually transduced with the 20 retroviruses and pooled for reconstitution of irradiated mice. After 10 weeks, tissue samples were prepared for analysis by flow cytometry. FlowCodeDecoder was used to assign each T cell to the appropriate TCR clone, based on expression of the 7 epitopes. Individual results from T cells derived from each of the FlowCode retrogenic TCRs, across the assessed tissues of spleen, LN, kidney, lung, liver, pancreas and LPLs. For each clone and tissue is shown the absolute cell count of detected $CD4^+$ T cells (size) together with the frequency of Treg cells within the population (indicate by colour, with percentage listed on each sample). Relates to **Figure 6**.

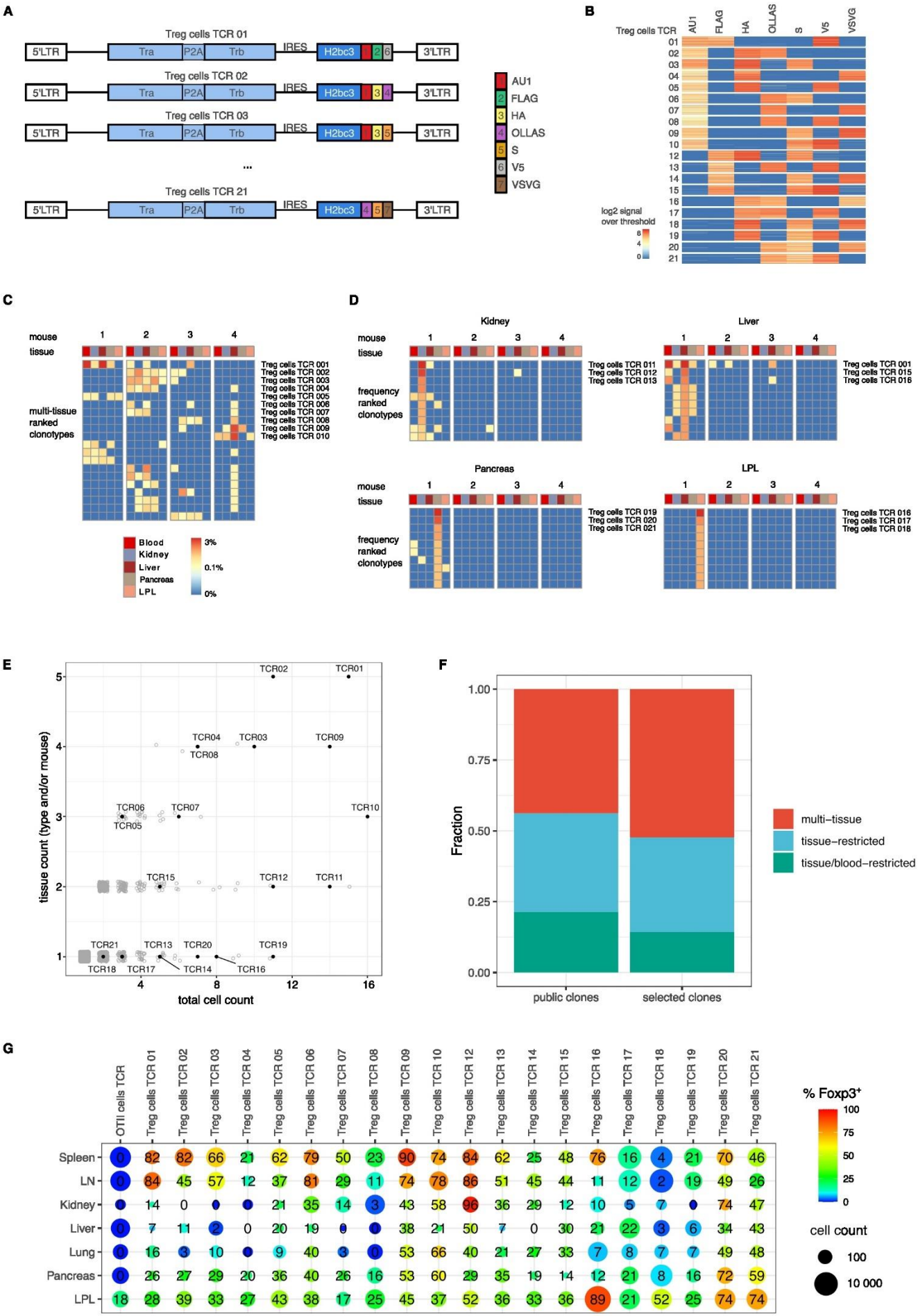
A
Treg cells TCR 01
5'LTR
Tra
P2A
Trb
IRES
H2bc3
3'LTR
Treg cells TCR 02
Treg cells TCR 03
...
Treg cells TCR 21
AU1
FLAG
HA
OLLAS
S
V5
VSVG
B
Treg cells TCR
log2 signal over threshold
C
mouse
tissue
multi-tissue ranked clonotypes
Blood
Kidney
Liver
Pancreas
LPL
3%
0.1%
0%
D
Kidney
Liver
Pancreas
LPL
frequency ranked clonotypes
E
tissue count (type and/or mouse)
total cell count
F
Fraction
public clones
selected clones
multi-tissue
tissue-restricted
tissue/blood-restricted
G
OTII cells TCR
Spleen
LN
Kidney
Liver
Lung
Pancreas
LPL
% Foxp3+
cell count
100
10 000

Supplementary Figure 7. No correlation between CD69 expression and single-tissue vs multi-tissue clonality status among tissue Treg cell TCRs. A) *Foxp3*$^{Thy1.1}$ male mice at 16 weeks of age were injected with intravenous anti-CD45 antibody label prior to FACS sorting of Treg cells from blood, kidney, liver, pancreas and LPL (n=4) for analysis by scTCRseq. Cells stained as positive for intravenous anti-CD45 antibody were gated out prior to downstream analysis. TCR clones, were categorised as single-tissue or multi-tissue based on the detected samples. Analysis limited to clones detected at least three times. CD69 mRNA expression and **B)** CD69 protein expression is displayed per mouse, and average across biological samples. **C)** Reciprocal analysis, with Treg cells classified as CD69^{+} at the mRNA or **D)** protein feature level, and assessed for the percentage of clones with a multi-tissue detection. **E)** Rag-deficient bone-marrow stem cells were individually transduced with 20 FlowCode-barcoded retroviruses, containing the tissue TCR clones, and pooled for reconstitution of irradiated mice. After 10 weeks, mice were injected intravenously with anti-CD45 antibody and tissue samples were prepared for analysis by flow cytometry. Cells stained as positive for intravenous anti-CD45 antibody were gated out prior to downstream analysis. FlowCodeDecoder was used to assign each T cell to the appropriate TCR clone, based on expression of the 7 epitopes. Individual results from T cells derived from each of the FlowCode retrogenic TCRs, across the assessed tissues of spleen, LN, kidney, lung, liver, pancreas and LPLs. For each clone and tissue is shown the absolute cell count of detected CD4^{+} T cells (size) together with the frequency of CD69^{+} cells within the population (indicate by colour, with percentage listed on each sample). Relates to **Figure 6**.

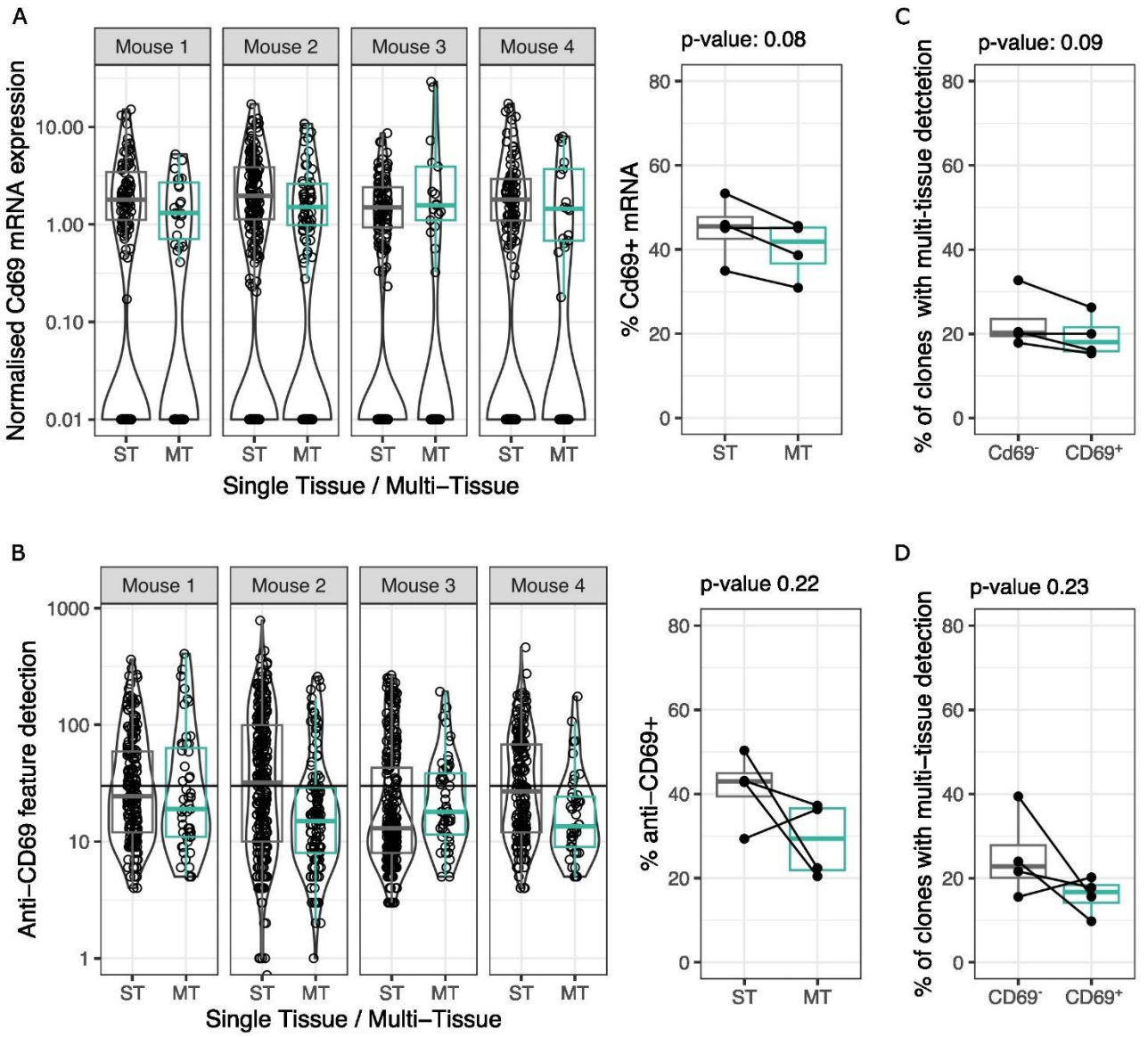
A
Mouse 1
Mouse 2
Mouse 3
Mouse 4
Normalised Cd69 mRNA expression
10.00
1.00
0.10
0.01
ST
MT
Single Tissue / Multi–Tissue
p-value: 0.08
% Cd69+ mRNA
C
p-value: 0.09
% of clones with multi-tissue detctetion
Cd69⁻
CD69⁺
B
Anti–CD69 feature detection
1000
100
10
1
p-value 0.22
% anti–CD69+
D
p-value 0.23
% of clones with multi–tissue detection

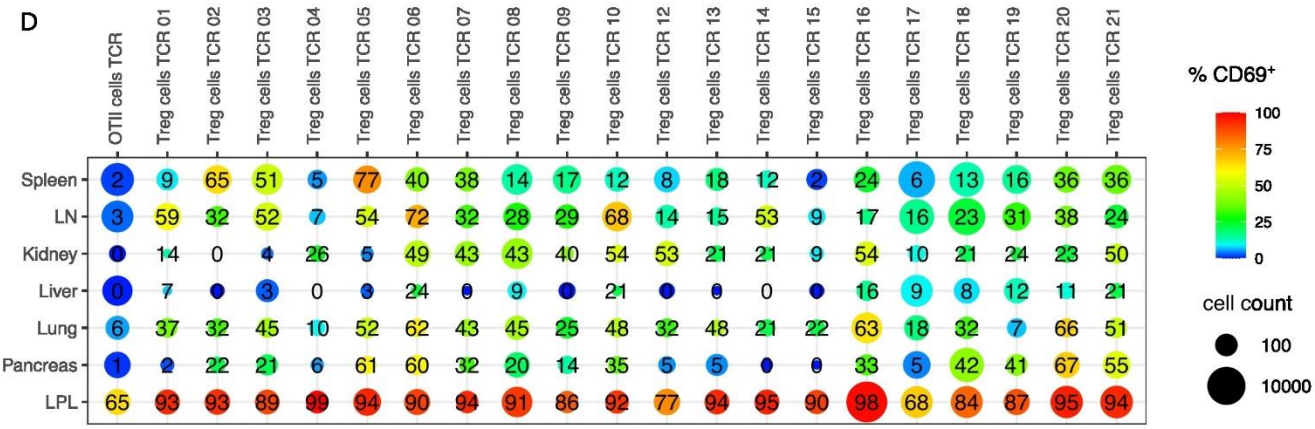
D
OTII cells TCR
Treg cells TCR 01
Treg cells TCR 02
Treg cells TCR 03
Treg cells TCR 04
Treg cells TCR 05
Treg cells TCR 06
Treg cells TCR 07
Treg cells TCR 08
Treg cells TCR 09
Treg cells TCR 10
Treg cells TCR 12
Treg cells TCR 13
Treg cells TCR 14
Treg cells TCR 15
Treg cells TCR 16
Treg cells TCR 17
Treg cells TCR 18
Treg cells TCR 19
Treg cells TCR 20
Treg cells TCR 21
Spleen 2 9 65 51 5 77 40 38 14 17 12 8 18 12 2 24 6 13 16 36 36
LN 3 59 32 52 7 54 72 32 28 29 68 14 15 53 9 17 16 23 31 38 24
Kidney 0 14 0 4 26 5 49 43 43 40 54 53 21 21 9 54 10 21 24 23 50
Liver 0 7 0 3 0 0 24 0 9 0 21 0 0 0 0 16 9 8 12 11 21
Lung 6 37 32 45 10 52 62 43 45 25 48 32 48 21 22 63 18 32 7 66 51
Pancreas 1 2 22 21 6 61 60 32 20 14 35 5 5 0 0 33 5 42 41 67 55
LPL 65 93 93 89 99 94 90 94 91 86 92 77 94 95 90 98 68 84 87 95 94
% CD69⁺
100
75
50
25
0
cell count
100
10000